

©Copyright by Fang Hao 2019

All Rights Reserved

**MATERIALS AND INTERFACIAL ENGINEERING FOR HIGH-
PERFORMANCE ALL-SOLID-STATE BATTERIES**

A Dissertation

Presented to

the Faculty of the Department of Electrical and Computer Engineering

University of Houston

In Partial Fulfillment

of the Requirements for the Degree

Doctor of Philosophy

in Electrical and Computer Engineering

by

Fang Hao

August 2019

**MATERIALS AND INTERFACIAL ENGINEERING FOR HIGH-
PERFORMANCE ALL-SOLID-STATE BATTERIES**

Fang Hao

Approved:

Chair of the Committee
Dr. Yan Yao, Associate Professor,
Electrical and Computer Engineering

Committee Members:

Dr. Stanko R. Brankovic, Professor,
Electrical and Computer Engineering

Dr. Xiaonan Shan, Assistant Professor,
Electrical and Computer Engineering

Dr. Zheng Fan, Assistant Professor,
Engineering Technology

Dr. Jun Lou, Professor,
Materials Science and NanoEngineering
Rice University

Dr. Suresh K. Khator, Associate Dean,
Cullen College of Engineering

Dr. Badri Roysam, Professor and Chair,
Electrical and Computer Engineering

Acknowledgements

First, I would like to express my greatest gratitude to my advisor, Dr. Yan Yao, for his supervision, guidance, and financial assistance throughout my study in the graduate program at UH. Thank you very much for giving me the opportunity to work in this amazing research team. During four years' Ph.D. journey in the Yao Group, I have worked on several research projects focused on solid-state batteries. I have also been challenged with different roles in the laboratory, which not only greatly strengthened my research ability but also enhanced my communication and leadership skills. Dr. Yao continuously motivates me to strive for deeper understanding and instead of satisfying with superficial observations.

I would like to thank the rest of my committee members: Prof. Stanko Brankovic, Prof. Xiaonan Shan, Prof. Zheng Fan, and Prof. Jun Lou for asking interesting questions, providing perceptive suggestions, and kind support on all aspects. Special thanks to Prof. Jun Lou for sharing the facilities and expertise for material characterizations at Rice University with insights for solid-state battery research.

To Yao group labmates, words cannot describe how thankful I am. I was an amateur with no background in the field of energy storage at the beginning of Ph.D. life. It was Dr. Yanliang Liang who gave me the first lesson of electrochemistry and patiently instructed me how coin-cells were built step-by-step. I also learned lots of experimental and writing skills from him. I am very grateful to Dr. Xiaowei Chi, who pioneered the solid-state battery research in our group. I appreciate his tremendous support and patience to help me grow. I have not only enjoyed every scientific discussion, but also our

friendship till this day. For Dr. Pu Hu, Ye Zhang, Hui Dong, Dr. Yi Shi, Yang Chen, Dr. Xiaojun Wang, Dr. Jibo Zhang, who have dedicated themselves to solid-state battery projects and always been supportive to me, I cannot express my appreciation enough to them. I also want to acknowledge my collaborators Dr. Hua Guo, Qing Ai, Dr. Tanguy Terlier from Rice University as well as Dr. Rong Xu, Prof. Kejie Zhao from Purdue University for their excellent expertise on material characterizations. I gratefully acknowledged the funding support from the Department of Energy ARPA-E program.

I want to thank my parents, Shuye Hao and Jun Wu from the bottom of my heart for their endless love and encouragement during my Ph.D. study and throughout my life. To my dear wife Yu Zhang, thanks for always being there when I need you. You have been always believing in me since we met each other 14 years ago and I am very glad to have you as my life partner. To my baby girl Chloe who will be born in one month, daddy cannot wait to see you!

**MATERIALS AND INTERFACIAL ENGINEERING FOR HIGH-
PERFORMANCE ALL-SOLID-STATE BATTERIES**

An Abstract

of a

Dissertation

Presented to

the Faculty of the Department of Electrical and Computer Engineering

University of Houston

In Partial Fulfillment

of the Requirements for the Degree

Doctor of Philosophy

in Electrical and Computer Engineering

by

Fang Hao

August 2019

Abstract

Developing advanced energy storage systems may address the increasing concerns of energy shortage and environmental issues. Among many energy storage technologies, electrochemical energy storage systems such as lithium-ion batteries have been widely used in various applications. However, current lithium-ion batteries using flammable liquid electrolytes may cause a safety risk. All-solid-state sodium batteries (ASSSBs) have been attracting considerable attention as safe and low-cost alternatives to Li-ion batteries. However, the performance of ASSSBs falls short of the requirements for commercial applications mainly due to the challenges at the electrode-solid electrolyte interface.

The goal of this dissertation is to develop new materials and interfacial engineering methods for high-performance ASSSBs with favorable electrode-electrolyte interfaces. In this dissertation, I demonstrate three effective strategies to address the interfacial challenges, namely through the use of organic cathode materials, new solid electrolyte development, and interfacial engineering.

First, a high-performance ASSSB can be achieved using organic cathode materials due to their unique properties. Organic cathode materials with a moderate redox potential enable an (electro)chemically reversible cathode-electrolyte interface. The unique elastic properties of organic cathode materials also ensure intimate contact during cycling. The benefits of organic cathode material are reflected in the excellent cell performance.

Second, an oxysulfide solid-state electrolyte (SE) is developed to improve the stability at the anode-electrolyte interface. The oxygen doped SE with more bridging

units shows a more interconnected glass structure with less grain boundaries than that of pure oxide or sulfide-based SEs, effectively suppressing the dendrite growth. The stronger bonding of P-O than P-S also improves the chemical stability against Na metal, which may be attributed to the electronic insulating interphase that self-limits the continuous interfacial decomposition in sulfide-based SEs.

Pervious two strategies aim to solve the interfacial challenges between sulfide-based electrolytes and electrodes mainly due to the (electro)chemical instability. Oxide-based solid electrolytes can provide much better (electro)chemical stability but poor interfacial contact against electrodes. The third strategy is to introduce auxiliary wetting agents at the electrode-electrolyte interface to significantly improve the interfacial contact and reduce the interfacial resistance. At the anode-electrolyte interface, an introduced Sn thin film can serve as a buffer layer to react with molten Na, forming a NaSn alloy and improving the interfacial contact. At the cathode-electrolyte interface, poly(ethylene oxide) can serve as a mechanically compliant and ionically conductive agent to form an efficient percolation network, enabling the full utilization of the organic cathode material in the ASSSB.

In summary, the demonstrated three strategies address the key challenges in solid-state batteries. Strategy 1 focuses on new electrode materials; strategy 2 proposes new electrolyte materials; and strategy 3 combines strategies 1 and 2 with new device engineering. I hope these approaches will be useful for building future solid-state batteries with higher energy and longer cycling stability, and eventually for enabling large-scale production.

Table of Contents

Acknowledgements.....	v
Abstract.....	viii
Table of Contents	x
List of Figures.....	xv
List of Tables.....	xxi
List of Publications	xxii
Chapter 1 Introduction.....	1
1.1 Solid-State Batteries	1
1.2 Research Objective and Significance	4
1.3 Dissertation Organization	5
Chapter 2 Literature Review of Solid-State Batteries.....	7
2.1 Solid-State Electrolytes.....	7
2.1.1 Historical Outline of Solid-State Electrolytes.....	7
2.1.2 Mechanisms of Ionic Transport in Solid-State Electrolytes	8
2.1.3 State-of-the-Art Solid-State Electrolytes	10
2.2 Architectural Design and Fabrication Approaches for Solid-State Batteries.....	17
2.2.1 Bulk-Type Solid-State Batteries with Thick Solid Electrolyte	17
2.2.2 Sheet-Type Solid-State Batteries with Thin Solid Electrolyte.....	19
2.2.3 Fabrication Approaches to Form Intimate Interparticle Contact	21
2.2.4 Fabrication Approaches to Form Intimate Interlayer Contact	24
2.3 Challenges for Large-Scale Fabrication.....	26

2.3.1 Material Cost.....	26
2.3.2 Mass Loading, Layer Thickness/Density/Uniformity	26
2.3.3 Fabrication Environment	27
2.3.4 Cell Stacking.....	28
2.4 The True Limits: Electro-Chemo-Mechanical Incompatibilities at the Electrode- Electrolyte Interfaces	28
2.4.1 (Electro)chemical Incompatibilities.....	30
2.4.2 Mechanical Incompatibilities.....	34
2.5 Conclusions.....	37
Chapter 3 Forming Stable Cathode-Solid Electrolyte Interfaces with Organic Cathode	39
3.1 Introduction.....	39
3.2 Experimental Procedures	43
3.2.1 Synthesis of Electrodes and Electrolyte.....	43
3.2.2 Materials Characterization	43
3.2.3. Fabrication of All-Solid-State Cells.....	44
3.2.4 Electrochemical Measurements	45
3.3 Effect of Carbon Ratio on the Electrochemical Performance.....	45
3.4 Investigation of Compatible Cathode-Electrolyte Interface	48
3.5 Electrochemical Performance of Organic Cathode-Based All-Solid-State Batteries	51
3.6 Conclusions.....	53
Chapter 4 An Electrochemomechanically Stable Glassy Electrolyte	54

4.1 Introduction.....	54
4.2 Experimental Procedures	56
4.2.1 Synthesis of Oxysulfide Solid-State Electrolytes	56
4.2.2 Materials Characterization of Oxysulfide Solid-State Electrolytes	57
4.2.3 Fabrication of Symmetric Cell and Full Cell	58
4.2.4 Electrochemical Measurements	59
4.3 Structural Characterizations of Oxysulfide Solid-State Electrolytes	60
4.4 Mechanical and Morphological Properties of Oxysulfide Solid-State Electrolytes	64
4.5 Chemical Stabilities of Oxysulfide Solid-State Electrolyte against Na Metal	67
4.6 Electrochemical Performance of Oxysulfide-Based Symmetrical Cell and Full Cell	69
4.7 Conclusions.....	76
Chapter 5 A High-Energy Quinone-Based Solid-State Sodium Battery Using Oxide Electrolyte	77
5.1 Introduction.....	77
5.2 Experimental Procedures	78
5.2.1 Synthesis of Oxide-Based Solid-State Electrolyte.....	78
5.2.2 Interfacial Modification Methods	79
5.2.3 Material Characterizations	79
5.2.4 Fabrication of Symmetric Cells and Full Cells	80
5.2.5 Electrochemical Measurement.....	80
5.3 Interfacial Engineering with Auxiliary Wetting Agents.....	81
5.4 Improved Electrochemical Performance	84

5.5 Conclusions.....	88
Chapter 6 Methods and Tools used in Solid-state Battery Research	90
6.1 Solid-State Electrolyte Synthesis.....	90
6.1.1 Mechanochemical-Synthesis Method	90
6.1.2 Solution-Synthesis Method.....	92
6.2 Characterization of Solid Electrolytes	92
6.2.1 Particle Size	92
6.2.2 Crystalline Structure	93
6.2.3 Ionic Conductivity	94
6.2.4 Electrochemical Stability Window.....	96
6.3 Anode Materials Synthesis.....	97
6.3.1 Na-Sn alloy	97
6.3.2 Li-In alloy	97
6.4 Size Reduction for Cathode Active Materials.....	98
6.4.1 Ball-Milling Method	98
6.4.2 Precipitation Method.....	98
6.5 Physicochemical Characterization Methods.....	99
6.5.1 Mechanical Properties Measurement by Indentation.....	99
6.5.2 Morphological Characterization by Focused-Ion-Beam Scanning Electron Microscopy and Three-Dimensional (3D) Reconstruction.....	101
6.5.3 Chemical Compositional Analysis by Time-of-Flight Secondary Ion Mass Spectrometry (ToF-SIMS)	102
6.6 Electrochemical Impedance Spectroscopy	103

6.6.1 Electronic Conductivities Measurement of Solid-State Electrolytes.....	103
6.6.2 In-Situ EIS Measurement at Various State-of-Charge	104
6.6.3 Ionic/Electronic Conductivities Measurement of Cathode Active Materials.	105
6.7 Full Cell Fabrication	106
6.7.1 Dry Mixing of Composite Cathodes for Bulk-Type Cells Fabrication.....	106
6.7.2 Wet Mixing of Composite Cathodes for Sheet-Type Cells Fabrication.....	107
6.8 Symmetrical Cell Fabrication	108
6.9 Full Cell Testing.....	109
6.10 Symmetrical Cell Testing.....	109
Chapter 7 Summary and Outlook	110
7.1 Summary.....	110
7.2 Outlook and Future Directions	113
References.....	116

List of Figures

Figure 1.1 Ragone plot of traditional batteries and lithium ion batteries. Reprinted with permission from Ref. 6. © 2017 Elsevier.....	2
Figure 1.2 Ragone plot of state-of-the-art batteries and predicted all-solid-state battery system. Reprinted with permission from Ref. 10. © 2015 The Electrochemical Society.....	3
Figure 1.3 Comparison of conventional lithium-ion battery and solid-state lithium battery at the cell, stack, and pack levels. Reprinted with permission from Ref. 15. © 2018 Elsevier.....	4
Figure 2.1 A historical outline of the development of solid-state electrolyte batteries. Reprinted with permission from Ref. 16. © 2017 Springer Nature.....	7
Figure 2.2 Li-ion conduction in amorphous phase of polymer-based SE. Reprinted with permission from Ref. 29. © 1988 John Wiley and Sons.....	9
Figure 2.3 Schematic representation of (a) defect. Reprinted with permission from Ref. 30. © 2018 Elsevier. (b) Migration pathway. (c) Migration mechanism in SEs. Reprinted with permission from Ref. 31. © 2017 Springer Nature.....	10
Figure 2.4 The composition of solid-state batteries and the corresponding requirements of solid-state electrolytes. Reprinted with permission from Ref. 32. © 2018 Elsevier.....	11
Figure 2.5 (a) Crystal structure of cubic $\text{Li}_7\text{La}_3\text{Zr}_2\text{O}_{12}$. (b) 3D conducting network of Li atomic arrangement in cubic $\text{Li}_7\text{La}_3\text{Zr}_2\text{O}_{12}$. Reprinted with permission from Ref. 38. © 2011 Chemistry Letters.....	13
Figure 2.6 (a) Crystal structure of $\text{Li}_7\text{P}_3\text{S}_{11}$. Reprinted with permission from Ref. 46. © 2016 Elsevier. (b) Crystal structure of LPGS. Reprinted with permission from Ref. 47. © 2011 Springer Nature.....	15
Figure 2.7 (a) Crystal structure of $\text{Li}_6\text{PS}_5\text{X}$ with $\text{X} = \text{Cl}, \text{Br}, \text{I}$. (b) The Li positions from localized cages in which multiple jump processes are possible. Reprinted with permission from Ref. 49. © 2017 American Chemical Society.....	16
Figure 2.8 Performance comparison of three classes of solid electrolyte materials. Reprinted with permission from Ref. 16. © 2017 Springer Nature.....	17
Figure 2.9 (a) Schematic representation of a typical bulk-type solid state batteries. (b) Cold-pressing for sulfide electrolyte-based SSB. (c) Sintering process for oxide electrolyte-based SSB.....	18

Figure 2.10 (a) Fabrication of thin solid electrolyte. Reprinted with permission from Ref. 72. © 2015 American Chemical Society. (b) Fabrication of binder-free sheet-type SSB. Reprinted with permission from Ref. 74. © 2017 Springer Nature.	21
Figure 2.11 (a) Finer particles. Reprinted with permission from Ref. 79. © 2017 Elsevier. (b) Solution processible components. Reprinted with permission from Ref. 84. © 2016 American Chemical Society. (c) Auxiliary wetting agents. Reprinted with permission from Ref. 53. © 2018 Elsevier.	23
Figure 2.12 Approaches to improve contact by (a) Surface modified layer. Reprinted with permission from Ref. 89. © 2014 Elsevier. (b) Pre-formed monolithic bilayer structure. Reprinted with permission from Ref. 91. © 2017 RSC Publishing.	25
Figure 2.13 The temperature dependent ionic conductivity of reported solid-state electrolytes and conventional liquid electrolytes. Reprinted with permission from Ref. 110. © 2017 Elsevier.	29
Figure 2.14 The fishbone diagram highlights contributing factors for battery failure. Reprinted with permission from Ref. 106. © 2017 The Electrochemical Society.	30
Figure 2.15 The schematic of open-circuit energy diagram for a Li-SE-Li _x M _y O ₂ solid-state battery system. Reprinted with permission from Ref. 111. © 2019 American Chemical Society.	31
Figure 2.16 Carbon effect on the electrolyte oxidation at the cathode-electrolyte interface. Reprinted with permission from Ref. 54. © 2017 American Chemical Society.	32
Figure 2.17 (a) The indication of mutual diffusion of elemental Co, P, and S. (b) Changes in LiCoO ₂ cathode impedance with or without buffer layer. Reprinted with permission from Ref. 113. © 2010 American Chemical Society.	33
Figure 2.18 The mutual diffusion at the LiCoO ₂ /LLZO interface. Reprinted with permission from Ref. 115. © 2011 Elsevier.	34
Figure 2.19 (a) The optical image of shorted LLZO. (b) SEM image of shorted LLZO. (c) Schematic of Li dendrite growth in intergranular way. Reprinted with permission from Ref. 57. © 2017 Elsevier.	35
Figure 2.20 (a) The optical image and (b) SEM image of Li dendrite in Li ₃ PS ₄ . Reprinted with permission from Ref. 60. © 2019 John Wiley and Sons.	35
Figure 2.21 (a) Volume change of LiCoO ₂ and NCM-811 during de-lithiation process. (b) Contact loss at the interface. (c) Capacity decay due to the contact loss.	

Reprinted with permission from Ref. 116. © 2018 American Chemical Society..... 37

- Figure 3.1 Interfacial compatibility between cathode materials and sulfide electrolytes. (a) Unfavorable interface. (b) Favorable interface. (c) Redox potential versus theoretical specific capacity. (d) Hardness-modulus plot of electrode. 40
- Figure 3.2 Load-displacement response of indentation of PTO and Na₃PS₄. 41
- Figure 3.3 Electrochemical reaction and voltage profile of PTO as a cathode. (a) Molecular structure of PTO and its electrochemical reaction. (b) First-cycle voltage profile of a PTO-Na₃PS₄/Na₃PS₄/Na₁₅Sn₄ half cell at 0.01C at 60°C 46
- Figure 3.4 (a) First-cycle voltage profiles. (b) XPS spectra (S 2p) of the composite cathodes. (c) Capacity and coulombic efficiency vs. carbon ratio. (d) Charging capacity and coulombic efficiency vs. cycle number..... 47
- Figure 3.5 (a) In-situ EIS measurement. Impedance spectra recorded during (b) First discharge and (c) First charge. (d) Voltage profile without PTO in the composite cathode. (e) XPS spectra. (f) ToF-SIMS spectra. 49
- Figure 3.6 Cross-sectional SEM images and elemental mapping of (FIB)-milled composite cathodes. (a) Before cycling. (b) After 200th cycles. 51
- Figure 3.7 (a-c) Different morphologies of PTO and (d-f) their corresponding electrochemical performance. (g) Rate capabilities. (h) Ragone plot. (i) Capacity and coulombic efficiency versus cycle number. 52
- Figure 4.1 Na|SEs interface phenomena in different SEs. (a) Oxide-based electrolyte. (b) Sulfide-based electrolyte. (c) Newly designed oxysulfide glass. 55
- Figure 4.2 Lab-based X-ray diffraction (XRD) patterns of Na₃PS_{4-x}O_x (x=0.00, 0.25, 0.50, and 1.00) SEs. 60
- Figure 4.3 (a) Synchrotron X-ray diffractions. (b) Gaussian fitting of Raman peak (PS₄ mode) at 420 cm⁻¹. (c) ³¹P-NMR spectra. (d) X-ray photoelectron spectra (XPS). (e) Schematics of the network structure of the Na₃PS₄ and Na₃PS₃O. 61
- Figure 4.4 FT-IR spectra of Na₃PS_{4-x}O_x (x=0.00, 0.25, 0.50, and 1.00) SEs. 63
- Figure 4.5 Top view (first row) and cross-sectional (second row) SEM images of HT-Na₃PS₄ glass ceramic, Na₃PS₄ glass, and Na₃PS₃O glass. Scale bar: 10 μm. 64
- Figure 4.6 Galvanostatic cycling of Na|HT-Na₃PS₄|Na symmetric cells at 60 °C under current density of 0.1 mA cm⁻² with a stripping/plating capacity of 0.1 mAh cm⁻² 64

Figure 4.7 (a) Relative density vs. molding pressure plot. (b) SEM images of cross-sectional Na_3PS_4 (first row) and $\text{Na}_3\text{PS}_3\text{O}$ (second row) SE pellets pressed at 150 MPa and 375 MPa.....	65
Figure 4.8 (a) Nano-indentation loading curves. (b) Comparison of Young's modulus and hardness for <i>HT</i> - Na_3PS_4 glass ceramic and oxysulfide glass SEs.	66
Figure 4.9 (a) Electrochemical impedance spectra (EIS) evolution of freshly made and 5 h-standing $\text{Na} \text{SE} \text{Na}$ symmetric cells. (b) P 2p and (c) S 2p XPS spectra of the interfaces between Na and SEs after 5 h of contact.....	67
Figure 4.10 (a) Temperature dependence of the Na-ion conductivities of SEs. (b) Nyquist plot of oxysulfide SEs. (c) Activation energies and conductivities versus oxygen contents.	70
Figure 4.11 Cyclic voltammetry curve of tri-layer electrolyte in $\text{Na} \text{SE} \text{Stainless Steel}$ asymmetric cell. Insets show the schematic of the cell set-up and SEM image of the tri-layer electrolyte. Scale bar is 100 μm	71
Figure 4.12 Critical current density test of $\text{Na}_3\text{PS}_3\text{O} \text{Na}_3\text{PS}_{3.75}\text{O}_{0.25} \text{Na}_3\text{PS}_3\text{O}$ tri-layer SE working in $\text{Na} \text{SE} \text{Na}$ symmetric cells at 60 °C, step size of the current density increase is 0.05 mA cm^{-2} and plating/stripping time is 0.5 h.....	72
Figure 4.13 Galvanostatic cycling of $\text{Na} \text{Na}_3\text{PS}_3\text{O} \text{Na}_3\text{PS}_{3.75}\text{O}_{0.25} \text{Na}_3\text{PS}_3\text{O} \text{Na}$ symmetric cells at 60 °C under current densities of (a) 0.2 mA cm^{-2} and (b) 0.5 mA cm^{-2} , respectively.....	73
Figure 4.14 Na-S full cell performances at 60 °C. (a) Charge/discharge voltage profiles. (b) Capacity and coulombic efficiency vs. cycle number. (c) Rate capability and cycling stability under different current densities.	75
Figure 5.1 (a) Arrhenius plot of ionic conductivity of BASE. Inset: cross-sectional scanning electron microscopy (SEM) image of a BASE pellet. (b) X-ray diffraction patterns of the BASE with and without Sn coating.....	81
Figure 5.2 (a) Different wetting behaviors of molten Na on bare and Sn-coated BASE. (b) Magnified SEM image of coated vs. uncoated portion of BASE. (c) Energy dispersive spectroscopy (EDS) shows the formation of NaSn alloy. .	82
Figure 5.3 Profilometer measurement of a Sn layer.	83
Figure 5.4 (a) Schematic of $\text{Na}/\text{Sn}/\text{BASE}/\text{PTO}/\text{PEO}$ structure. (b–c) SEM images highlight the intimate contact between the cathode composite and BASE. ...	84
Figure 5.5 A cross-sectional SEM image highlights the non-ideal mechanical contact between PTO-C65 cathode and BASE electrolyte.	84

Figure 5.6 (a) Voltage profiles of the Na/BASE/Na cell. Inset: EIS spectrum. (b) EIS spectrum of the Na/Sn/BASE/Sn/Na cell. (c) Voltage profiles of the Na/Sn/BASE/Sn/Na cell.	85
Figure 5.7 (a) EIS spectrum and corresponding equivalent circuit. (b) Voltage profiles at 0.1C for 50 cycles. (c) Cycling stability and coulombic efficiency vs. cycle number. (d) A comprehensive comparison with all reported ASSMBs.	87
Figure 5.8 Electrochemical performance of an all-solid-state cell (Na/Sn/BASE/PTO-PEO) using PEO as a cathode side interlayer measured at 60 °C. (a) Galvanostatic voltage profiles and (b) cycling at different C rates.....	88
Figure 6.1 DSC measurement of the as-synthesized 75Li ₂ S-25P ₂ S ₅ glassy electrolyte. .	91
Figure 6.2 SEM images of glass ceramic Li ₃ PS ₄ electrolyte synthesized by (a) high energy ball milling. (b) solution synthesized with THF. (c) high energy + low energy ball milling followed by sifting.....	93
Figure 6.3 The XRD patterns of the reported glassy 75Li ₂ S-25P ₂ S ₅ , glass ceramic Li ₃ PS ₄ (Figure 6.3a), and our home-made glass ceramic Li ₃ PS ₄ (Figure 6.3b). Figure 6.3a is reprinted with permission from Ref. 213. © 2017 Springer Nature....	94
Figure 6.4 (a) The representative EIS spectra of solid electrolyte for ionic conductivity measurement. (b) The temperature-dependent ionic conductivity of Li ₃ PS ₄ . Inset is the cell architecture for ionic conductivity measurement.....	95
Figure 6.5 Cyclic voltammetry profile and cell architecture for electrochemical stability window measurement.	96
Figure 6.6 (a) As-synthesized PTO. (b) PTO-Micro pellet that treated by low-energy ball milling process. (c) PTO-Nano rod that treated by precipitation method.....	98
Figure 6.7 The load-displacement curve for an indentation experiment. Reprinted with permission from Ref. 149. © 1992 Materials Research Society.	99
Figure 6.8 Load-displacement response of indentation of Na ₃ PS ₄	100
Figure 6.9 (a) Cross-sectional SEM image of the composite cathode. (b) Acquisition and align of consecutive SEM images. (c) 3D reconstruction of the composite cathode.....	102
Figure 6.10 The schematic setup of ToF-SIMS.	103
Figure 6.11 The representative current-time curves for electronic conductivity measurement. Reprinted with permission from Ref. 216. © 2019 Springer Nature.	104

Figure 6.12 EIS spectra during (a) discharge and (b) charge process and their corresponding real part resistance versus minus square root of frequency during (c) discharge and (d) charge process. 105

Figure 6.13 DC polarization curves for (a) electronic conductivity measurement and (b) ionic conductivity measurement of active material. Reprinted with permission from Ref. 217. © 2017 Elsevier. 106

Figure 6.14 The comparison of fabrication procedures of bulk-type and sheet-type solid-state batteries. Reprinted with permission from Ref. 75. © 2017 The Electrochemical Society. 108

List of Tables

Table 3.1 Comparison of electrochemical performance of previously reported intercalation-type cathode materials and this work for all-solid-state sodium cells.....	42
Table 4.1 Fitting results of EIS spectra (Figure 4.9a) of Na Na ₃ PS _{4-x} O _x (x=0.00, 0.25, 0.50, and 1.00) SEs Na symmetric cells before and after resting for 5 h.....	68
Table 4.2 Comparison of reported critical current densities (CCD) of SEs with that of Na ₃ PS ₃ O SE developed our work.....	72
Table 4.3 Comparison of reported Na-S batteries using SEs with our work	75
Table 5.1 Cell performance of reported all-solid-state sodium metal batteries.	78
Table 5.2 EIS spectra fitting of the symmetric cells shown in the inset of Figure 5.6a and Figure 5.6b. R_b , R_i , and R_{ct} represent the resistance of the BASE bulk, the resistance of the interphase, and the charge transfer resistance.	86
Table 5.3 Fitting results for the EIS spectra shown in Figure 5.7a. In the equivalent circuit, W_s represents the Warburg diffusion resistance. R_b , R_i , R_{ct} , refer to the same definitions as above.....	86

List of Publications

1. **F. Hao**,[‡] X. Chi,[‡] Y. Liang, Y. Zhang, R. Xu, H. Guo, H. Dong, K. Zhao, J. Lou, Y. Yao, “Taming active material–solid electrolyte interfaces with organic cathode for all-solid-state batteries”, *Joule*, **2019**, 3, 1349–1359.
2. **F. Hao**, F. Han, Y. Liang, C. Wang, Y. Yao, “Architectural design and fabrication approaches for solid-state batteries”, *MRS Bull*, **2018**, 43, 775–781.
3. X. Chi,[‡] **F. Hao**,[‡] J. Zhang, X. Wu, Y. Zhang, S. Gheytani, Z. Wen, Y. Yao, “A high-energy quinone-based all-solid-state sodium metal battery”, *Nano Energy*, **2019**, 62, 718–724
4. S. Venkatesan, **F. Hao**, J. Y. Kim, Y. Rong, Z. Zhu, Y. Liang, J. Bao, Y. Yao, “Moisture-driven phase transition for improved perovskite solar cells with reduced trap-state density”, *Nano Research*, **2017**, 10, 1413–1422
5. X. Chi,[‡] Y. Liang,[‡] **F. Hao**, Y. Zhang, J. Whiteley, H. Dong, P. Hu, S. Lee, Y. Yao, “Tailored organic electrode material compatible with sulfide electrolyte for stable all-solid-state sodium batteries”, *Angewandte Chemie*, **2018**, 57, 2630–2634.
6. P. Hu,[‡] Y. Zhang,[‡] X. Chi, K. K. Rao, **F. Hao**, H. Dong, F. Guo, Y. Ren, L. C. Grabow, Y. Yao, “Stabilizing the interface between sodium metal anode and sulfide-based solid-state electrolyte with an electron blocking interlayer”, *ACS Appl. Mater. Interfaces*, **2019**, 11, 9672–9678.
7. Y. Chen,[‡] Y. Shi,[‡] Y. Liang,[‡] H. Dong, **F. Hao**, A. Wang, Y. Zhu, X. Cui, Y. Yao, “Hyperbranched PEO-based hyperstar solid polymer electrolytes with simultaneous improvement of ion transport and mechanical strength”, *ACS Appl. Energy Mater.*, **2019**, 2, 1608–1615.
8. H. Dong, Y. Liang, O. Tutusaus, R. Mohtadi, Y. Zhang, **F. Hao**, Y. Yao, “Directing Mg-storage chemistry in organic polymers towards high-energy Mg batteries”, *Joule*, **2018**, 3, 782–793.
9. R. Guo, Z. Zhu, A. Boulesbaa, **F. Hao**, A. Puretzky, K. Xiao, J. Bao, Y. Yao, W. Li, “Synthesis and photoluminescence properties of 2D phenethylammonium lead bromide perovskite nanocrystals”, *Small Methods*, **2017**, 1700245.
10. Z. Zhu, V. G. Hadjiev, Y. Rong, R. Guo, Z. Tang, F. Qin, Y. Li, Y. Wang, **F. Hao**, S. Venkatesan, W. Li, S. Baldelli, A. M. Guloy, H. Fang, Y. Hu, Y. Yao, Z. Wang, J. Bao, “Interaction of organic cation with water molecule in perovskite MAPbI₃: from dynamic orientational disorder to hydrogen bonding”, *Chem Mater.* **2016**, 28, 7385–7393.

11. X. Hou, M. Xu, C. Tong, W. Ji, Z. Fu, Z. Wan, **F. Hao**, Y. Ming, S. Liu, Y. Hu, H. Han, Y. Rong, Y. Yao, “High performance printable perovskite solar cells based on $\text{Cs}_{0.1}\text{FA}_{0.9}\text{PbI}_3$ in mesoporous scaffolds”, *J. Power Sources*, **2019**, 415, 105–111.
12. X. Chi,[‡] Y. Zhang,[‡] **F. Hao**,[‡] S. Kmiec,[‡] R. Xu, K. Zhao, S. W. Martin, Y. Yao, “An electrochemomechanically stable and structurally flawless glassy electrolyte: towards new solid-state Na metal batteries”, *In preparation*.

Chapter 1 Introduction

1.1 Solid-State Batteries

Fossil fuels (oils, coals, and natural gases) have served as the most dominant source of energy supply in the past few centuries. These convenient and cheap sources, however, are not sustainable, resulting in the severe depletion of these fossil fuel reserves. The combustion reaction of fossil fuels also emits a significant amount of carbon dioxide, which is the primary culprit behind global warming.¹ Therefore, the development of advanced energy storage systems and devices is one of the most promising solutions to alleviate the environmental concerns and the utilization of renewable energy sources is imperative.

Rechargeable lithium ion batteries have been the predominant power source for portable electronics and electric vehicles owing to their high energy density, long cycle life, and high sustainability.²⁻⁵ However, current commercial batteries do not meet the urgent and increasing demands of these systems, in particular for large-scale applications like electric vehicles. This is because the state-of-the-art lithium ion batteries have a severe shortage of specific energy and specific power as shown in Figure 1.1. Most current lithium ion batteries with specific energy of 80-120 Wh/kg only allow short distances of 100-150 miles for an electric vehicle. This limited ranges are far from the requirements for advanced automotive batteries with higher specific energy of 350 Wh/kg in order to have a longer driving distance.⁶ One apparent approach to improve the specific energy is to replace the graphite anode with Li metal anode, which has approximately 10 times higher specific capacity (3860 mAh/g) than that of graphite

anode.⁷ However, battery charge/discharge cycling leads to non-uniform stripping and plating of the Li metal, eventually causing the Li dendrites growth.⁸ These dendrites can penetrate the separator and connect the anode to the cathode, allowing an internal electron transport pathway with an extremely high current that can ignite the flammable liquid electrolyte and result in battery explosions. Therefore, the limited development with lithium ion batteries with poor specific energy and high safety risk is strongly correlated with organic liquid electrolytes.

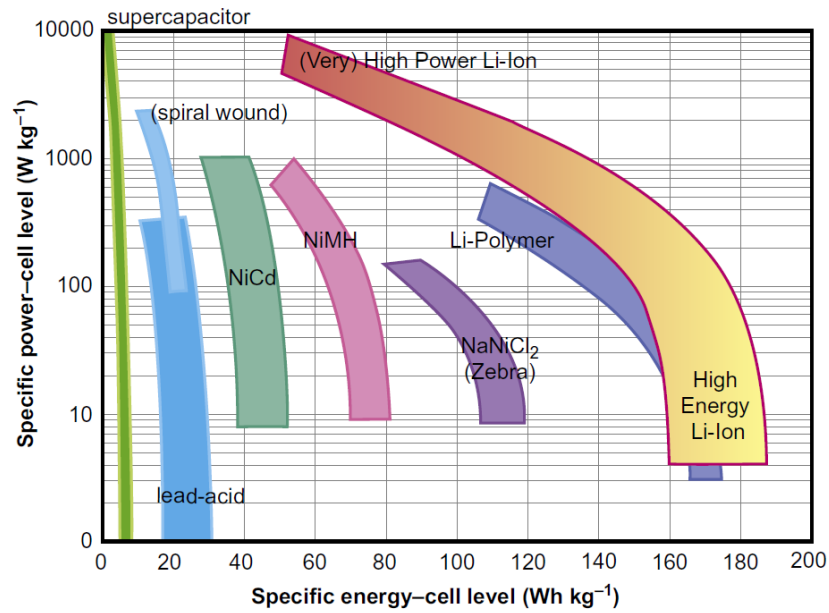


Figure 1.1 Ragone plot of traditional batteries and lithium ion batteries. Reprinted with permission from Ref. 6. © 2017 Elsevier.

Solid-state batteries (SSBs) are receiving intense interests not only because of the improved safety by replacing organic-based flammable liquid electrolytes with inorganic-based solid ones,⁹ but also the possibility of using lithium or sodium metal for improving the cell-level specific energy as shown in Figure 1.2.¹⁰

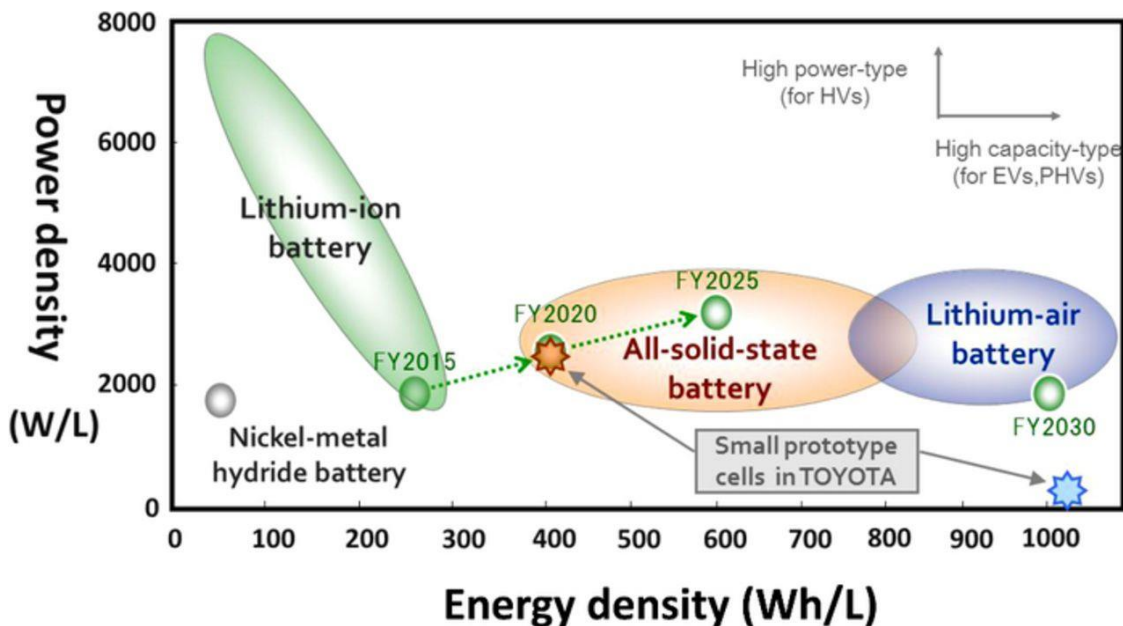


Figure 1.2 Ragone plot of state-of-the-art batteries and predicted all-solid-state battery system. Reprinted with permission from Ref. 10. © 2015 The Electrochemical Society.

Additionally, SSBs also offer unique advantages over conventional liquid-electrolyte batteries such as: (i) the prevention of electrode cross-talk,¹¹ (ii) the formation of a less dynamic interphase,¹² (iii) the possibility for extremely high power and ultra-thick electrode because of the absence of electrolyte concentration gradient and high concentration of metal-ion per volume,^{13, 14} and (iv) the possibility for bipolar design as shown in Figure 1.3.¹⁵ In a traditional lithium ion battery, the liquid electrolyte is mobile and interconnects all components of the battery cell. Therefore, each single cell must be connected in parallel and then packed in series. In contrast, a solid-state electrolyte is immobile, therefore, each single cell can be connected in series with a shared ionic insulating current collector and packed in parallel. The reduction of the number of current collectors and the exclusion of the cooling system significantly reduce the weight and volume of the package, leading to an improved cell-level specific energy.

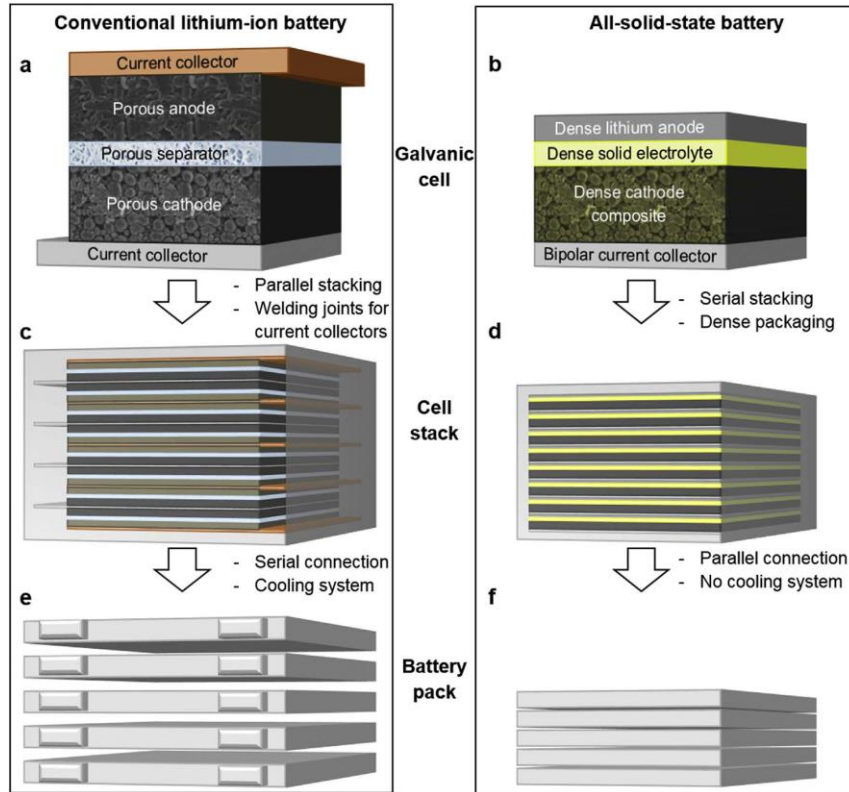


Figure 1.3 Comparison of conventional lithium-ion battery and solid-state lithium battery at the cell, stack, and pack levels. Reprinted with permission from Ref. 15. © 2018 Elsevier.

1.2 Research Objective and Significance

Due to the substantial reserve and low cost of sodium resources, solid-state sodium-ion batteries are attracting considerable attention. Therefore, the focus of this dissertation will be on developing the high-performance solid-state sodium-ion batteries with high-energy and long-cycle-life. This dissertation reveals the fundamental hurdles, which are interfacial incompatibilities between electrode and electrolyte. This dissertation proposes three viable approaches to overcome these issues in different perspectives: 1) the use of innovative organic cathode materials; 2) the development of new solid electrolyte; 3) solid-state cell architectural design. The demonstrated methods open a new

opportunity to realize a stable electrode-electrolyte interface for enhancing performances of solid-state batteries and can be expanded in solid-state lithium-ion batteries for the future work.

1.3 Dissertation Organization

The contents of this dissertation are divided into seven chapters. The motivation and advantages of developing solid-state batteries are discussed in Chapter 1. Chapter 2 reviews relevant literature based on emerging solid-state electrolytes, architectural design, fabrication approaches, and large-scale fabrication challenges for solid-state batteries. The main hurdles regarding interfacial incompatibilities of developing high-performance solid-state batteries are illustrated and the corresponding failure results related to interfaces are analyzed.

The detailed research projects are reported in Chapters 3, 4, and 5. Chapter 3 begins with a detailed study on taming active material-solid electrolyte interface to achieve high-performance solid-state batteries by using organic cathode material. The quinone-based organic active material with moderate redox potential and unique mechanical properties enables the solid-state sodium-ion batteries to deliver high specific energy and long cycling stability.

Chapter 4 focuses on developing new oxysulfide electrolyte for improving anode-electrolyte interfacial stability, enabling the use of Na metal as anode material to further improve the specific energy. The features of a defect-free structure and excellent chemical stability of electrolyte enable the best cycling stability with Na metal over all the other known solid electrolytes.

Chapter 5 develops solutions to address the interfacial contact challenges between

oxide-based solid electrolyte and electrodes by introducing auxiliary wetting agents at the interlayers. This work represents the first use of organic redox materials in oxide-based solid-state sodium batteries. The study establishes effective interfacial modifying strategies for developing high-performance solid-state sodium metal batteries, and to all emerging solid-state batteries in general.

Chapter 6 summarizes all fundamental and advanced methodologies that I find important and useful for solid-state batteries research. The fundamental synthesis methods for electrode and electrolyte, processing procedures for the composite cathodes, fabrication approaches, and test protocol for solid-state batteries are also introduced.

A final summary is provided and the outlook for this work is discussed.

Chapter 2 Literature Review of Solid-State Batteries

2.1 Solid-State Electrolytes

2.1.1 Historical Outline of Solid-State Electrolytes

Solid-state electrolytes (SEs) can be divided into two categories of material: inorganic sulfide-based/oxide-based SEs and organic polymer-based SEs. Efforts to incorporate SEs into batteries can be traced to the 1960s, when a fast sodium-ion-conductor β -alumina ($\text{Na}_2\text{O} \cdot 11\text{Al}_2\text{O}_3$) for high-temperature sodium-sulfur batteries was discovered by Joseph and Weber from Ford Corporation, which marked as a milestone in the development of SEs (Figure 2.1).¹⁶

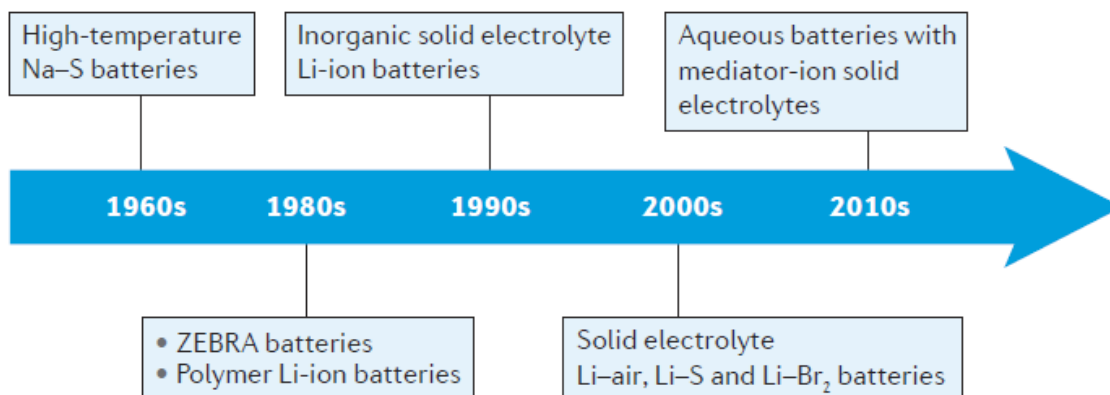


Figure 2.1 A historical outline of the development of solid-state electrolyte batteries. Reprinted with permission from Ref. 16. © 2017 Springer Nature.

Three types of battery chemistry using Ag_3SI , RbAg_4I_5 , and β -alumina were successfully demonstrated in the 1960s and early 1970s, boosting the development pace of SEs.¹⁷⁻¹⁹ In the 1980s, β -alumina was used in ZEBRA cell, in South African for high-temperature battery system.²⁰ An organic polymer-based SE based on poly(ethylene oxide) (PEO) was also discovered.²¹ Inorganic SEs have been used since the 1990s, after a lithium phosphorus oxynitride (LiPON) was fabricated as a thin-film solid electrolyte

by the Oak Ridge National Laboratory.²² After that, significant effort has been made towards the development of inorganic lithium-ion conductive ceramic materials, such as oxide-based SEs including perovskite-type,²³ sodium superionic conductor (NASICON)-type,²⁴ garnet-type,²⁵ and sulfide-based SE materials.²⁶ In the following sections, ion-transport mechanisms, fundamental properties, and crystal structures of state-of-the-art SEs will be reviewed and discussed.

2.1.2 Mechanisms of Ionic Transport in Solid-State Electrolytes

The mechanism of ionic transport in SEs are fundamentally different from those of traditional liquid electrolytes. In liquid electrolytes, both the cations and anions are mobile and contribute to the conductivity. As a result, the Li-ion transference number is generally lower than 0.5.²⁷ During cell cycling, Li-ions and anions will move in opposite direction, leading to the accumulation of anions at the other side and causing concentration gradients, cell polarization, and further degradation to the cell performance. In contrast, only one type of ion is mobile in SSEs, thus, the Li-ion transference number is 1, eliminating the possibility of electrodes cross-talk.

The temperature dependence ionic conductivity is one of the key metrics for SEs. It is usually modeled by the Arrhenius equation (for inorganic SEs, Equation 2-1):

$$\sigma_i = \frac{A}{T} \exp \left[-\frac{E_a}{kT} \right] \quad (2-1)$$

or the Vogel-Tammann-Fulcher (VTF) equation (for organic polymer-based SEs, Equation 2-2).²⁸

$$\sigma_i = \sigma_0 T^{-\frac{1}{2}} \exp \left[-\frac{B}{T - T_0} \right], \quad (2-2)$$

where A and σ_0 are the pre-exponential factor, k is the rate constant, E_a is the activation

energy, B is the pseudo-activation energy, and T_0 is the reference temperature.

In organic polymer-based SEs, the ionic conduction is realized by the ions migrating from one coordinating site to another with the aid of the segmental motion of polymer chains at amorphous phase above the glass transition temperature (T_g) as shown in Figure 2.2.²⁹ Therefore, the lower T_g leads to the fast ion motion and the increase of ionic conductivity.

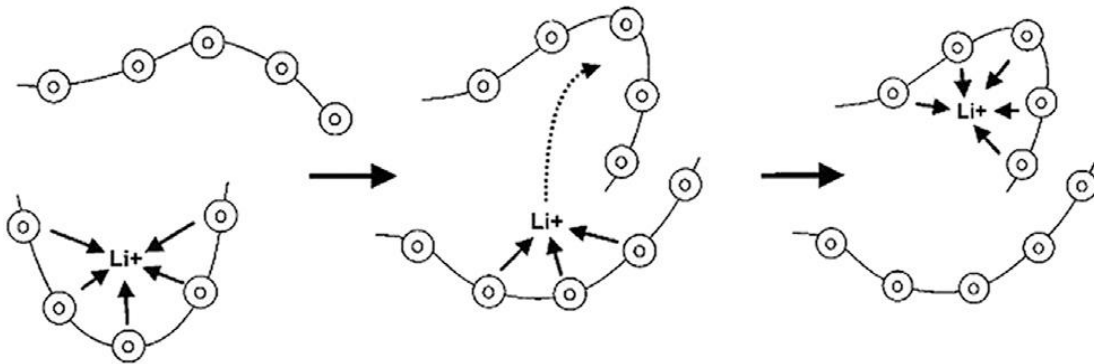


Figure 2.2 Li-ion conduction in amorphous phase of polymer-based SE. Reprinted with permission from Ref. 29. © 1988 John Wiley and Sons.

In inorganic SEs, Li-ions transport is generally achieved by their concentration and distribution of defects (Figure 2.3a).³⁰ The ionic diffusion mechanism based on Schottky and Frenkel point defects mainly include vacancy mechanism, interstitial mechanism, and the interstitial-substitutional exchange mechanism (Figure 2.3c). Vacancy mechanism generally relies on the Schottky defects that create many vacancies available for ion-migrating among the crystalline. Interstitial mechanism normally depends on the Frenkel defects by continuously dislocating Li ions in adjacent available sites. In addition, super-ionic conductors with high ionic conductivity ($\sim 10^{-2}$ S/cm) can be achieved by a synergistic mechanism as reported by Mo et al.,³¹ who found that the

ions do not hop isolate, but instead migrate through concerted migrations of multiple ions with low energy barriers (Figure 2.3b).

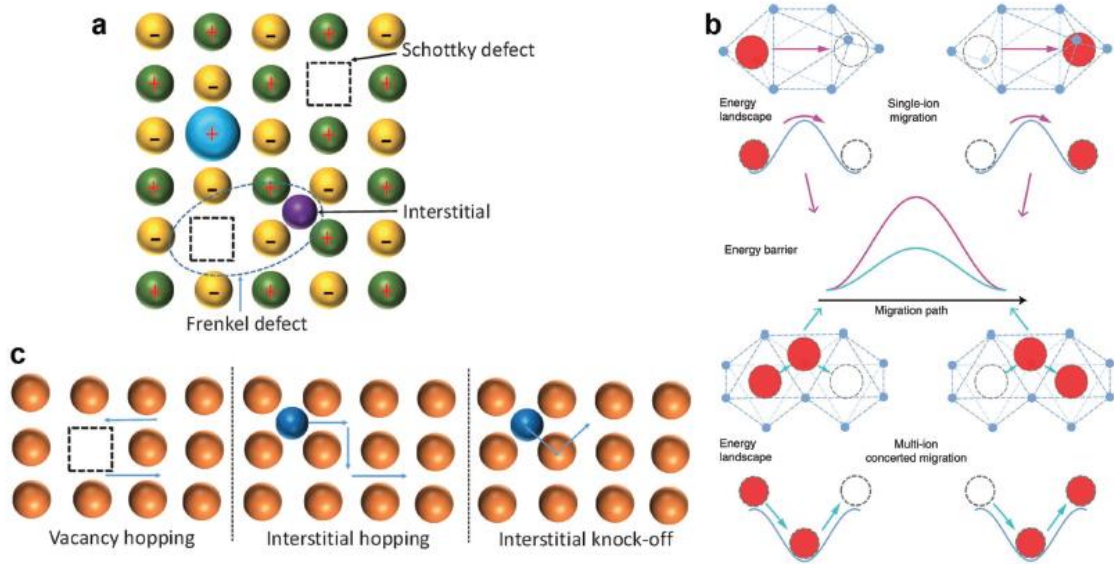


Figure 2.3 Schematic representation of (a) defect. Reprinted with permission from Ref. 30. © 2018 Elsevier. (b) Migration pathway. (c) Migration mechanism in SEs. Reprinted with permission from Ref. 31. © 2017 Springer Nature.

Overall, to achieve fast ionic conduction, three minimum criteria must be satisfied: (i) the number of available equivalent sites for the mobile ions to occupy should be much larger than the number of mobile species; (ii) the migration barrier energies between the adjacent available sites should be low enough for an ion to migrate easily from one site to another; (iii) and these available sites must be connected to form a continuous diffusion pathway. These standards also apply to the sodium-ion conductor.

2.1.3 State-of-the-Art Solid-State Electrolytes

Solid-state electrolyte is the most vital component in solid-state batteries. It determines the delivered energy, power, stability, and the safety of the SSBs. To achieve a high-performance SSB, solid-state electrolytes must fulfill numerous metrics such as high

ionic conductivity, high interfacial compatibilities, good mechanical properties, facile preparation, and so on (Figure 2.4).³² However, all state-of-the-art SEs can not simultaneously meet these requirements. In this section, I will introduce a general overview of these features of SEs. The detailed review regarding processing approaches, architectures, and interfacial compatibilities will be discussed in the following sections.

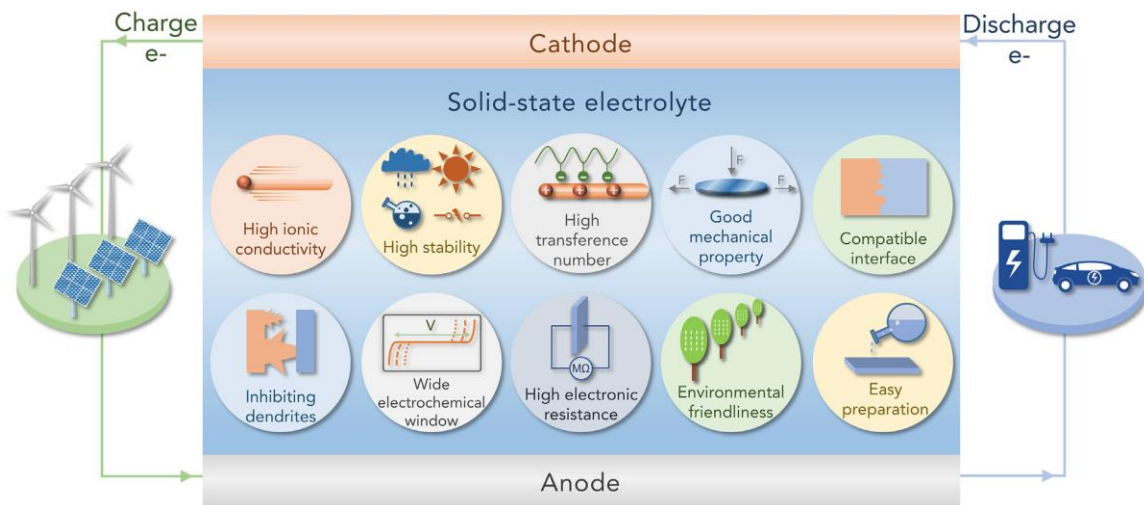


Figure 2.4 The composition of solid-state batteries and the corresponding requirements of solid-state electrolytes. Reprinted with permission from Ref. 32. © 2018 Elsevier.

The development of organic polymer-based SEs can be divided into three categories: gel polymer electrolytes, dry solid polymer electrolytes, and composite polymer electrolytes. However, as gel polymers are not in the solid state, they will not be discussed here. Dry solid polymer electrolytes are usually flexible, thus allowing a facile device integration and decent processing scalability. It also own decent stability with Lithium metal.³³ However, one of the main drawbacks is the low ionic conductivity (10^{-6} S/cm) at ambient temperatures. Using polymer-based SEs at elevated temperatures can increase the ionic conductivity but sacrifice the mechanical strength. Therefore, composite polymer-based SEs, developed by introducing ceramic fillers into the organic

polymer host, help to improve conductivity by decreasing the glass transition temperatures and further the crystallinity.³⁴ The other disadvantage of polymer-based SEs is the low ionic transference number, causing concentration gradients and cell polarization. Therefore, single-ion-conducting polymer-based SEs gradually becomes the research interest, whose anions are anchored to the host backbone or immobilized by anion acceptors, exhibiting a high lithium-ion transference number approaching unity.³⁵

In general, inorganic SEs can be divided into oxide-based SE and sulfide-based SE. The main oxide-based SEs that are being studied for SSBs are garnet-type, perovskite-type, LISICON-type, and NASICON-type. Garnet-type materials have the general formula $A_3B_2X_3O_{12}$ (A = Ca, Mg, Y, La or rare earth; B = Al, Fe, Ga, Ge, Mn, Ni, V; X = Si, Ge, Al), where the A and B cations have eight-fold and six-fold coordination, respectively. The first representative garnet-type lithium ion conductor $Li_5La_3M_2O_{12}$ (M = Nb, Ta) with ionic conductivity of 10^{-5} S/cm was developed in 2003.³⁶ Since then, the conductivity was further increased to 10^{-3} S/cm with Li rich garnets such as $Li_6Ala_2M_2O_{12}$ (A = Mg, Ca, Sr, Ba),³⁶ and $Li_7La_3C_2O_{12}$ (C = Zr, Sn).³⁷ The improved ionic conductivities in Li rich garnets were attributed to 3D network of the Li-ion migration pathway with short Li-Li distance and occupational disordering is formed in the garnet-type framework structure. The basic unit of the pathway is a loop constructed by the Li1 and Li2 sites (Figure 2.5).³⁸

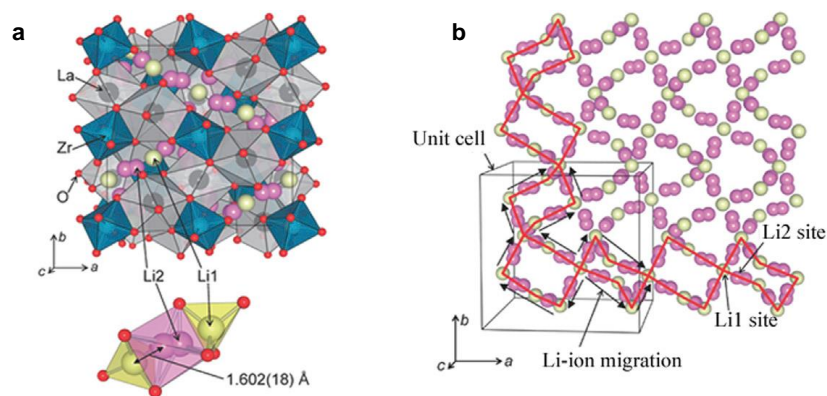


Figure 2.5 (a) Crystal structure of cubic $\text{Li}_7\text{La}_3\text{Zr}_2\text{O}_{12}$. (b) 3D conducting network of Li atomic arrangement in cubic $\text{Li}_7\text{La}_3\text{Zr}_2\text{O}_{12}$. Reprinted with permission from Ref. 38. © 2011 Chemistry Letters.

Garnet-type SEs have numerous advantages such as high (electro)chemical stability against Li metal, high anodic decomposition potential, and high mechanical strength. However, it is rigid and difficult to be fabricated in large-scale production due to the requirement of high temperature annealing. It is also not stable when exposed to the moisture, leading to the formation of Li_2CO_3 , which has been found as a key component to degrade the interfacial contact between Li metal and cubic $\text{Li}_7\text{La}_3\text{Zr}_2\text{O}_{12}$.³⁹

The general formula of perovskite structure is ABO_3 ($\text{A} = \text{Li}, \text{La}$; $\text{B} = \text{Ti}$), where the A sites are in twelve-fold coordination and the B sites are in six-fold coordination. The representative perovskite solid electrolyte is $\text{Li}_{3x}\text{La}_{2/3-x}\text{TiO}_3$, which shows ionic conductivity of 10^{-3} S/cm at room temperature.⁴⁰ However, these materials are not stable against Li metal because the facile reduction of Ti^{4+} when in contact with Li metal, thus limiting their practical applications.

Lithium Super Ionic Conductors (LISICONs) have crystal frameworks that are similar to the $\gamma\text{-Li}_3\text{PO}_4$ structure with an orthorhombic unit cell and $Pnma$ space group.⁴¹ LISICONs are three-dimensional structures with a hexagonal close packing of oxygen

atoms with Ge, Li and Zn cations occupying the tetrahedral and octahedral interstices.⁴² The room temperature conductivity of LISICONs is quite low ($\sim 10^{-7}$ S/cm), which fails to meet the basic requirement of SE.

Sodium Super Ionic Conductors (NASICONs) have the general formula $\text{LiM}_2(\text{XO}_4)_3$ (M = Ge, Ti, or Zr; X = S, P, As, Mo). Generally, the compounds are rhombohedral structures (space group R3c) with a 3D framework built up by $\text{M}_2(\text{XO}_4)_3$ units in which two MO_6 octahedra and three XO_4 tetrahedra share oxygen atoms while the A^+ ions diffuse through interstices.⁴³ These NASICONs such as $\text{Li}_{1+x}\text{Al}_x\text{Ti}_{2-x}(\text{PO}_4)_3$ (LATP) and $\text{Li}_{1+x}\text{Al}_x\text{Ge}_{2-x}(\text{PO}_4)_3$ (LAGP) exhibit excellent ionic conductivity of $\sim 10^{-3}$ S/cm at room temperature.⁴⁴ However, they are also not stable with Li metal due to the reduction of Ti^{4+} or Ge^{4+} when in contact with Li metal anode.

For sulfide-based SEs, glassy powders with low ionic conductivity of $\sim 10^{-7}$ - 10^{-5} S/cm can be prepared from mechanical ball milling. To increase the conductivity, the glass-ceramic and ceramic sulfide-based SEs with crystalline phase can be obtained by the heat treatment.⁴⁵ The earliest studied sulfide-type solid electrolyte was the $\text{Li}_2\text{S-SiS}_2$ system. Various other types which followed are LiS-GeS_2 , $\text{Li}_2\text{S-B}_2\text{S}_3$ and $\text{Li}_2\text{S-P}_2\text{S}_5$. The compounds $x\text{Li}_2\text{S} \cdot (100-x)\text{P}_2\text{S}_5$ (x from 70 to 80) have been investigated extensively. Among them, the stoichiometric $\text{Li}_7\text{P}_3\text{S}_{11}$ exhibits the highest ionic conductivity of 4.2×10^{-3} S/cm, which is contributed from the direct Li-ion hopping with a low activation barrier in the triclinic crystal structure (Figure 2.6a).⁴⁶ Recently, Kanno et al. reported that $\text{Li}_{10}\text{GeP}_2\text{S}_{12}$ (LGPS)⁴⁷ and $\text{Li}_{9.54}\text{Si}_{1.74}\text{P}_{1.44}\text{S}_{11.7}\text{Cl}_3$ (LSPSCI)¹³ provide extremely high ionic conductivity more than 10^{-2} S/cm which is comparable to that of the conventional liquid electrolyte. Figure 2.6b shows the framework structure of LGPS composed of

$(\text{Ge}_{0.5}\text{P}_{0.5})\text{S}_4$ tetrahedra and LiS_6 octahedra connected to each other by a common edge, forming 1D Li conduction path along the c-axis.⁴⁷ In addition to the high ionic conductivity, sulfide-based SEs also owns excellent deformability, enabling an easy device integration and good scalability. However, sulfide-based SEs are extremely sensitive to moisture, leading to the formation of hydrogen sulfide. The other big challenge brought by sulfide-based SEs is the poor interfacial compatibilities against cathode and anode materials, which will be discussed in detail in section 2.3, significantly slowing down the development pace.

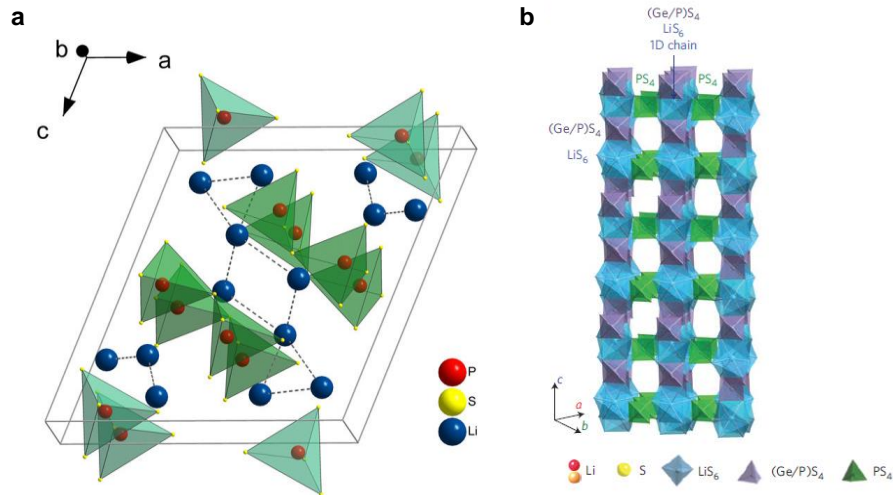


Figure 2.6 (a) Crystal structure of $\text{Li}_7\text{P}_3\text{S}_{11}$. Reprinted with permission from Ref. 46. © 2016 Elsevier. (b) Crystal structure of LPGA. Reprinted with permission from Ref. 47. © 2011 Springer Nature.

The addition of halides to sulfide-based SEs can increase the conductivity of quasi-binary or quasi-ternary systems. Outstanding examples are the halogen-substituted argyrodites $\text{Li}_6\text{PS}_5\text{X}$ ($X = \text{Cl}, \text{Br}, \text{I}$).⁴⁸ Figure 2.7a shows the unit cell of $\text{Li}_6\text{PS}_5\text{X}$. The framework of the lattice is built-up by PS_4^{3-} anions that centered at the $4b$ sites, with the remaining sulfur occupying the $4a$ and $4c$ sites.⁴⁹ The halogen substitutions occupy the $4a$

or $4c$ sites. The Li^+ ions are located at the $48h$ and $24g$ sites, with the $24g$ sites acting as the transition state between hops from $48h$ to $48h$. Twelve $48h$ sites surround each $4c$ site, and form a cage-like structure, as depicted in Figure 2.7b.⁴⁹ The unique solution processible property of argyrodite SE open up many opportunities not only for large-scale processing, but also for achieving intimate particle contact by coating SE materials to the active material.⁵⁰

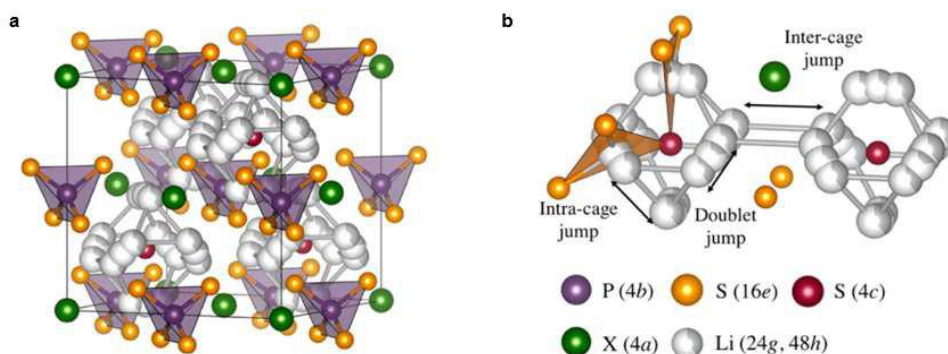


Figure 2.7 (a) Crystal structure of $\text{Li}_6\text{PS}_5\text{X}$ with $\text{X} = \text{Cl}, \text{Br}, \text{I}$. (b) The Li positions from localized cages in which multiple jump processes are possible. Reprinted with permission from Ref. 49. © 2017 American Chemical Society.

Similarly, oxide-based SE such as $\beta''\text{-Al}_2\text{O}_3$ ¹⁹ or sulfide-based SE such as Na_3PS_4 ⁵¹ for sodium ionic conductors have been reported with similar features to lithium ionic conductor, facilitating the development of solid-state sodium ion batteries.

In summary, the performance properties of polymer-based SEs (Figure 2.8a), oxide-based SEs (Figure 2.8b), and sulfide-based SEs (Figure 2.8c) are present in the radar plots. Polymer-based SEs are flexible and easy to produce a large-area membrane. However, it has a low ionic conductivity at room temperature and low oxidation voltage, which is typically less than 4 V, limiting the application of high-voltage cathode materials. Oxide-based SEs have wide electrochemical stability window, offering

intrinsic stability against electrodes. However, rigid oxide-based SEs bring challenges for large-scale fabrication and device integration. Sulfide-based SEs offer high ionic conductivity at room temperature and excellent deformability for facile device integration. However, they have narrow electrochemical stability window with poor stability against electrodes. Most sulfide-based SEs are extremely sensitive to the moisture, producing toxic H₂S gas.

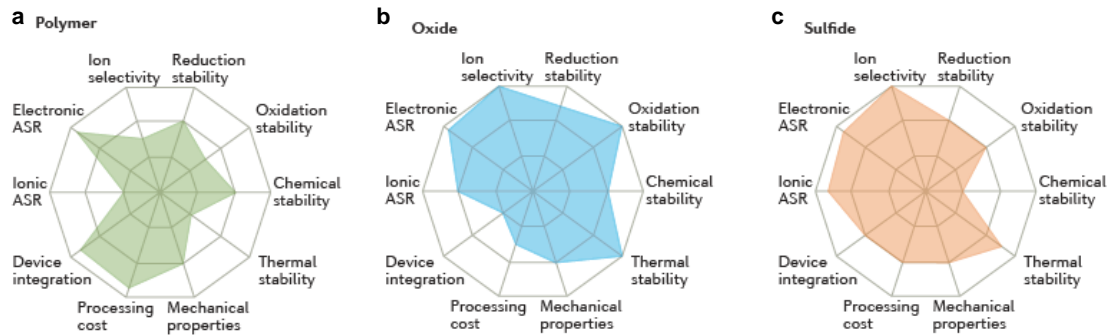


Figure 2.8 Performance comparison of three classes of solid electrolyte materials. Reprinted with permission from Ref. 16. © 2017 Springer Nature.

2.2 Architectural Design and Fabrication Approaches for Solid-State

Batteries

2.2.1 Bulk-Type Solid-State Batteries with Thick Solid Electrolyte

Unlike conventional lithium ion batteries that use porous electrodes (both cathode and anode) and porous separator with the pores filled with liquid electrolytes,⁵² Bulk-type SSBs are usually made of dense layers of electrodes and electrolyte (~500 μm thick) as shown in Figure 2.9a. The use of dense layers is not only beneficial for high volumetric energy density, but also prerequisite to for intimate interfacial contact and fast Li⁺ conduction.

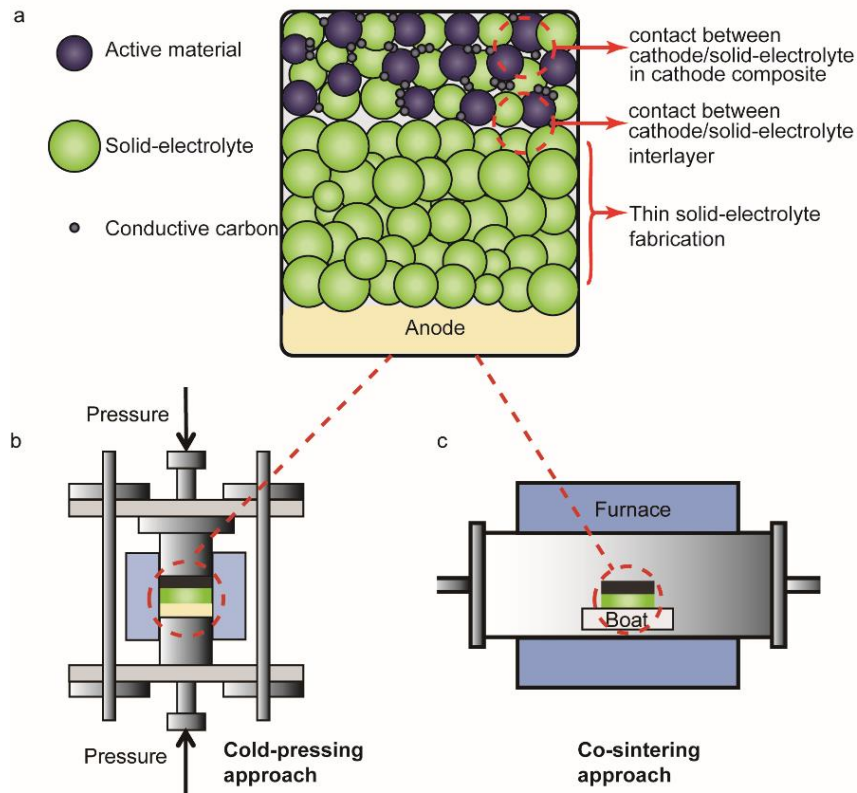


Figure 2.9 (a) Schematic representation of a typical bulk-type solid state batteries. (b) Cold-pressing for sulfide electrolyte-based SSB. (c) Sintering process for oxide electrolyte-based SSB.

The cathode of bulk-type SSBs is usually a composite layer of active material, ionically conductive solid electrolyte, and electronically conductive carbon. Conductive carbon is excluded sometimes if the electronic conductivity of active material is sufficiently high.^{47, 53, 54} A high mechanical strength for the dense cathodes is required to sustain any volume change of active materials since there is no free space to accommodate such changes. A dense layer of solid electrolyte is also required to separate cathode from anode, which is also considered as a potential solution for Li dendrite suppression and enabling high-capacity Li anode.^{55, 56} However, challenges still remain in understanding the formation of Li dendrites along the grain boundaries and/or voids in

certain solid electrolytes.⁵⁷⁻⁶⁰ If conventional anode materials such as graphite and $\text{Li}_4\text{Ti}_5\text{O}_{12}$ are used in SSBs instead of Li metal, a composite electrode could also be used as the anode.

The fabrication approach of SSBs largely depends on the mechanical property of the solid electrolyte being used. Sulfide electrolytes are compliant, and therefore both the composite electrode and the solid electrolyte layer can be prepared by cold-pressing (Figure 2.9b),⁶¹ and lithium disc can be attached on the electrolyte with minimal pressure. However, oxide-based solid electrolytes are generally much harder mechanically,⁶² and high-temperature sintering (Figure 2.9c) is usually required to ensure good contact within the solid electrolyte and at the interface between solid electrolyte and electrode. Current approaches of preparing these SSBs cannot be easily scaled up to industrial production, and the performances of most SSBs are not as good as those of liquid-electrolyte batteries. These limitations could be mainly ascribed to four challenges as summarized in Figure 2.9a: (i) achieving intimate interfacial contact between electrolyte and active material particles in the cathode composite, (ii) achieving intimate interfacial contact between cathode composite layer and electrolyte layer, (iii) fabricating thin electrolyte layer, (iv) scaling up for industrial fabrication. All of these challenges will be discussed in the following sections.

2.2.2 Sheet-Type Solid-State Batteries with Thin Solid Electrolyte

To achieve higher specific gravimetric energy (Wh kg^{-1}) and volumetric energy density (Wh L^{-1}) at cell level than those of conventional lithium ion batteries, the solid electrolyte layer must be thinner than a critical value, or “break-even thickness”.^{63, 64} For example, for a cathode with 19.5 mg cm^{-2} loading, the specific gravimetric energy break-

even thickness for oxide (LLZO) and sulfide solid electrolyte layers ($\text{Li}_{10}\text{GeP}_2\text{S}_{12}$ (LGPS)) are 45 μm and 122 μm , respectively.⁶³ It is obvious that the sulfide-based solid electrolyte with a smaller mass density (LGPS, $\rho \sim 2 \text{ g cm}^{-3}$; LLZO, $\rho \sim 5 \text{ g cm}^{-3}$) shows a larger break-even thickness. Solid electrolytes with less than 120 μm in thickness are necessary, which is still hard to be reached using traditional fabrication technology. Thus, novel thin-electrolyte fabrication methods and sheet-type SSBs are essential. Advanced techniques are emerging for fabricating thin oxide solid electrolytes with extremely conformal thin-coating quality such as pulsed laser deposition (PLD),⁶⁵ sol-gel,⁶⁶ aerosol deposition,⁶⁷ radio frequency magnetron sputtering,⁶⁸ and atomic layer deposition,⁶⁹ though some of these approaches can be high-cost and/or difficult to scale up. A scalable fabrication of thin LLZO film was demonstrated with casting-sintering flame-made LLZO nanopowders.⁷⁰ While typical LLZO pellets prepared from micropowders requires sintering at $>1000 \text{ }^\circ\text{C}$, the nanopowder-derived film was sintered at 700–800 $^\circ\text{C}$ and considerably dense and thin ($<30 \mu\text{m}$). Stacking such brittle thin films without damage could become a challenge.

The break-even thickness for sulfide solid electrolytes is larger than that for oxide solid electrolytes, thus technically more achievable.⁶³ Therefore, sulfide solid electrolytes could be more promising for high cell-level specific energy and energy density.⁷¹⁻⁷⁶ Thin sulfide solid electrolytes can be fabricated with the help of compliant polymer scaffold.⁷² Figure 2.10a shows a self-standing and bendable thin sulfide solid electrolyte layer (70 μm) fabricated by doctor-blading a Li_3PS_4 slurry on Ni foil followed by drying and then cold-pressing onto a polymer (poly(paraphenylene terephthalamide)) nonwoven scaffold which provides flexibility and toughness. The SSB assembled using this thin solid

electrolyte delivered a 3-fold increase in cell-level specific energy compared with that of a conventional pelletized SSB.⁷² Introduction of polymeric binders also provides the mechanical flexibility and adhesion between solid electrolyte particles necessary for achieving thin layer.^{73, 75} A thin solid electrolyte sheet ($\sim 70 \mu\text{m}$) was prepared by coating a slurry consisting of glassy Li_3PS_4 solid electrolyte and styrene butadiene styrene copolymer binder on a copper foil.⁷³ Since polymer binders are ion-insulating, a thermal decomposable poly(propylene carbonate) binder was designed for fabrication thin glassy Li_3PS_4 sheet ($\sim 60 \mu\text{m}$).⁷⁴ The binder could be fully removed by heat treatment at 225°C after stacking and compressing steps (Figure 2.10b). The resulted SSB exhibited cell-level specific energy of 115 Wh kg^{-1} , which was a 25% increase from that of binder-containing SSB (92 Wh kg^{-1}).⁷⁶

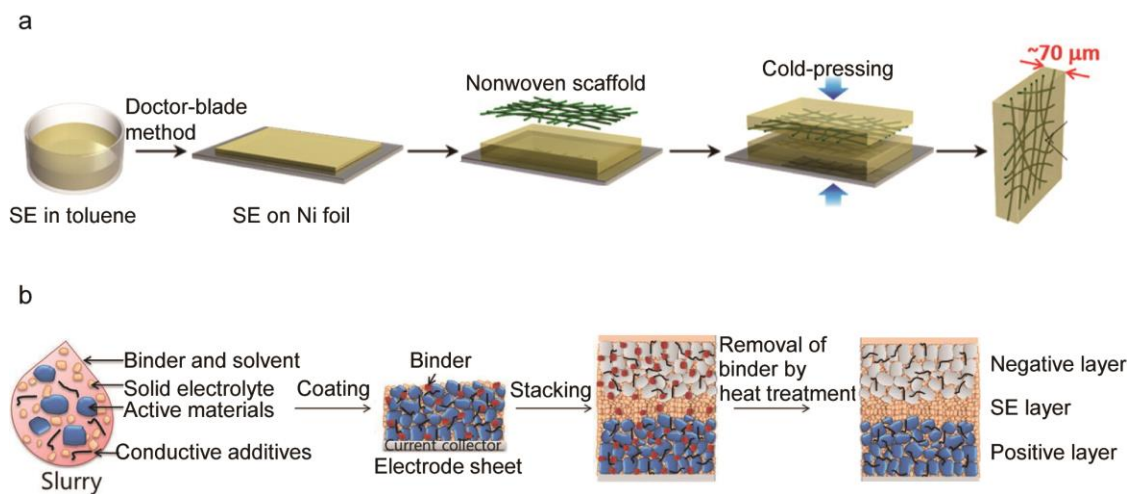


Figure 2.10 (a) Fabrication of thin solid electrolyte. Reprinted with permission from Ref. 72. © 2015 American Chemical Society. (b) Fabrication of binder-free sheet-type SSB. Reprinted with permission from Ref. 74. © 2017 Springer Nature.

2.2.3 Fabrication Approaches to Form Intimate Interparticle Contact

An ionically and electronically conductive network in the cathode composite is crucial for high-performance SSBs. Unlike conventional batteries where liquid-

electrolytes easily infiltrate into porous cathode layer to form intimate liquid-solid contact, SSBs face challenge arising from insufficient solid-solid contact, leading to large interfacial resistance between active material and solid electrolyte particles. Various approaches have been reported to increase the inter-particle contact area in the cathode composite.

A straightforward approach is to use submicrometer fine particles (Figure 2.11a) by mechanical milling of active material, conductive carbon, and solid electrolyte using a planetary ball-mill apparatus.^{77, 78} Different from hand-ground cathode composite, better contact was obtained in submicrometer particles, forming effective ions and electrons transport pathway.⁷⁹ Further enhancement of contact area can be achieved by using solution processible components (Figure 2.11b). Some of the prevailing options are soluble sulfide solid electrolytes.⁸⁰ A solution of the sulfides is either mixed with active material to form solid electrolyte-coated active material after removing solvent,⁸¹⁻⁸³ or infiltrated into a porous cathode fabricated for conventional liquid-electrolyte LIBs.⁵⁰ Both approaches allow active materials and solid electrolyte to form an intimate contact, and thus a more efficient ion transport pathway and enhanced performance compared to dry-mixed electrodes. In addition to ionic conduction, electronic pathway should also be simultaneously improved. Therefore, a solution processible conductive carbon precursor was proposed, where the soluble polyvinylpyrrolidone was coprecipitated with active material and solid electrolyte followed by thermal carbonization.⁸⁴ The mixed ionic and electronic conducting cathode composite shows intimate triple-phase contact in nanoscale, resulting in a high utilization of the active materials.

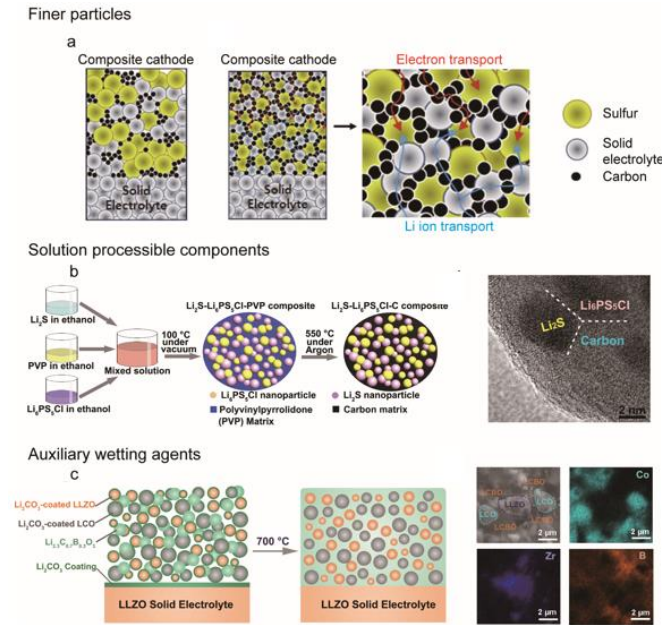


Figure 2.11 (a) Finer particles. Reprinted with permission from Ref. 79. © 2017 Elsevier. (b) Solution processible components. Reprinted with permission from Ref. 84. © 2016 American Chemical Society. (c) Auxiliary wetting agents. Reprinted with permission from Ref. 53. © 2018 Elsevier.

For solid oxide electrolytes with a low solubility in solvents, auxiliary liquid or solid wetting agents may be introduced to facilitate interfacial contact (Figure 2.11c). Liquid electrolytes are great examples of such wetting agents, though the introduction of liquids compromises the unique properties of SSBs.⁸⁵ Li_3BO_3 (LBO) is a solid wetting agent that has a melting point of 700 °C, enabling an improved interfacial contact between $\text{Li}_7\text{La}_3\text{Zr}_2\text{O}_{12}$ (LLZO) particles at a relatively low sintering temperature (790 °C).⁸⁶ The introduced LBO can also minimize element mutual-diffusion between active material and solid electrolytes, which takes place at >500 °C by physically separating the two during sintering.⁸⁷ To further improve the contact and separation, the wetting agent $\text{Li}_{2.3}\text{C}_{0.7}\text{B}_{0.3}\text{O}_3$, reacts with Li_2CO_3 and forms solid solution interphase of $\text{Li}_{2.3-x}\text{C}_{0.7+x}\text{B}_{0.3-x}\text{O}_3$ (LCBO) after sintering at 700 °C. The active material and solid electrolyte particles

are tightly glued together by the presence of LCBO.⁵³ Overall, an intimate inter-particle contact is non-trivial to the formation of ionically/electronically conductive network in cathode composite and continues to call for more effective solutions.

2.2.4 Fabrication Approaches to Form Intimate Interlayer Contact

In addition to the contact within the cathode composite, the contact between the cathode layer and electrolyte layer can also become problematic. Due to the excellent deformability of sulfide solid electrolytes, intimate contact is achieved by simple cold-pressing. However, rigid oxide solid electrolyte leaves microscopic gaps between cathode and solid electrolyte layers and cause huge interfacial resistance (Figure 2.12a). The interfacial contact can be improved by the above-mentioned wetting agent-aided co-sintering,⁸⁶ or by advanced sintering techniques such as spark plasma sintering that could lower sintering temperature (680 °C) and shorten processing time (10 min).⁸⁸ However, element mutual-diffusion inevitably occurs at these temperatures (> 500 °C) and induces resistive interphase. Insertion of auxiliary interlayers has been proposed to improve the interlayer contact without degrading interface stability (Figure 2.12a). A thin Nb layer was deposited on the surface of (LLZO) pellet by radio frequency magnetron sputtering and thermal annealing to form a Li⁺-conductive Li-Nb-O layer. The interfacial resistance between LiCoO₂ and LLZO decreased from 2600 Ω cm² to 150 Ω cm² after the introduction of the Li-Nb-O interlayer, which was attributed to the elimination of voids/cavities and the suppression of element diffusion at the interface.⁸⁹ Alternatively, an additional soft polymer electrolyte layer inserted between cathode and solid electrolyte layer can wet the oxide solid electrolyte surface, leading to a large interlayer contact area.⁹⁰

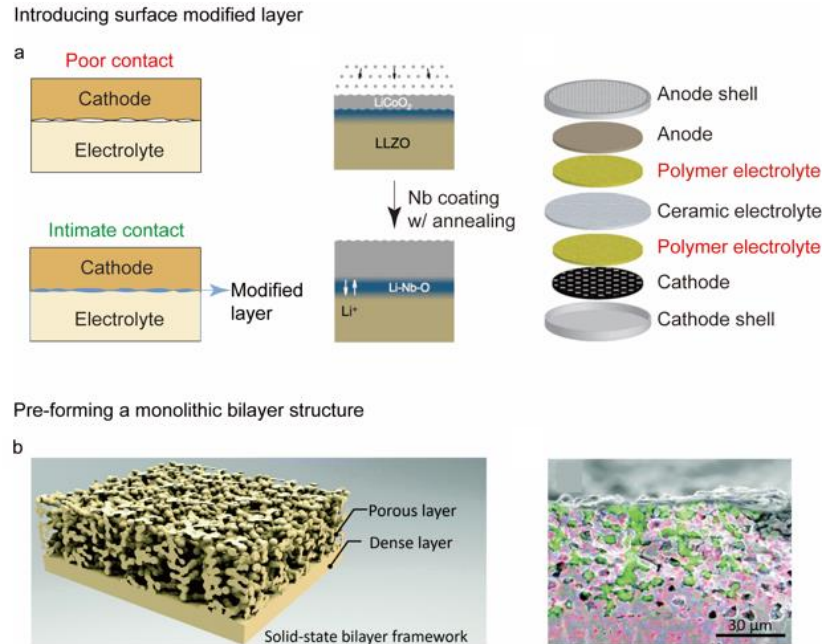


Figure 2.12 Approaches to improve contact by (a) Surface modified layer. Reprinted with permission from Ref. 89. © 2014 Elsevier. (b) Pre-formed monolithic bilayer structure. Reprinted with permission from Ref. 91. © 2017 RSC Publishing.

Besides middle layer insertion, a monolithic porous cathode–dense electrolyte bilayer architecture represents a promising strategy to provide intimate contact and continuous ion transport if the active materials in continuous porous channels can maintain good contact to the electrolyte wall during charge/discharge cycles.⁹¹⁻⁹⁴ The dense electrolyte layer was fabricated by tape-casting a LLZO powder slurry while the porous electrolyte structure in cathodes was fabricated by adding pore former (*e.g.* poly(methyl methacrylate)) in the slurry using the same method. Finally, the monolithic bilayer structure was then formed by laminating and co-sintering (Figure 2.12b).⁹¹ The continuous connected pore channels in the porous layer allow subsequent infiltration of conductive-carbon (carbon nanotube ink) and active materials (melted sulfur). The direct connection between cathode and solid electrolyte layers was demonstrated through

elemental mapping (La, red; S, green). The aforementioned approaches can also be extended to improve the interfacial contact between anode and solid electrolyte.^{95, 96}

2.3 Challenges for Large-Scale Fabrication

Bringing SSBs to the market requires scaling up from lab-scale fabrication to industrial production. In this session, we provide an overview of the main challenges for the large-scale fabrication of SSBs.

2.3.1 Material Cost

SSBs face challenges of obtaining low-cost solid electrolytes. The germanium contained in LGPS, one of the most promising solid electrolytes with ionic conductivity (12 mS cm^{-1} at room temperature) surpassing those of liquid electrolytes, is very expensive and efforts are being made to find its substitutions such as silicon and tin.⁹⁷ As for oxide solid electrolytes, the lanthanum contained in Li-garnet oxides is a concern because of its scarcity on the Earth. Developing low-lanthanum oxide solid electrolytes should be a direction. Since SSBs have hope to use Li metal as anode, the cost of Li metal should also be considered. The cost of Li foils increases with decreasing thickness.¹⁵ Similar to conventional LIBs, low-cost electrodes such as low-cobalt cathodes⁹⁸ and organic electrodes^{99, 100} are desirable for SSBs.

2.3.2 Mass Loading, Layer Thickness/Density/Uniformity

One unique advantage of SSBs is to use ultra-thick electrode because of the absence of Li-ion concentration gradient and high concentration of Li^+ per volume.¹³ A 600 μm -thick cathode layer (corresponding to a geometric capacity of 15.7 mAh cm^{-2}) has been used in SSBs with a sulfide solid electrolyte.¹⁴ Achieving homogenous

distributions of solid electrolyte, active material, and carbon in such a thick electrode is important for its performance but is also challenging. It is found that the rate performance of ultra-thick electrode is mainly limited by the ohmic resistance from ion transport, and therefore more careful optimization is needed to improve the ionic conductivity of solid electrolyte in the composite and lowering the tortuosity for Li^+ transport.¹⁴ In this regard, a sintering step might also be used for the cathode composite for sulfide solid electrolyte-based SSB's to improve the ionic conductivity of cathode composite, and considerable attention must be focused on the particle size, morphology, and distribution of solid electrolyte particles to reduce the tortuosity. Solution processing method will be helpful to achieve this purpose. Although achieving close to theoretical density in the cathode composite is strongly desired, such a dense cathode composite may suffer severe mechanical strain/stress due to volume change of the electrode.¹⁰¹ Adding polymer binders in the cathode composite can help tolerate the volumetric change of active materials during SSB cycling and prevent the formation of cracks induced by the strain/stress.¹⁰²

2.3.3 Fabrication Environment

Sulfide electrolytes are very sensitive to moisture in the air, generating toxic H_2S , and therefore the electrolytes and electrode composites have to be synthesized and processed in moisture-controlled environment. Oxide electrolytes are more stable with air. However, slight reactions between LLZO and $\text{CO}_2/\text{H}_2\text{O}$ also occur, eventually forming Li_2CO_3 on the surface.¹⁰³ The formation of Li_2CO_3 on the surface affects the performance of LLZO, *e.g.* increased interfacial resistance between electrolyte and Li.¹⁰⁴ Several approaches have been proposed to remove the Li_2CO_3 layer on LLZO,^{39, 105} but

all of these approaches should be done under CO₂ and H₂O free atmosphere to avoid the re-formation of Li₂CO₃ during processing. In addition, attention must be paid to the environment for successful sintering of oxide-based electrolytes. Subtle variations in humidity, Li vapor pressure, CO₂ and O₂ partial pressures have strong influence on the relative density and ionic conductivity of solid electrolyte.¹⁰⁶ Sintering under O₂ flow helps to achieve a high relative density and ionic conductivity of LLZO.¹⁰⁷

2.3.4 Cell Stacking

Although the utilization of solid electrolytes enables bi-polar design, stacking of large SSBs for a high-voltage cell pack has shown difficult. Currently, the stacking of multiple cells was achieved manually.¹⁰⁸ The key challenge arises from the high bending stiffness of the electrode and electrolyte layers. Adequate attentions need to be drawn to ensure the layers undamaged during stacking. Pressure or heating may be needed to ensure intimate contact between layers. In addition, the volume change of stacked cell during charge and discharge is another issue to be addressed. Polymer binders may be added in each layer and buffer space may be required to accommodate the volume change.¹⁰⁹ Fixed or variable pressure may be applied on the cell during cycling. Packaging will also require special design to address the volume change of the cells.

2.4 The True Limits: Electro-Chemo-Mechanical Incompatibilities at the Electrode-Electrolyte Interfaces

Although significant progress has been made in the development for solid-state electrolytes with high ion conductivity as shown in Figure 2.13,¹¹⁰ which looks quite promising to apply solid-state electrolytes in solid-state batteries, the development is still

advancing slowly. Indeed, high-ionic conductivity is the prerequisite for SEs, but blindly pursuing fast ionic conductor will be misleading and not hitting the nail on the head.

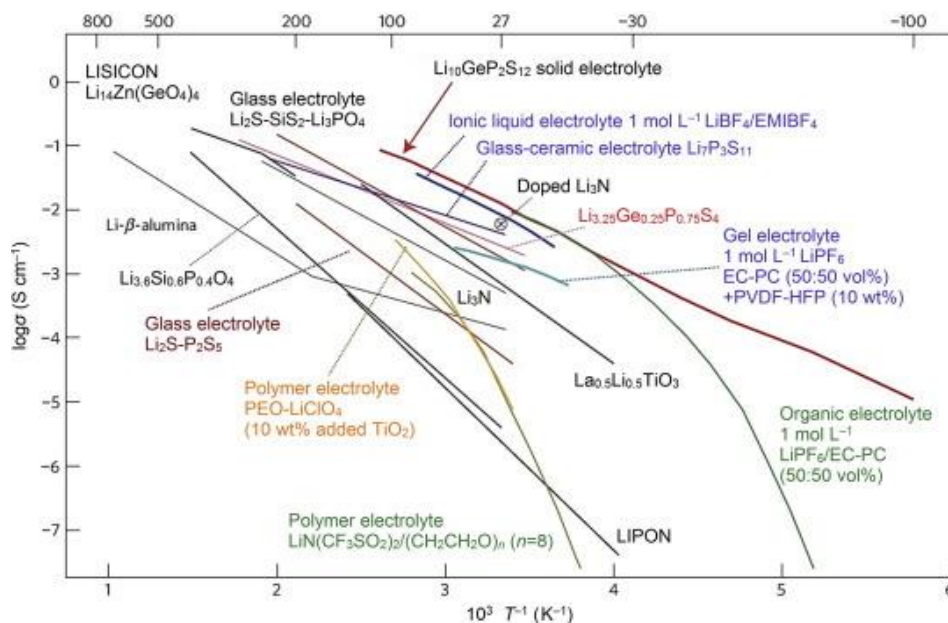


Figure 2.13 The temperature dependent ionic conductivity of reported solid-state electrolytes and conventional liquid electrolytes. Reprinted with permission from Ref. 110. © 2017 Elsevier.

Researchers started to realize that the high interfacial resistance at the electrode-electrolyte interfaces led to the large polarization, which is the main reason for the low material utilization. The impedance growth during battery cycling also led to the capacity fade. The dendrites still grew and penetrated the electrolyte and eventually caused a short circuit even though SEs exhibited good mechanical strength. The volume expansion or contraction of electrodes during battery cycling caused the loss of contact at the electrode-electrolyte interface (Figure 2.14).¹⁰⁶ All these factors resulted in an inferior electrochemical performance. In the following sections, I will introduce the origins of these interfacial challenges between solid electrolytes and electrodes in details.

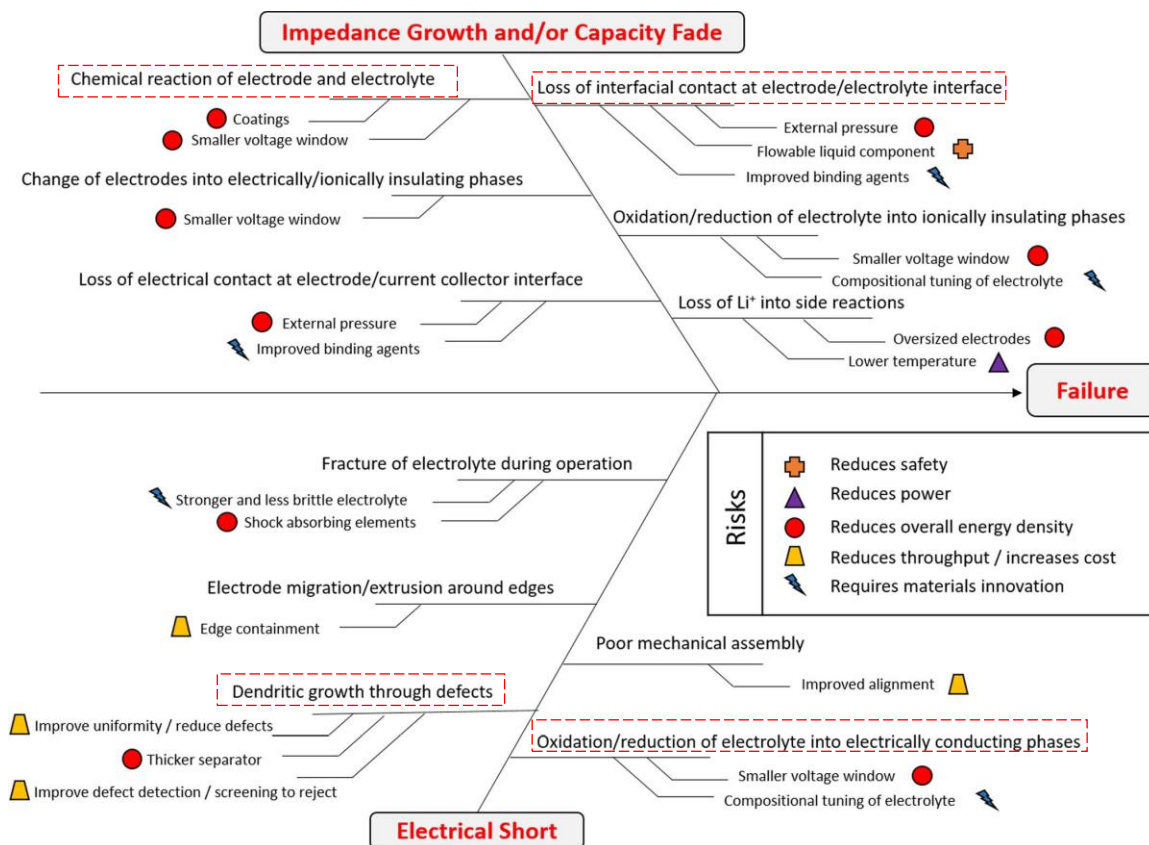


Figure 2.14 The fishbone diagram highlights contributing factors for battery failure. Reprinted with permission from Ref. 106. © 2017 The Electrochemical Society.

2.4.1 (Electro)chemical Incompatibilities

A schematic of the open circuit energy band diagram of a Li-SE-Li_xM_yO₂ solid-state system is presented in Figure 2.15.¹¹¹ The electrochemical stability window indicates the difference of the reduction and oxidation potentials of the solid electrolyte. The applied cutoff voltages during battery beyond this window will lead to the reduction and oxidation of SEs.

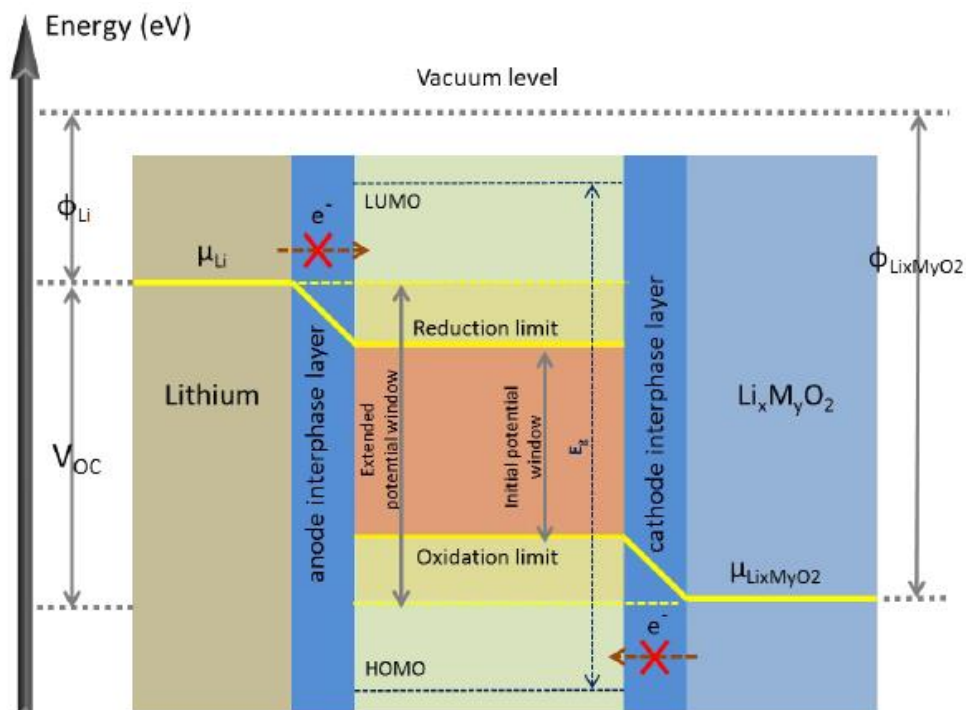


Figure 2.15 The schematic of open-circuit energy diagram for a Li-SE- $\text{Li}_x\text{M}_y\text{O}_2$ solid-state battery system. Reprinted with permission from Ref. 111. © 2019 American Chemical Society.

Ideally, the potentials of the electrodes should be within the potential window of the electrolyte to achieve stable electrochemical performance. Sulfide-based SEs are also claimed to exhibit excellent stability with wide electrochemical stability windows of 0-5 V that are interpreted from relatively inaccurate CV measurements with the Li/SE/inert blocking (stainless steel) electrode.¹¹² These experiments results in an overestimation of electrochemical stability window as the contact area between SE and inert blocking electrode is too small to detect slow decomposition reactions at the interfaces. The newly developed method using a Li-SE-SE+carbon cell is more convincible to measure the intrinsic electrochemical stability window.¹¹² Combining with the first principles calculation of the voltage profile and phase equilibria of SEs, it has been widely accepted

that SEs have much narrower electrochemical stability window than previously reported. As shown in Figure 2.15, the potentials of Li and Li_xMyO_2 are beyond the electrochemical stability window of the electrolyte, leading to the formation of reduction species at the anode-electrolyte interface and oxidation species at the cathode-electrolyte interface during battery cycling.

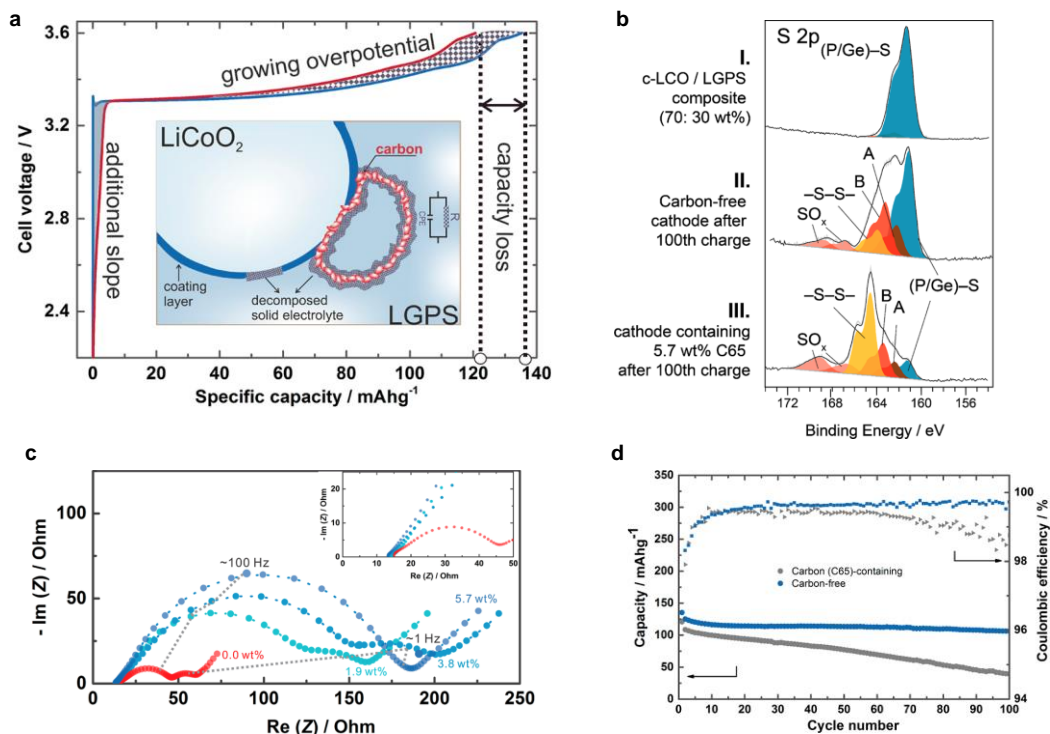


Figure 2.16 Carbon effect on the electrolyte oxidation at the cathode-electrolyte interface. Reprinted with permission from Ref. 54. © 2017 American Chemical Society.

In the cathode side, it has been demonstrated that this decomposition process can be accelerated by the carbon additive (Figure 2.16a).⁵⁴ XPS spectra detects the oxidized species (Figure 2.16b) and EIS spectra shows larger impedance (Figure 2.16c) in the carbon-containing cathode, leading to less cycling stability than that of carbon-free cathode (Figure 2.16d). Even before applying the voltage, the directly contact between

cathode and electrolyte will cause the formation of a resistive space-charge layer. Due to the stronger bonding between Li ions and oxide ions than that of sulfide ions, Li ions in sulfide-based SEs prefer to move into oxide cathodes and this ionic mutual diffusion leads to a depletion layer of Li ions and high resistance at the interface as shown in Figure 2.17a, which resulting in a large interfacial resistance.¹¹³ An electronic insulating but ionic conducting layer such as LiNbO_3 can suppress this mutual diffusion process and effectively reduce the interfacial resistance (Figure 2.17b). In the anode side, most sulfide-based SEs are also unstable against Li metal when in contact. The reduction species such as Li_3P is the mixed conducting interphase, leading to a continuous decomposition of the SEs and eventually resulting in a short circuit.

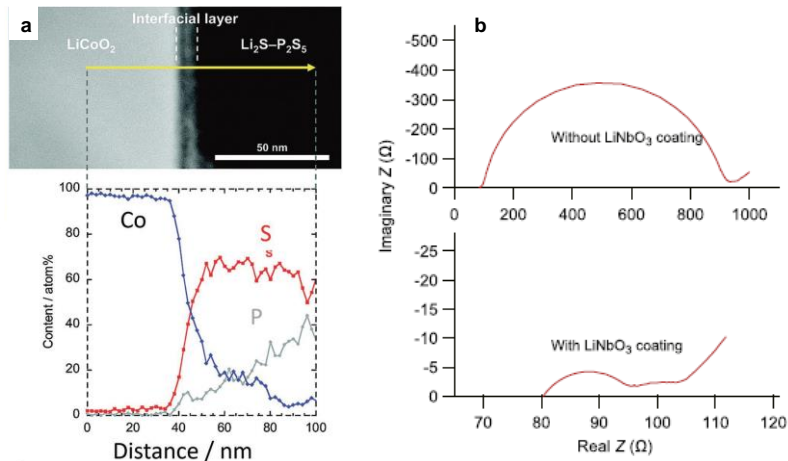


Figure 2.17 (a) The indication of mutual diffusion of elemental Co, P, and S. (b) Changes in LiCoO_2 cathode impedance with or without buffer layer. Reprinted with permission from Ref. 113. © 2010 American Chemical Society.

In comparison to the sulfide-based SEs, oxide-based SEs are relatively more thermodynamically stable with much wider electrochemical stability window, therefore more electrochemically stable against electrodes during battery cycling.¹¹⁴ However, chemical side reactions are still observed at the interface and form the undesired

interfacial species. The reaction species corresponds to La_2CoO_4 due to the mutual diffusion and retards the lithium insertion/extraction at the interface, resulting in poor electrochemical performance (Figure 2.18).¹¹⁵

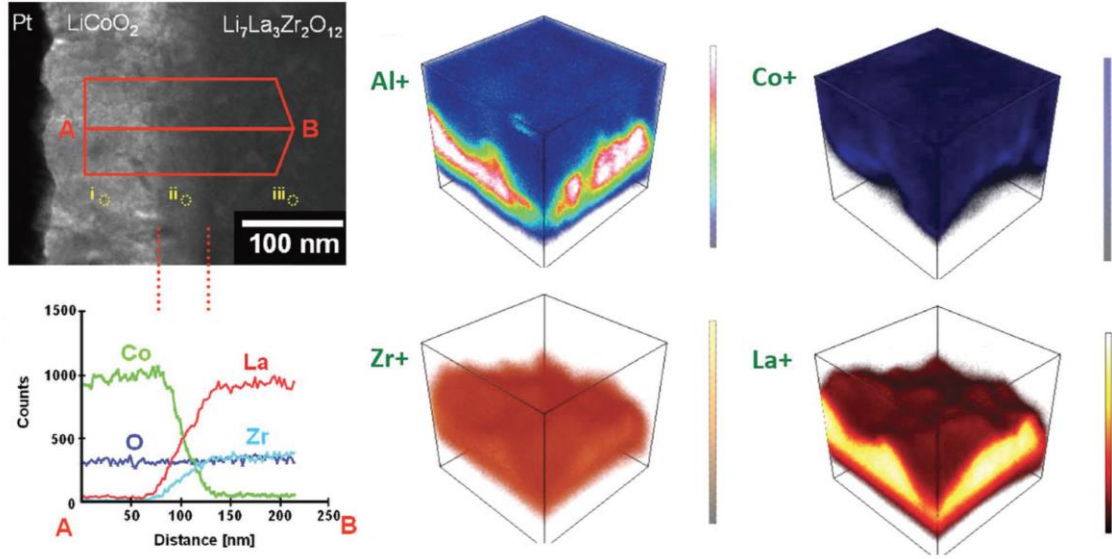


Figure 2.18 The mutual diffusion at the $\text{LiCoO}_2/\text{LLZO}$ interface. Reprinted with permission from Ref. 115. © 2011 Elsevier.

Overall, it is unrealistic to find SEs that are simultaneously stable at both the reductive potentials of ~ 0 V against Li metal anode and positive electrode potentials of ~ 4 V. A stable, ionic conducting, and electronic insulating solid electrolyte interphase (SEI) is highly desirable to improve the (electro)chemical compatibilities at the interface.

2.4.2 Mechanical Incompatibilities

Mechanical incompatibilities can be divided into two categories. The first one is the challenge between Li metal anode and solid-state electrolytes. Monroe and Newman suggested that the Li dendrite growth can be suppressed if a SE has a shear modulus two times higher than that of Li, which is 4.2 GPa.⁴⁵ However, this point of view may not be appropriate in the practical situation, because the lithium dendrite has been detected in

the garnet type LLZO as shown in Figure 2.19, despite the high shear modulus of (~60 GPa).⁵⁷ The Li dendrites were found to preferentially propagate intergranularly through the LLZO grain boundaries and result in a short circuit of cell during cycling. A similar phenomenon was also observed in the sulfide-based SEs. Chiang et al found the presence of Lithium dendrites in crystalline Li_3PS_4 as shown in Figure 2.20.⁶⁰

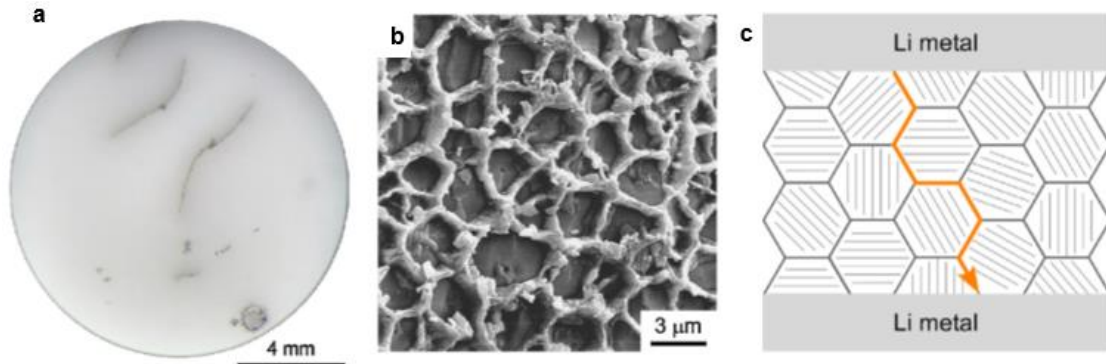


Figure 2.19 (a) The optical image of shorted LLZO. (b) SEM image of shorted LLZO. (c) Schematic of Li dendrite growth in intergranular way. Reprinted with permission from Ref. 57. © 2017 Elsevier.

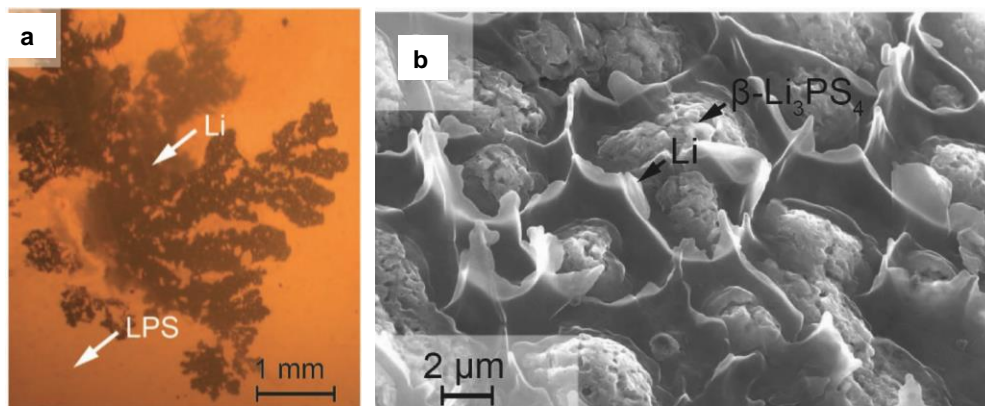


Figure 2.20 (a) The optical image and (b) SEM image of Li dendrite in Li_3PS_4 . Reprinted with permission from Ref. 60. © 2019 John Wiley and Sons.

The origins of these phenomena are due to the inhomogeneous lithium ions current flow in polycrystalline electrolytes, leading to a current redistribution and detrimental current focusing, which initiates Li dendrites at the electrolyte/Li interfaces,

especially propagating in confined spaces (voids, defects, grain boundaries, etc.) inside polycrystalline electrolytes. Therefore, the shear-modulus criterion is not the determining factor. Instead the factors such as inhomogeneous contact between SEs and Li metal, grain boundaries, voids inside SEs that influenced lithium ions transport and current flow should be carefully considered. An ideal SE material to stabilize the Li metal anode and inhibit dendrite formation will be an amorphous electrolyte that lacks grain boundaries, pores, surface flaws, and provides a homogeneous isotropic Li ion transport.

The second mechanical incompatibility is between the active material and the SE in the composite cathode. Many efforts to achieve an efficient percolation network by improving the inter-particle contact inside the composite cathode have been made and introduced in section 2.2.3. What I would like to emphasize in this section is the importance of maintaining an intimate inter-particle contact during cell cycling. The volume expansion/contraction of an active material occurs during cell cycling. As shown in Figure 2.21a, traditional inorganic active materials such as LiCoO_2 and NMC-811 experience 2-4% volume change during the charging process.¹¹⁶ Due to the high Young's moduli of these inorganic cathodes,¹¹⁷ the volume evolution during cell cycling generates huge interfacial stress and finally leads to contact loss at the cathode-electrolyte interface (Figure 2.21b), deteriorating the ionic pathway and causing the capacity decay (Figure 2.21c).

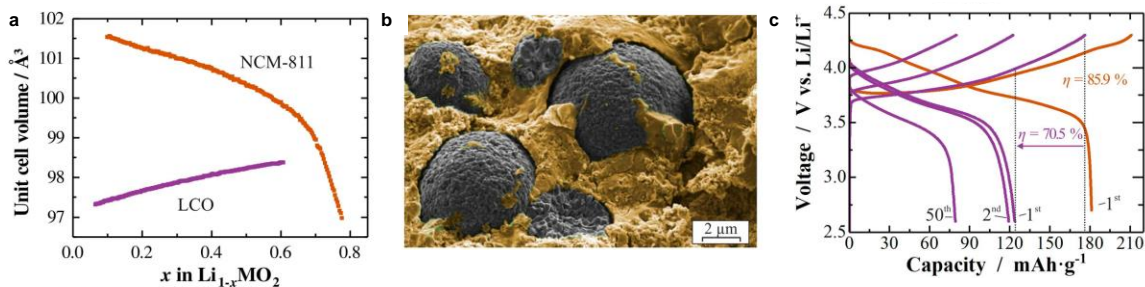


Figure 2.21 (a) Volume change of LiCoO₂ and NCM-811 during de-lithiation process. (b) Contact loss at the interface. (c) Capacity decay due to the contact loss. Reprinted with permission from Ref. 116. © 2018 American Chemical Society.

Therefore, rigid cathode is not able to compensate the mechanical changes induced by the electrodes. The “zero-strain” or soft cathodes with low Young’s modulus should be considered in the future.

2.5 Conclusions

In this chapter, the development of solid-state electrolytes was briefly reviewed. The mechanisms of ionic transport in solid-state electrolytes were illustrated. In general, lithium ions transport is achieved by their concentration and distribution of defects. In addition, a synergistic mechanism showed that Li-ions migrate through concerted migrations of multiple ions can significantly lower energy barriers with high ionic conductivity ($\sim 10^{-2}$ S/cm). I have also reviewed architectures of solid-state batteries and highlighted fabrication approaches for achieving intimate interparticle and interlayer contact. The thin solid electrolyte film is critical for high cell-level specific energy and energy density and can be prepared from soluble solid electrolytes with the aid of polymer scaffolds or binders. Limiting factors in developing high-performance solid-state batteries were discussed. Interfacial incompatibilities between electrodes and electrolyte leads to the interfacial resistance growth, large polarization, dendritic growth, and contact

loss during cell cycling, eventually resulting in an inferior performance. In chapter 3, 4, and 5, the demonstrated strategies to solve these interfacial challenges will be discussed in detail.

Chapter 3 Forming Stable Cathode-Solid Electrolyte

Interfaces with Organic Cathode

3.1 Introduction

All-solid-state sodium batteries (ASSSBs) with inorganic solid electrolytes feature higher safety and lower cost than non-aqueous liquid Li-ion batteries and are attracting worldwide attention for their potential use in large-scale energy storage applications.^{9, 32, 118} Among all currently known Na⁺-conducting solid electrolytes, sulfide-based electrolytes offer the necessary formability and conductivity.^{51, 119-121} Despite these encouraging advantages, the development and application of sulfide-based ASSSBs have been advancing slowly due to serious issues concerning the interface between oxide cathode materials and sulfide electrolytes, as highlighted in Figure 3.1a. First, the redox potentials of oxide cathodes are far above the anodic decomposition potential of Na₃PS₄ (Figure 3.1c),¹²²⁻¹²⁴ which can result in irreversible formation of a resistive layer at the interface, causing increased interfacial resistance and decreased capacity.^{125, 126} Such detrimental reactions are accelerated in the presence of conductive carbon.^{54, 112} Second, the chemical potential difference between oxide cathodes and Na₃PS₄ is large enough leading to the formation of a highly resistive space-charge layer.¹²⁷ Accordingly, electron-insulating coatings on the oxide cathodes by spray coating¹²⁸ or atomic layer deposition,¹⁰⁴ which are expensive to scale up, are commonly required to solve the abovementioned (electro)chemical issues. Third, oxide cathodes with high Young's moduli (Figure 3.1d) are prone to induce high mechanical stress during cell cycling and lose interparticle mechanical contact with the electrolyte.^{117, 129, 130}

Therefore, forming stable interfaces between cathode material and sulfide electrolyte is a critical task for the successful development of high-performance ASSSBs.¹³¹

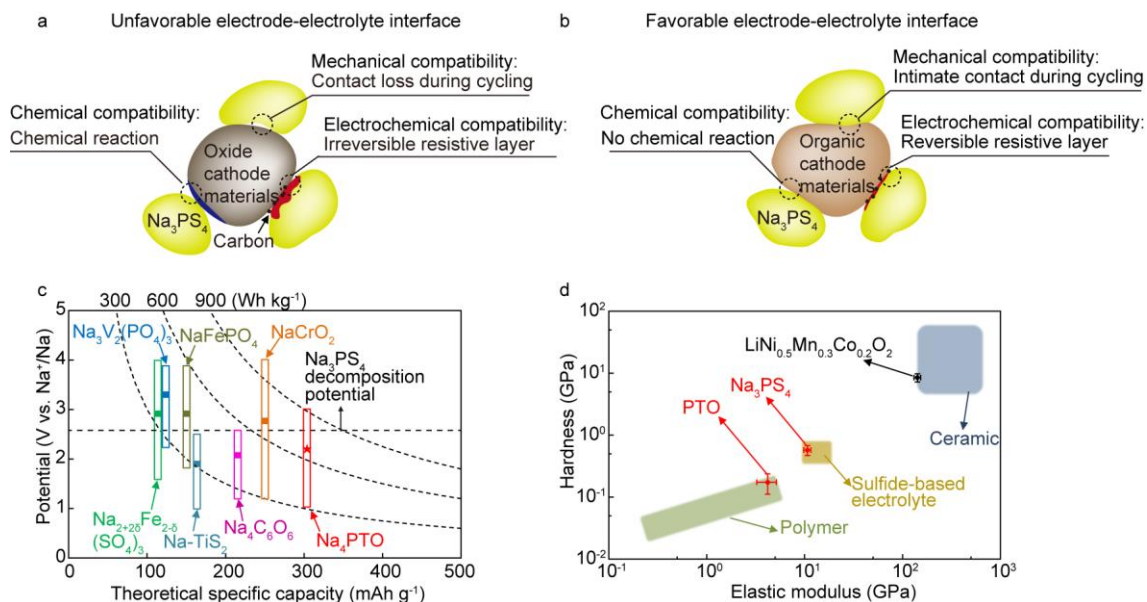


Figure 3.1 Interfacial compatibility between cathode materials and sulfide electrolytes. (a) Unfavorable interface. (b) Favorable interface. (c) Redox potential versus theoretical specific capacity. (d) Hardness-modulus plot of electrode.

Cathode materials with moderate redox potentials and low Young's moduli will thus be ideal candidates for overcoming the fundamental interfacial issues described above. Organic electrode materials represent one class of materials that is able to form a favorable electrode–electrolyte interface (Figure 3.1b) due to their unique tunable redox potentials^{99, 132-134} and mechanical compliance. We have recently presented a tailored organic cathode Na₄C₆O₆ that is (electro)chemically compatible with Na₃PS₄, thereby delivering a specific energy of 395 Wh kg⁻¹ at the active-material level and a 70% capacity retention after 400 cycles, among the highest energy and longest cycle life for ASSSBs.¹⁰⁰ To further improve the specific energy, cathode candidates with even higher capacity and voltage are desirable but will also introduce new interfacial challenges. Here

we report another quinone, pyrene-4,5,9,10-tetraone (PTO),^{135, 136} with a theoretical specific capacity of 409 mAh g⁻¹ (or 303 mAh g⁻¹ for the sodiated form Na₄PTO) and a higher working potential of 2.2 V (vs. Na⁺/Na). A notable difference of PTO from Na₄C₆O₆ is that its end-of-charge potential (3.1 V vs. Na⁺/Na) exceeds the anodic decomposition potential of electrolyte, resulting in partial oxidation of Na₃PS₄. To address this challenge, we tweaked the carbon ratio in the composite cathode to achieve reversible Na₃PS₄ oxidation and reduction as revealed by in-situ electrochemical impedance spectroscopy (EIS), ex-situ X-ray photoelectron spectroscopy (XPS), and time-of-flight secondary ion mass spectrometry (ToF-SIMS) measurements. In addition, the Young's modulus of PTO (4.2 ± 0.2 GPa; Figure 3.2) is approximately two orders of magnitude lower than that of oxide cathodes (100–200 GPa)¹³⁷, which promises effective accommodation of interfacial stress and consistently intimate interfacial contact for solid-state batteries.

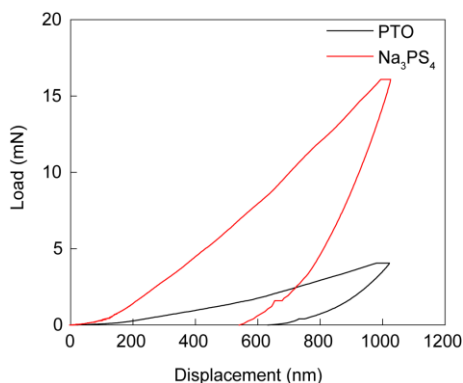


Figure 3.2 Load-displacement response of indentation of PTO and Na₃PS₄.

These properties enable PTO-based cells to deliver a high specific energy (587 Wh kg⁻¹) and a record cycling stability (89% retention over 500 cycles) for ASSSBs reported to date (Table 3.1). The understandings obtained and the generalizable strategies

established via the success of PTO make this work significant for energy storage.

Table 3.1 Comparison of electrochemical performance of previously reported intercalation-type cathode materials and this work for all-solid-state sodium cells.

Cathode materials	Electrolyte	Anode Materials	T (°C)	Cycles/Reversible capacity (mAh/g)/Rate	Reference
TiS ₂	Na ₃ PS ₄	Na ₃ Sn	RT	10/90/0.01C	Hayashi et al., 2012 ⁵¹
TiS ₂	Na _{2.9375} PS _{3.9375} Cl _{0.0625}	Na	RT	10/70/0.1C	Chu et al., 2016 ¹³⁸
TiS ₂	Na ₃ P _{0.62} As _{0.38} S ₄	NaSn	80	9/103/0.02C	Yu et al., 2017 ¹³⁹
TiS ₂	Na _{3.75} Sn _{0.75} Sb _{0.25} S ₄	Na ₃ Sn	30	40/165/0.18C	Heo et al., 2018 ¹⁴⁰
TiS ₂	Na _{2.7} Ca _{0.15} PS ₄	Na ₃ Sn	30	120/160/0.11C	Moon et al., 2018 ¹⁴¹
Na ₃ V ₂ (PO ₄) ₃	Na _{1.9} Zn _{1.9} Ga _{0.1} TeO ₆	Na	80	10/75/0.2C	Li et al., 2018 ¹⁴²
Na ₃ V ₂ (PO ₄) ₃	Na _{3.3} Zr _{1.7} La _{0.3} Si ₂ PO ₁₂	Na	80	40/75/0.1C	Zhang et al., 2017 ¹⁴³
NaFePO ₄	Na ₃ Zr ₂ Si ₂ PO ₁₂	Na	RT	3/5/0.2C	Kim et al., 2015 ¹⁴⁴
Na _{2+2δ} Fe _{2-δ} (SO ₄) ₃	Na _{3.1} Sn _{0.1} P _{0.9} S ₄	NaTi ₃ O ₇	80	100/70/2C	Rao et al., 2017 ¹⁴⁵
NaCrO ₂	Na ₃ PS ₄	Na ₁₅ Sn ₄	RT	20/60/0.01C	Hayashi et al., 2014 ¹²⁶
NaCrO ₂	Na ₃ SbS ₄	Na ₃ Sn	RT	20/60/0.03C	Banerjee et al., 2016 ¹²⁵
NaCrO ₂	Na ₂ (B ₁₂ H ₁₂) _{0.5} (B ₁₀ H ₁₀) _{0.5}	Na	60	250/65/0.2C	Duchêne et al., 2017 ¹⁴⁶
Na ₄ C ₆ O ₆	Na ₃ PS ₄	Na ₁₅ Sn ₄	60	400/107/0.2C	Chi et al., 2018 ¹⁰⁰
PTO–NR	Na₃PS₄	Na₁₅Sn₄	60	500/242/0.3C	This work

3.2 Experimental Procedures

3.2.1 Synthesis of Electrodes and Electrolyte

Na_3PS_4 glass-ceramic powders were prepared via mechanochemical reaction and heat treatment. In brief, 1.02 g of Na_2S (Alfa Aesar, 99.9%) and 0.98 g of P_2S_5 (Sigma–Aldrich, 99%) were ball milled in a 250-mL argon-protected stainless-steel jar containing stainless-steel milling balls ($2 \times \Phi 15$ mm and $20 \times \Phi 10$ mm) at 500 rpm for 2 hours to obtain amorphous powders, which was further treated under vacuum at 260°C for 2 hours to obtain glass-ceramic Na_3PS_4 . Na_3PS_4 has been shown unstable with Na metal;¹⁴⁷ therefore, a $\text{Na}_{15}\text{Sn}_4$ alloy (~ 0.1 V vs. Na^+/Na) was prepared following the literature.¹⁴⁸ PTO–B was synthesized following the previously report.¹³⁶ PTO–MP was prepared by ball milling 200 mg of PTO powders in a 100-mL agate milling jar at 400 rpm for 10 hours. PTO–NR was synthesized using a chemical antisolvent precipitation method. Briefly, 50 mg of PTO–B was dissolved in 13 mL of tetrahydrofuran (THF, anhydrous, $\geq 99.9\%$, Sigma–Aldrich) and quickly injected into 70 mL of deionized water. After sonication for 10 min, yellow precipitates were collected by centrifuging at 10,000 rpm for 15 min and subsequent vacuum drying overnight.

3.2.2 Materials Characterization

Nanoindentation measurements were performed on the surface of cold-pressed Na_3PS_4 and PTO pellets using a nanoindenter (G200, Agilent Technologies) in an argon-filled glove box. The modulus and hardness were extracted from the load-displacement curves according to the standard Oliver and Pharr method.¹⁴⁹ Indentations under displacement control at a maximum depth of 1000 nm were conducted at 10 different

locations using a standard Berkovich tip. The loading, holding, and unloading time is 10 s, 5 s, and 10 s, respectively. The cross sections of composite cathodes utilized for SEM were observed in a FIB-SEM (FEI, Helios NanoLab 660 DualBeam) using an argon-ion beam polisher. Chemical information was obtained by FT-IR spectroscopy (Nicolet iS5). The surface composition of the cycled composite cathodes was investigated by XPS (Physical Electronics PHI 5700) and ToF-SIMS (ION-TOF). All reported binding energy values were calibrated to the C 1s peak at 284.8 eV. A sputtering ion beam (Cs^+ with 1 keV ion energy) was used for depth profiling of ToF-SIMS in negative polarization mode. To minimize air exposure, all samples were transferred from an argon-filled vessel to the analysis chamber.

3.2.3. Fabrication of All-Solid-State Cells

The PTO– Na_3PS_4 –C composite cathodes were mixed using an agate mortar and pestle with weight ratios of 20:(80–x):x, where the x values are 0, 5, 10, 20, 28, and 33. The Na_3PS_4 –C composite cathode was mixed with a weight ratio of 70:10. To assemble the cell, 150 mg of electrolyte powder was filled into a polyetherether–ketone (PEEK) cell die with a diameter of 13 mm and pressed at a pressure of 75 MPa to form a pellet. Five milligrams (5 mg) of the composite cathode (active material loading ~ 1.0 mg) was uniformly distributed on one side of the Na_3PS_4 pellet, and $\text{Na}_{15}\text{Sn}_4$ powder (100 mg) was added to the other side of the pellet and then pressed together at a pressure of 375 MPa. The over-dimensioned $\text{Na}_{15}\text{Sn}_4$ was necessary for fabrication as the $\text{Na}_{15}\text{Sn}_4$ layer easily cracked after cold-pressing at such high pressure if less $\text{Na}_{15}\text{Sn}_4$ was used. During the cell testing, the cell was subjected to a torque of 20-inch-pound on each of three screws, corresponding to an initial pressure of ~ 0.5 MPa applied on the cell.

3.2.4 Electrochemical Measurements

All galvanostatic discharge–charge cycles were performed in the potential range of 1.1–3.1 V vs. Na^+/Na at 60°C using a battery tester (LAND CT–2001A). Specific capacity is calculated based on the mass of active material in the composite cathode. EIS measurements were carried out using an electrochemical workstation (VMP3, Bio–Logic Co.) during galvanostatic cycling at the following potentials: 2.0 V, 1.7 V, 1.5 V, 1.3 V, and 1.1 V vs. Na^+/Na during the discharge process; and 1.7 V, 2.0 V, 2.5 V, 2.8 V, and 3.1 V vs. Na^+/Na during the charge process. Each measurement was preceded by a rest period of 30 min for equilibrium. A bias of 5 mV was applied for the measurement in the frequency range of 1.0 MHz to 0.1 Hz.

3.3 Effect of Carbon Ratio on the Electrochemical Performance

PTO molecule theoretically undergoes a four-electron transfer reaction that corresponds to a specific capacity of 409 mAh g^{-1} (Figure 3.3a). To experimentally verify the capacity of PTO but to minimize possible oxidation of Na_3PS_4 when charging above 2.7 V vs. Na^+/Na , we first adopted a carbon-free composite cathode. We found that a half cell with the configuration of PTO– $\text{Na}_3\text{PS}_4/\text{Na}_3\text{PS}_4/\text{Na}_{15}\text{Sn}_4$ can deliver a reversible capacity of 376 mAh g^{-1} and a near-unity first-cycle coulombic efficiency at a low rate (0.01C) (Figure 3.3b).

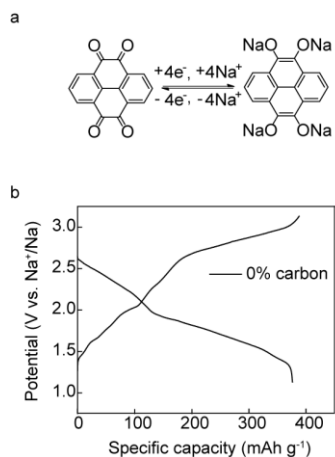


Figure 3.3 Electrochemical reaction and voltage profile of PTO as a cathode. (a) Molecular structure of PTO and its electrochemical reaction. (b) First-cycle voltage profile of a PTO- $\text{Na}_3\text{PS}_4/\text{Na}_3\text{PS}_4/\text{Na}_{15}\text{Sn}_4$ half cell at 0.01C at 60°C

Next, to test at more practical current densities, composite cathodes with different carbon ratio (0, 5, 10, 20wt%) were prepared. Figure 3.4a shows the first-cycle galvanostatic voltage profiles of the corresponding cells tested at 0.1 C. When no carbon was present, the cell only delivered 49% of its theoretical capacity, or 53% of that observed at 0.01 C, and a low coulombic efficiency of 75%. When carbon was added, the charge capacity increased and reached a maximum of 314 mAh g^{-1} at 10 wt% carbon (Figure 3.4c). The first-cycle coulombic efficiency increased as carbon ratio increased from 0 to 5 wt% but then decreased as carbon ratio increased further (Figure 3.4c). To understand the carbon effect on overall cell performance, we used XPS to study the degree of electrolyte oxidation at different carbon ratio (Figure 3.4b). All samples showed two S 2p doublets at 160.7 (blue) and 161.9 eV (orange), corresponding to the P-S-Na and P=S bonds in Na_3PS_4 , respectively.^{100, 147} When the carbon ratio was higher than 5 wt%, new peaks (green) appeared at a higher binding energy of 162.7 eV. According to a similar study on Li_3PS_4 from Janek's group,¹⁵⁰ we assigned these peaks to the P-[S]_n-P

($n=1, 2$) bond in $\text{Na}_4\text{P}_2\text{S}_8$, $\text{Na}_4\text{P}_2\text{S}_7$, and $\text{Na}_2\text{P}_2\text{S}_6$, which are oxidation products of Na_3PS_4 . When the carbon ratio increased to 10 and 20 wt%, we saw intensity of the new peaks increased, indicating more ionically resistive phases were produced. Therefore, the low efficiency for carbon-containing composite cathodes are resulted from inefficient ionic conduction at the interface due to oxidation of Na_3PS_4 .

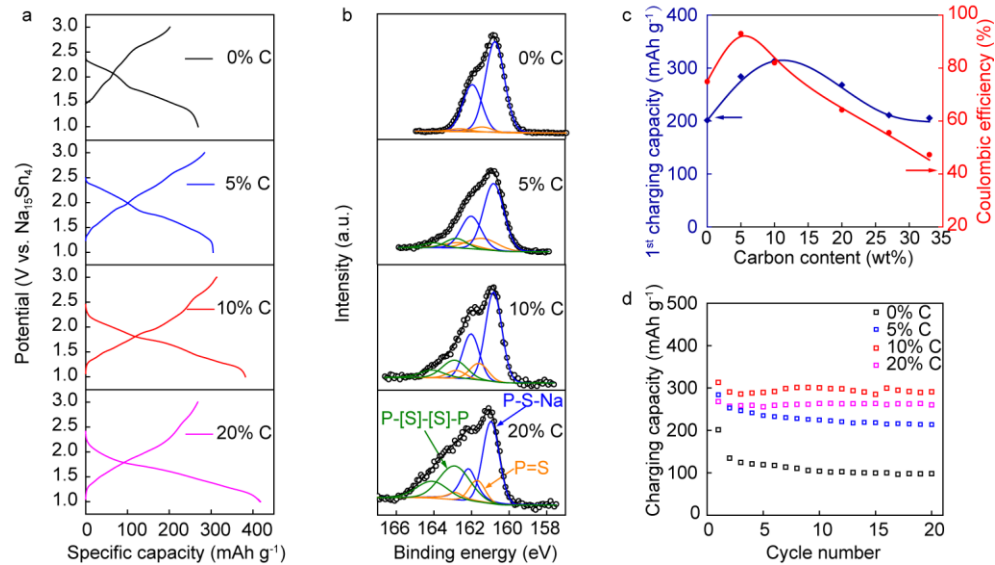


Figure 3.4 (a) First-cycle voltage profiles. (b) XPS spectra (S 2p) of the composite cathodes. (c) Capacity and coulombic efficiency vs. carbon ratio. (d) Charging capacity and coulombic efficiency vs. cycle number.

The composite cathode with 10 wt% carbon showed the best combination of high initial charge capacity (314 mAh g^{-1}), first-cycle coulombic efficiency (82%), and capacity retention (93% after 20 cycles) among the compositions investigated (Figure 3.4d). These observations suggest that (i) incorporation of carbon into the composite cathode is indispensable for providing sufficient electron transport and (ii) too much carbon in the composite cathode causes significant accumulation of resistive products at the interface, thus leading to large capacity loss in the first cycle and the decreased discharge potential in first few cycles. Therefore, composite cathodes with mass ratio of

PTO:Na₃PS₄:carbon 2:7:1 and active material loading $\sim 1 \text{ mg cm}^{-2}$ were used in the following experiments. The mass loading of Na₁₅Sn₄ is 100 mg cm^{-2} . All cells were tested under 60°C and 0.5 MPa during cycling.

3.4 Investigation of Compatible Cathode-Electrolyte Interface

To probe the evolution of the cathode–electrolyte interface, we performed in-situ EIS measurements for PTO-based cells in the first three cycles. Each EIS measurement was preceded by a rest period of 30 min to allow for reaching equilibrium. Figure 3.5a shows the galvanostatic voltage profiles and the A_w extracted from the low-frequency EIS spectra (1.0 Hz–0.1 Hz) at each selected potential (Figure 3.5b–3.5c). During the first cycle, A_w decreased from $225 \Omega \text{ s}^{-1/2}$ (corresponding to a Na-diffusion coefficient D_{Na^+} of $1.46 \times 10^{-11} \text{ cm}^2 \text{ s}^{-1}$) at open circuit to $47 \Omega \text{ s}^{-1/2}$ at 1.1 V vs. Na⁺/Na during discharge and then gradually increased to $154 \Omega \text{ s}^{-1/2}$ at 2.5 V vs. Na⁺/Na during charge. Once reached 2.8 V vs. Na⁺/Na, above the decomposition potential of Na₃PS₄, we saw a significant increase of A_w to 550 and further to $1897 \Omega \text{ s}^{-1/2}$ (D_{Na^+} of $1.73 \times 10^{-12} \text{ cm}^2 \text{ s}^{-1}$) at 3.1 V vs. Na⁺/Na. Interestingly, A_w reverted to $45 \Omega \text{ s}^{-1/2}$ at 2.0 V vs. Na⁺/Na during the second discharge and remains low until the next charging process. The same impedance evolution was observed during the second and third cycles. It is noteworthy that even though PTO's end-of-discharge potential of 1.1 V vs. Na⁺/Na exceeds the thermodynamic cathodic decomposition potential of Na₃PS₄ (1.55 V vs Na⁺/Na),¹²² A_w values stayed low at 1.5 V, 1.3 V, and 1.1 V vs. Na⁺/Na, indicating the probable cathodic instability at PTO–Na₃PS₄ interface does not produce resistive passivation layer and further degrading the performance.

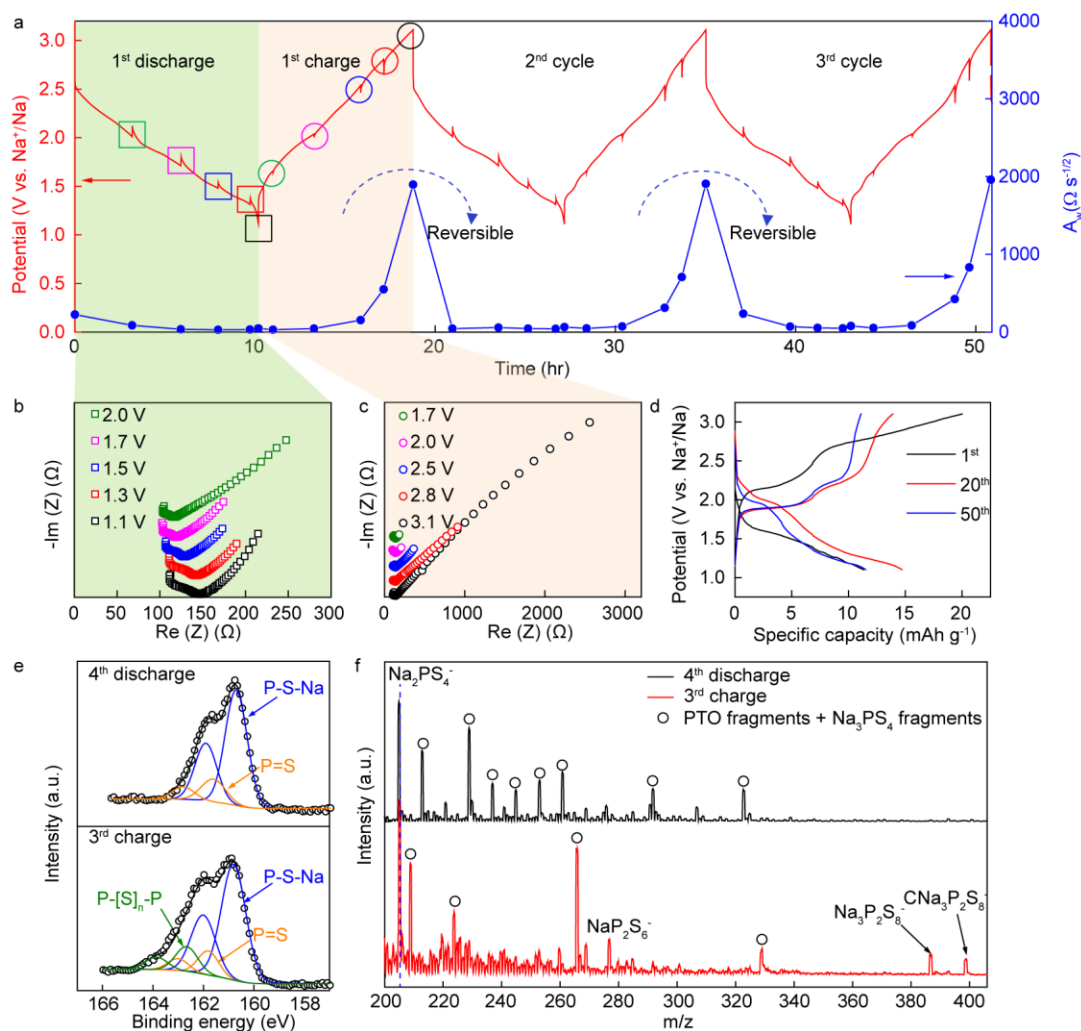


Figure 3.5 (a) In-situ EIS measurement. Impedance spectra recorded during (b) First discharge and (c) First charge. (d) Voltage profile without PTO in the composite cathode. (e) XPS spectra. (f) ToF-SIMS spectra.

Therefore, we observed for the first time a reversible interfacial resistance evolution during cell cycling. Such a reversible behavior is the consequence of reversible conversion between conductive Na_3PS_4 phase and resistive phases, which occurs within the operation potential range of PTO (1.1–3.1 V vs. Na^+/Na). In contrast, oxide cathode materials with higher operation potentials, *e.g.* NaCrO_2 (up to 4.0 V vs. Na^+/Na), result in irreversible formation of low conductivity species such as S^0 at higher voltages,³³ which

is responsible for capacity fading.

As the Na_3PS_4 decomposition also contributes to the cathode capacity, a control cell with a composite cathode containing only Na_3PS_4 and carbon was fabricated to quantify the contribution. As shown in Figure 3.5d, Na_3PS_4 alone showed a specific capacity of less than 20 mAh g^{-1} . Therefore, we can conclude that the high specific capacities of PTO-based composite cathodes were mainly contributed by PTO. To provide direct evidence of the identity and reversibility of oxidation products of Na_3PS_4 , we conducted ex-situ XPS and ToF-SIMS on two cycled cells as shown in Figure 3.5e and 3.5f. The S 2p XPS spectra of the composite cathode after the third charge showed new peaks (green) that corresponded to the $\text{P}-[\text{S}]_n-\text{P}$ bond, indicating partial oxidation of Na_3PS_4 . After the following discharge, these peaks disappeared and S 2p spectra became similar to that of pristine Na_3PS_4 . The ToF-SIMS spectra of the fully charged electrode showed peaks at 277, 387, and 399 m/z corresponding to NaP_2S_6^- , $\text{Na}_3\text{P}_2\text{S}_8^-$, and $\text{CNa}_3\text{P}_2\text{S}_8^-$ respectively, indicating the formation of $\text{Na}_2\text{P}_2\text{S}_6$ and $\text{Na}_4\text{P}_2\text{S}_8$. None of these peaks retained after the fourth discharge, indicating a reversible transformation of the oxidized products back to Na_3PS_4 . Overall, Na_3PS_4 oxidation and $\text{Na}_4\text{P}_2\text{S}_8/\text{Na}_2\text{P}_2\text{S}_6$ reduction are highly reversible between 1.1 and 3.1 V vs. Na^+/Na , guaranteeing a reversible interface that is beneficial for cycling stability of cells.

Due to the suitable deformability of sulfide electrolytes,¹²¹ intimate interparticle contact can be achieved for most composite cathodes containing sulfide electrolytes by simple cold-pressing. Additionally, solution processed solid electrolyte can create a uniform coating around the cathode particles to achieve intimate interparticle contact.¹⁴⁶ However, maintaining such an intimate contact upon cycling is challenging for oxide

cathodes which have high Young's moduli. Stress-induced cracks were observed in cycled cathodes at the active material particle–electrolyte interface.¹²⁹ In contrast, PTO shows intimate contact with Na₃PS₄ before (Figure 3.6a) and after 200 cycles (Figure 3.6b), which is attributed to the small Young's modulus of PTO that helps the particles readily accommodate the mechanical stress generated at the interface upon cycling. The cell therefore shows 304 mAh g⁻¹ specific capacity at 0.1 C with 97% capacity retention after 100 cycles. To the best of our knowledge, this consistently intimate interfacial contact is revealed for the first time for solid-state batteries. Low-modulus electrode materials should receive more attention as an effective approach to mitigate capacity fading originated from mechanically induced contact loss.

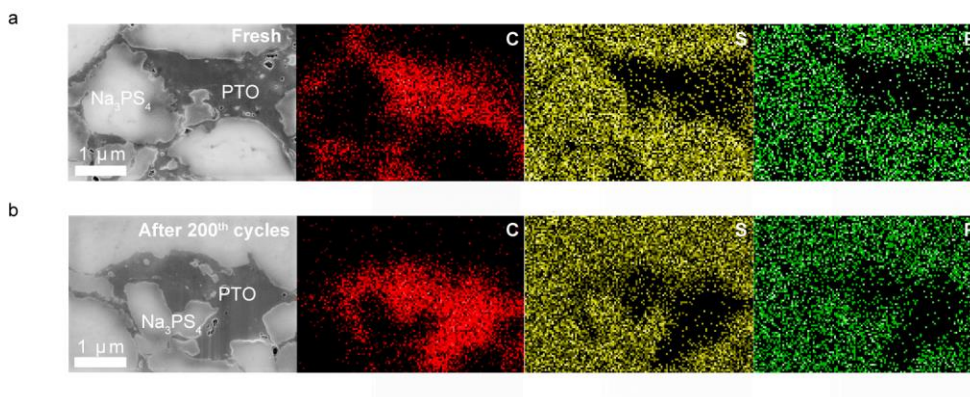


Figure 3.6 Cross-sectional SEM images and elemental mapping of (FIB)-milled composite cathodes. (a) Before cycling. (b) After 200th cycles.

3.5 Electrochemical Performance of Organic Cathode-Based All-Solid-State Batteries

Size effect of electrode materials on the battery kinetics is well known.^{151, 152} Smaller electrode particles lead to shorter ionic and electronic pathways. Therefore, we prepared PTO micropellets (PTO–MP) and PTO nanorods (PTO–NR) by mechanical

milling and a chemical antisolvent precipitation method, respectively. Scanning electron microscopy (SEM) images in Figure 3.7a–3.7c show a significant particle size reduction: bulk PTO (PTO-B) particles are 50–100 μm in diameter, while PTO-MP has an average diameter of 5 μm and a thickness of 1 μm , and PTO-NR is ~ 1 μm in length and ~ 300 nm in thickness. The rate performance of differently sized PTO is shown in Figure 3.7d–3.7g. PTO-NR exhibited the best rate capability, with capacity of 322 mAh g^{-1} at 0.1C and 200 mAh g^{-1} at 1C. PTO-NR allows the cell to achieve a specific energy of 587 Wh kg^{-1} at 0.1C, a specific power of 335 W kg^{-1} at 1C, (Figure 3.7h), and 89% capacity retention after 500 cycles at 0.3C (Figure 3.7i).

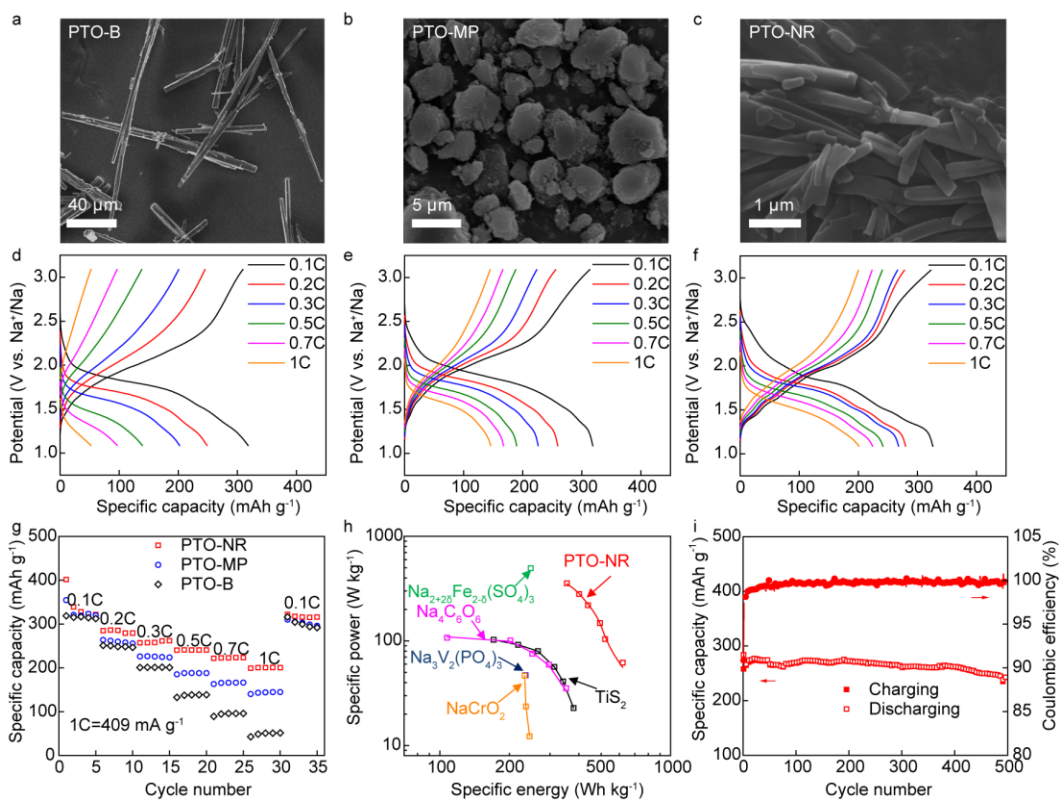


Figure 3.7 (a-c) Different morphologies of PTO and (d-f) their corresponding electrochemical performance. (g) Rate capabilities. (h) Ragone plot. (i) Capacity and coulombic efficiency versus cycle number.

3.6 Conclusions

In summary, we have demonstrated the capability of an organic cathode material PTO to enable high-energy, high-power, and long-cycle-life ASSSBs. We tweaked the carbon ratio in the composite cathode to achieve the best combination of high initial charge capacity, first-cycle coulombic efficiency, and capacity retention. We also observed for the first time a reversible cathode-electrolyte interfacial resistance evolution during the cell cycling. We have further shown that PTO with a Young's modulus two orders of magnitude smaller than that of oxide cathodes, is capable of overcoming mechanical failures and maintaining intimate interparticle contact upon cycling. As a result, reversible resistance and intimate contact at the electrode-electrolyte interface form the basis of achieving record specific capacity and cycling stability of any ASSSBs reported to date. The improved performance and deeper understanding of the electrode-electrolyte interface are shaping up a bright future for ASSSBs and opening up new opportunities for other solid-state devices.

Chapter 4 An Electrochemomechanically Stable Glassy

Electrolyte

4.1 Introduction

In previous work, the $\text{Na}_{15}\text{Sn}_4$ alloy was used as anode material as Na metal was not stable against sulfide-based solid-state electrolytes. However, the cell voltage was limited due to the potential of $\text{Na}_{15}\text{Sn}_4$ was 0.1 V vs. Na^+/Na . Therefore, solid-state sodium metal batteries (SSMBs) using earth-abundant sodium metal anodes are attracting worldwide research attention.^{2, 9, 153} So far, the high-temperature Na-S battery is the only successful example of a commercialized Na metal battery for grid-scale energy storage.¹⁵⁴ However, its high working temperature of >300 °C, where both Na and S are in the molten state, dramatically increases operational cost and poses safety hazards.¹⁵⁵ In contrast, the SSMBs working at ambient temperature using solid Na metal anode are more desirable in a broader range of applications, whose realization is highly relied on the development of the Na-ion solid electrolytes (SEs). In addition to high ionic conductivity, an ideal Na-ion SE should also be chemically and electrochemically stable with Na metal, and mechanically robust to resist Na dendrites. Furthermore, the SEs for commercial applications must simultaneously meet the stringent requirements of low cost and facile fabrication.¹⁶ The currently developed Na-ion SEs mainly include two categories,¹¹⁹ oxide and sulfide, as illustrated in Figure 4.1a and 4.1b, respectively. Oxide-based SEs such as $\beta''\text{-Al}_2\text{O}_3$ and NASICON-type ceramics exhibit excellent chemical stability towards Na metal, nevertheless, they are subjected to high processing temperatures and poor wettability with Na metal due to their rigid and rough surface.^{131,}

^{156, 157} Particularly, during the Na deposition process, metallic dendrites preferentially propagate along the oxide-based SEs' distinct grain boundaries, leading to eventual short-circuiting,^{106, 158} although these SEs provide more than adequate moduli to resist dendrites (Figure 4.1a). Sulfide-based SEs (e.g., heat-treated Na_3PS_4 ⁵¹ and Na_3SbS_4 ¹⁵⁹) have soft surfaces that effectively wet with Na metal. They also exhibit less well-defined grain boundaries due to the existence of a certain quantity of a glassy phase (5~50 vol%), which can mitigate the dendrite growth. However, these SEs suffer from continuous decomposition when contact with Na,^{127, 147, 160, 161} which leads to the unstable interface (Scheme 4.1b). For these reasons, Na alloys (e.g. $\text{Na}_{15}\text{Sn}_4$) are commonly applied as an alternative anode at the expense of voltage and cost.^{122, 162}

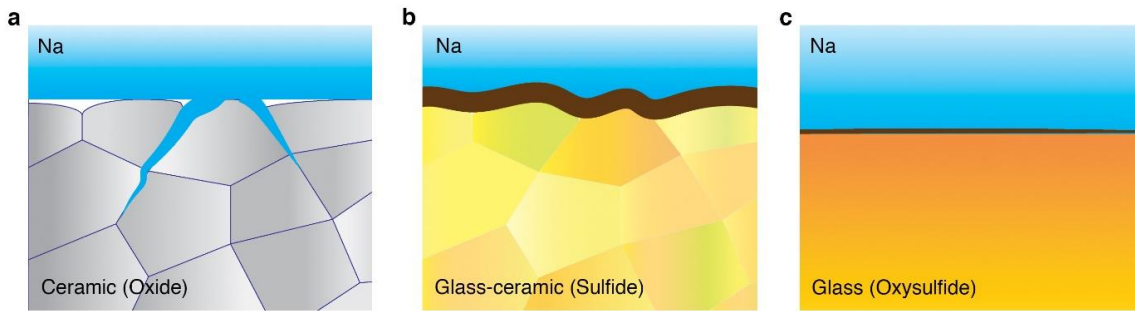


Figure 4.1 Na|SEs interface phenomena in different SEs. (a) Oxide-based electrolyte. (b) Sulfide-based electrolyte. (c) Newly designed oxysulfide glass.

To date, therefore, there is no single SE that can simultaneously meet all of the chemical, mechanical, electrochemical, and processing requirements to realize the SSMB with enhanced electrochemical performance and specific energy. Inspired by the specific benefits of the individual SEs described above, we have developed a new series of oxysulfide-based SEs ($\text{Na}_2\text{S}-\text{P}_2\text{S}_5-\text{P}_2\text{O}_5$) existing as a flawless glass using a facile one-step mechanochemical milling method. The ternary electrolyte system reported here has

been carefully designed based upon the following three aspects: first, P_2S_5 with a low melting point is a strong glass former that appears to facilitate the formation of a structurally defect-free bulk glass,^{163, 164} which we find crucial to addressing the Na dendrites propagation issue in above pure oxide-based SEs; second, following our previous studies on mixed oxysulfide glass,^{165, 166} P_2O_5 can form more robust glass network because of stronger chemical bonding of P–O than that of P–S, thereby boosting the mechanical strength and improving the electro-/chemical stability of pure sulfide-based SEs; third, Na_2S is an outstanding glass modifier to achieve high Na-ion conductivity.^{167, 168} During normal uniaxial cold-pressing, these new oxysulfide-based SEs were found to spontaneously transform into fully dense and microscopically homogeneous glass (Figure 4.1c). This structural transformation appears to be unique and essential to creating excellent mechanics, chemical stability, and electrochemical cycling vs. Na metal, which the oxide or sulfide-based SEs alone does not possess. Further, the new oxysulfide-based SEs enable to fabricate an ambient-temperature all-solid-state Na-S battery with the state-of-the-art energy density.

4.2 Experimental Procedures

4.2.1 Synthesis of Oxysulfide Solid-State Electrolytes

Na_2S , P_2S_5 , and P_2O_5 (Sigma–Aldrich, 99%) were used as the raw materials without further purification. The $Na_3PS_{4-x}O_x$ ($x = 0.00, 0.25, 0.50$ and 1.00) SEs were prepared by high-energy ball-milling technique. Typically, 2 g mixtures of appropriate amounts of Na_2S , P_2S_5 , and P_2O_5 powders were milled in an Argon-protected stainless steel jar containing stainless steel milling balls at 500 rpm for 3 h to obtain the amorphous SEs. The pure sulfide ($x = 0.00$) SE was synthesized by ball-milling raw

materials in the agate jar at 500 rpm for 20 h. The Na₃PS₄ glass-ceramic SE, *HT*-Na₃PS₄, was obtained from the glassy Na₃PS₄ by heating under vacuum at 260 °C for 2 h.

4.2.2 Materials Characterization of Oxysulfide Solid-State Electrolytes

Since Na₃PS_{4-x}O_x SEs are sensitive to air and moisture, all of the characterizations were conducted under Argon protection. Lab-based X-ray diffraction (XRD) were collected using a Rigaku MiniFlex 600 with Cu K α radiation ($\lambda = 1.5418 \text{ \AA}$). The synchrotron-based XRD patterns were collected at Beamline 11-ID-C at Advanced Photon Source with an X-ray wavelength of 0.1173 \AA . The thermal behavior of the SEs powders was examined using differential scanning calorimetry, DSC (TA Instruments Q2000), using nitrogen as the carrier gas. The sample was placed in the Tzero aluminum pan and hermetically crimp-sealed inside the Argon-filled glove box. The DSC measurements were carried out at a heating rate of 20 °C min⁻¹ from 50 °C to 400 °C. A Renishaw inVia Raman spectrometer employing a 488 nm Ar⁺ laser and 10 mW of power was used to collect the Raman spectra from 200 to 700 cm⁻¹. SE powders were placed into a small plastic sample holder inside an Argon-filled glove box. Infrared (IR) spectra were acquired on a Bruker IFS 66 v/s vacuum IR spectrometer in the range of 400–1200 cm⁻¹ using a KBr beamsplitter. The IR spectra of the samples were taken by diluting the finely ground glass and glass-ceramic powders to ~2% in finely ground and carefully dried CsI and then pressed into small pellets. ³¹P Solid-state Magic Angle Spinning Nuclear Magnetic Resonance (MAS NMR) spectra were collected using a JEOL ECA-500 NMR spectrometer. SE powders were packed into an alumina spinner with a sealant in an Argon-filled glove box. Spectra were collected using a 4.25 μs , 60° pulse length, and a 200 s recycle delay with the spinning speed of 20 kHz. Chemical shifts were

externally referenced to NaH_2PO_4 . Morphologies of the SEs powders, as well as the surface and cross-section of the densified pellets, were observed using a Gemini LEO 1525 scanning electron microscope (SEM). The X-ray photoelectron spectroscopy (XPS) spectra were collected using a Physical Electronics PHI 5700 on the SEs pellets before and after contacting with Na metal using a monochromatic Mg $K\alpha$ X-ray source. The XPS signals were corrected relative to the C 1s signal (284.8 eV) and fitted using the XPS PEAK41 software. The elastic modulus E and hardness H were measured using the same method as reported. Briefly, E and H values were measured using a G200 Keysight nanoindenter with a Berkovich indenter using the Oliver-Pharr method on samples inside an Argon-filled glove box. Indentations with a maximum indentation load of 1 mN were pressed on different spots of the SE surfaces to ensure the convergence of the measured results. The loading-displacement curves were recorded during the tests.

4.2.3 Fabrication of Symmetric Cell and Full Cell

For the fabrication of $\text{Na}|\text{Na}_3\text{PS}_3\text{O}|\text{Na}_3\text{PS}_{3.75}\text{O}_{0.25}$ or $HT\text{-Na}_3\text{PS}_4|\text{Na}_3\text{PS}_3\text{O}|\text{Na}$ symmetric cells, $\text{Na}_3\text{PS}_{3.75}\text{O}_{0.25}$ glass or $HT\text{-Na}_3\text{PS}_4$ glass-ceramic (~150 mg) SE powders were cold-pressed at 75 MPa; then $\text{Na}_3\text{PS}_3\text{O}$ glass powders (~25 mg) were evenly distributed on both sides of as-pressed $\text{Na}_3\text{PS}_{3.75}\text{O}_{0.25}$ glass or $HT\text{-Na}_3\text{PS}_4$ glass-ceramic pellet; finally the three layers were co-pressed at 450 MPa and attached with Na metal with an initial pressure of 20 psi. Similarly, the all-solid-state Na metal-sulfur full cells were assembled using $\text{Na}_3\text{PS}_{3.75}\text{O}_{0.25}|\text{Na}_3\text{PS}_3\text{O}$ bi-layer electrolyte, sulfur/Ketjen black/ $\text{Na}_3\text{PS}_{3.75}\text{O}_{0.25}$ composite, and Na metal as the separator, cathode, and anode, respectively. Specifically, since $\text{Na}_3\text{PS}_{3.75}\text{O}_{0.25}$ is the most conductive among the oxysulfide-based SEs and Ketjen black carbon has a high surface area of $1400 \text{ m}^2 \text{ g}^{-1}$,

they were chosen to blend with sulfur to create both fast ionic and electronic pathways for the sulfur active material in the composite cathode. So the architecture of the all-solid-state Na-S batteries was sulfur/Ketjen black/ $\text{Na}_3\text{PS}_{3.75}\text{O}_{0.25}$ | $\text{Na}_3\text{PS}_{3.75}\text{O}_{0.25}$ | $\text{Na}_3\text{PS}_3\text{O}$ | Na. In detail, sulfur (99.5%, Alfa Aesar) and Ketjen black (EC-600JD, AkzoNobel) powders with a weight ratio of 1:1 were ball-milled in an agate jar at a rotation speed of 500 rpm for 20 h to obtain a sulfur/Ketjen black nanocomposite, which was then milled with $\text{Na}_3\text{PS}_{3.75}\text{O}_{0.25}$ electrolyte powders at a rotation speed of 350 rpm for 30 min. The weight ratio of sulfur: Ketjen black: $\text{Na}_3\text{PS}_{3.75}\text{O}_{0.25}$ composite cathode is 2:2:6. $\text{Na}_3\text{PS}_{3.75}\text{O}_{0.25}$ electrolyte powders (~150 mg) were firstly pressed at 75 MPa into a pellet, of which anode side was then uniformly covered with $\text{Na}_3\text{PS}_3\text{O}$ electrolyte powders (20~25 mg) and cathode side with composite cathode powders (~1 mg). Bulk-type all-solid-state Na-S batteries were fabricated after co-pressing at 450 MPa and attaching a piece of Na metal foil onto the $\text{Na}_3\text{PS}_3\text{O}$ electrolyte side. Galvanostatic tests were performed in the potential range of 1.0 to 3.0 V vs. Na/Na⁺ at different current densities from 0.05 to 0.35 mA cm⁻². All the electrochemical tests were conducted at 60 °C except as otherwise specified.

4.2.4 Electrochemical Measurements

The temperature-dependent ionic conductivities of the pelletized SEs were measured from 25 °C to 90 °C using alternating current impedance method (frequency: 1 MHz–0.1 Hz, amplitude: 5 mV) on a VMP3, Bio-Logic Co. electrochemical workstation. The SEs pellets were prepared by cold-pressing in a polyetherether-ketone (PEEK) test cell die ($\varphi = 13$ mm) under a pressure of 450 MPa and then co-pressing with nano-copper (20 mg) powders (Sigma-Aldrich, 40–60 nm, $\geq 99.5\%$) as the electrodes under a pressure

of 200 MPa. Chemical stability of the SEs towards Na metal was studied by monitoring the impedance change vs. time of the symmetric cell Na|SE|Na, which was assembled by attaching two same pieces of Na metal foils (~100 μm in thickness) on both sides of the SEs. Cyclic voltammetry of the stainless steel foil|Na₃PS₃O|Na₃PS_{3.75}O_{0.25}|Na₃PS₃O|Na asymmetric cell was carried out using a scanning rate of 0.05 mV/s in a potential range of -0.3 V to +3.0 V. Na plating/stripping test of the Na|Na₃PS₃O|Na₃PS_{3.75}O_{0.25} or HT-Na₃PS₄|Na₃PS₃O|Na symmetric cells was conducted under step-current and constant-current modes.

4.3 Structural Characterizations of Oxysulfide Solid-State Electrolytes

To study the synergistic effects of oxygen and sulfur on the properties of the SEs, different compositions of $x = 0.00, 0.25, 0.50, 1.00$ were systematically characterized. The XRD patterns (Figure 4.2) show that all the raw materials became amorphous after milling, as no diffraction peaks of the starting materials were detected.

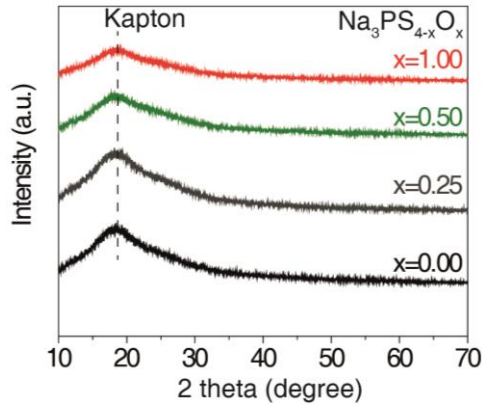


Figure 4.2 Lab-based X-ray diffraction (XRD) patterns of Na₃PS_{4-x}O_x ($x=0.00, 0.25, 0.50,$ and 1.00) SEs.

The amorphous glass is formed by the local high-temperature generated during the milling process and rapid thermal quenching after the milling.¹⁶⁹ However, just as in

melt-quenching method, the quenching rate in milling process is always insufficient to yield a fully amorphous glass and small amounts of crystalline phases can be detected in some systems (e.g. $\text{Na}_2\text{S}-\text{P}_2\text{S}_5$ ¹²⁶ and $\text{Li}_2\text{S}-\text{P}_2\text{S}_5$ ¹⁷⁰). To investigate the possible crystalline phases in the $\text{Na}_3\text{PS}_{4-x}\text{O}_x$ SEs, high-energy synchrotron XRD patterns were collected and shown in Figure 4.3a.

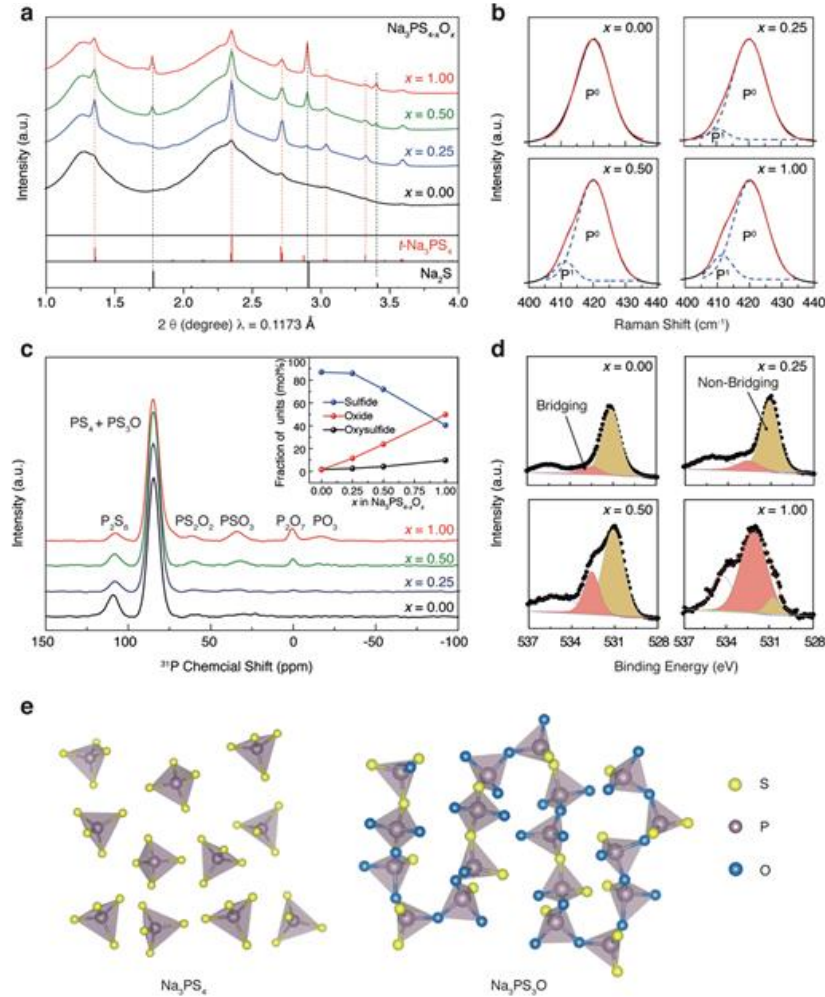


Figure 4.3 (a) Synchrotron X-ray diffractions. (b) Gaussian fitting of Raman peak (PS_4 mode) at 420 cm^{-1} . (c) ^{31}P -NMR spectra. (d) X-ray photoelectron spectra (XPS). (e) Schematics of the network structure of the Na_3PS_4 and $\text{Na}_3\text{PS}_3\text{O}$.

All synthesized SEs feature two broad halos superimposed with weak Bragg peaks, indicating a small number of fine-grained crystalline phases (tetragonal Na_3PS_4

and Na₂S) do form and are embedded in the dominant glassy matrix. When x approaches 1.00, the proportion of the crystalline Na₃PS₄ diminishes, while the Na₂S increases in intensity. The reason for the appearance Na₂S is disproportionation reaction ($2\text{Na}_3\text{PS}_4 (\text{P}^0) \rightarrow \text{Na}_4\text{P}_2\text{S}_7 (\text{P}^1) + \text{Na}_2\text{S}$) as confirmed from the Gaussian fitting of the primary Raman peak (corresponding to the stretching mode of the PS₄ unit^{167, 171}) centered at 420 cm⁻¹ (Figure 4.3b). As indicated from both Figure 4.3a and 4.3b, the main composition of the Na₃PS_{4-x}O_x SEs is a glassy phase with a small number of crystalline Na₃PS₄ and Na₂S.

³¹P MAS-NMR was used to gain further insights into the glassy phase of these SEs by examining the local structure around the phosphorus glass forming cations. Deconvolution of the ³¹P NMR spectra (Figure 4.3c) show that the glass Na₃PS₄ ($x = 0.00$) is mainly composed of PS₄ and P₂S₆ sulfide units, which is consistent with the Raman spectra. With the incorporation of oxygen, three new peaks at 63 ppm, 32 ppm, and -17 ppm can be clearly observed, which are attributed to the formation of PS₂O₂, PSO₃, and PO₃ units.¹⁷² The peak for the expected but missing PS₃O oxysulfide units is nearly indiscernible since it has essentially the same chemical shift as the PS₄ units, whose relative amount could be calculated with the charge balance method we recently developed.^{171, 173} As is shown in the inset of Figure 4.3c, the fraction of mixed oxysulfide units PS_{4-x}O_x ($x = 1,2,3$) dramatically increases with oxygen incorporation and become dominant when x reaches 1.0. Their appearance further suggests that the oxygen has been incorporated into the PS₄ tetrahedra unit, which is expected to improve the chemical stability and mechanical strength of the glass network over that of the pure sulfide-based SE. FTIR spectroscopy was further applied to explore the chemical bonding of P-S and

P–O and the corresponding peaks assignments shown in Figure 4.4. The S or O bonding mainly exists as three modes: non-bridging sulfur (NBS) P–S⁻ (400–600 cm⁻¹), bridging oxygen (BO) P–O–P (600–950 cm⁻¹), and non-bridging oxygen (NBO) P–O⁻ or P=O (950–1200 cm⁻¹).^{174, 175} The oxygen incorporation leads to a slightly increased fraction of P–O⁻ and P=O bonds and a particularly significant increase in the fraction of BO P–O–P bonds, where the O atom is bridged between two P atoms.

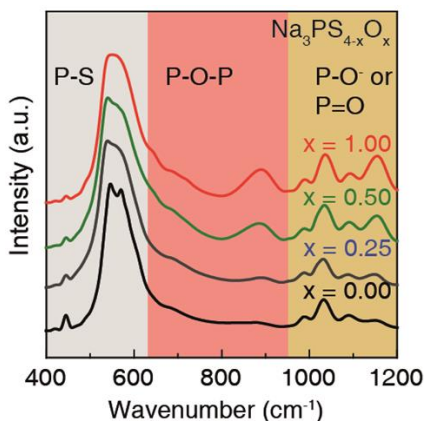


Figure 4.4 FT-IR spectra of Na₃PS_{4-x}O_x ($x=0.00, 0.25, 0.50, \text{ and } 1.00$) SEs.

Further evidence of the formation of BO can be found in the O 1s XPS spectra (Figure 4.3d), where peak for BO (532.5 eV^{176, 177}) becomes dominant as x reaches 1.00. Spectral deconvolution of the Na₃PS₃O composition, for example, shows that more than 90% of the added oxygen atoms are present as BOs in the glass. This result is completely consistent with our previous work on a similar Li₂GeS_{4-x}O_x glass system.¹⁷⁸ As shown in Figure 4.3e, compared with the fully ionic and non-bridging structure of Na₃PS₄ sulfide, the formation of BO units in the Na₃PS₃O oxysulfide eventually leads to a more interconnected glass structure that possesses high structure density, higher mechanical modulus, and stronger bonding that improves the chemical stability of SEs.

4.4 Mechanical and Morphological Properties of Oxysulfide Solid-State Electrolytes

The morphological structure and mechanical properties of $\text{Na}_3\text{PS}_{4-x}\text{O}_x$ SEs were then investigated. Obvious pores and grain boundaries can be clearly observed in both the surface and cross-sectional SEM images of pelletized $HT\text{-Na}_3\text{PS}_4$ (Figure 4.5). These Griffith flaws are believed to induce dendrite penetration⁶⁰ and eventually lead to short-circuiting, as demonstrated in Figure 4.6.

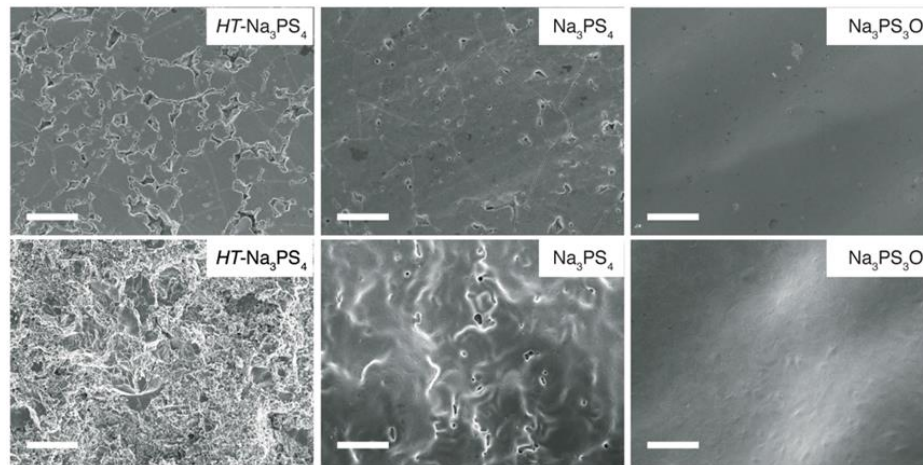


Figure 4.5 Top view (first row) and cross-sectional (second row) SEM images of $HT\text{-Na}_3\text{PS}_4$ glass ceramic, Na_3PS_4 glass, and $\text{Na}_3\text{PS}_3\text{O}$ glass. Scale bar: 10 μm .

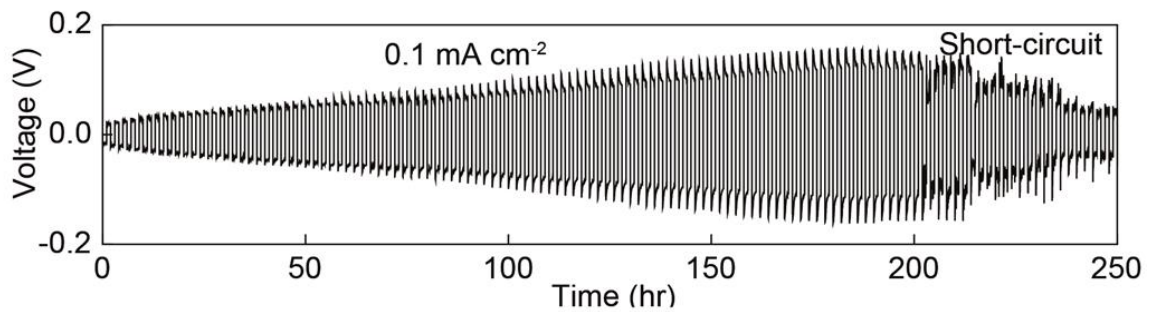


Figure 4.6 Galvanostatic cycling of $\text{Na}|HT\text{-Na}_3\text{PS}_4|\text{Na}$ symmetric cells at 60 $^\circ\text{C}$ under current density of 0.1 mA cm^{-2} with a stripping/plating capacity of 0.1 mAh cm^{-2}

Na_3PS_4 glass SE ($x = 0.00$) shows fewer defects on the surface and forms a denser pellet compared to $HT\text{-Na}_3\text{PS}_4$. Surprisingly, the oxygen doped $\text{Na}_3\text{PS}_3\text{O}$ glass SE ($x = 1.00$) appears to be absent of any pores and cracks and is smooth and uniform from the surface through to the interior. To the best of our knowledge, this fully dense morphology observed here is the first result reported in any SE fabricated by the simple cold-pressing at room temperature.

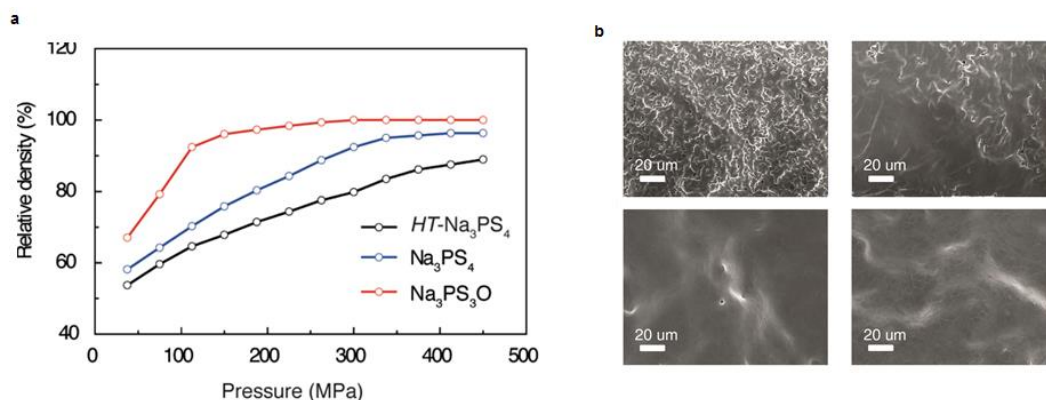


Figure 4.7 (a) Relative density vs. molding pressure plot. (b) SEM images of cross-sectional Na_3PS_4 (first row) and $\text{Na}_3\text{PS}_3\text{O}$ (second row) SE pellets pressed at 150 MPa and 375 MPa.

As shown in Figure 4.7a and 4.7b, the $\text{Na}_3\text{PS}_3\text{O}$ glass is nearly fully densified at a relatively low pressure of 150 MPa. In comparison, the Na_3PS_4 glass and $HT\text{-Na}_3\text{PS}_4$ are not readily achievable even though much higher pressure of 450 MPa during cold-pressing was applied. The excellent formability of these oxysulfide-based SEs may be attributed to the synergistic effects of mixed P_2S_5 and P_2O_5 glass formers and abundant BOs units. We hypothesize that such electrolyte that lacks grain boundaries, pores, and surface flaws combining with high mechanical strength can prevent the Na dendrite growth. To quantify the mechanical properties of SEs, the Young's elastic modulus E and hardness H were measured using our previously reported nano-indentation technique.¹¹⁷

Typical loading-displacement curves (Figure 4.8a) of the $HT\text{-Na}_3\text{PS}_4$ pellet exhibit a sudden increase of indenter penetration during the loading process, which is not found in glassy $\text{Na}_3\text{PS}_{4-x}\text{O}_x$ pellets. A “pop-in” phenomenon is observed associated with crack generation.¹¹⁷ Further, benefiting from the homogeneous structure, the $\text{Na}_3\text{PS}_{4-x}\text{O}_x$ SEs display very small standard deviations for E and H as seen in the bar chart (Figure 4.8b). The oxygen doping results in an increase of E and H of SEs, which supports the above hypothesis. The E and H of $\text{Na}_3\text{PS}_3\text{O}$ glass were measured to be 20.9 ± 0.7 GPa and 1.0 ± 0.1 GPa, respectively, which are the highest among $\text{Na}_3\text{PS}_{4-x}\text{O}_x$ SEs. In particular, they are superior to the reported sulfide-based Na-ion SEs by the complex hot-pressing method.^{164, 179}

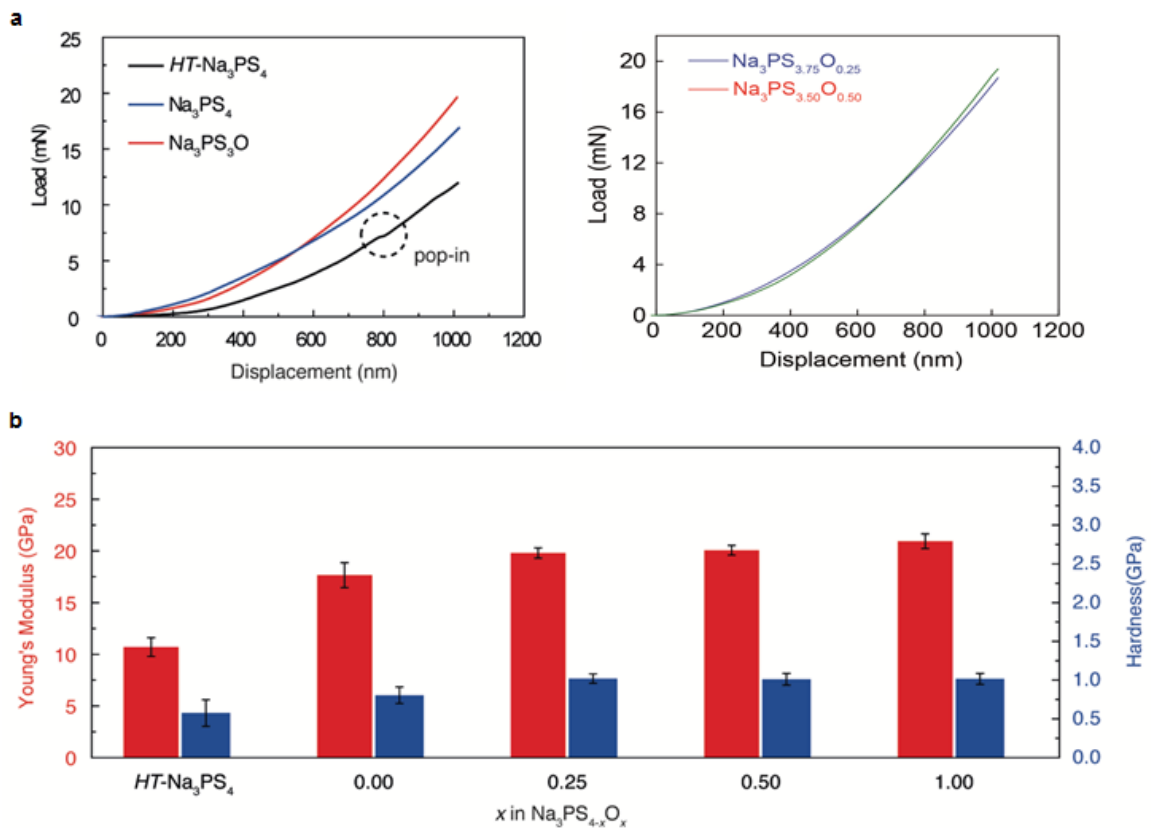


Figure 4.8 (a) Nano-indentation loading curves. (b) Comparison of Young's modulus and hardness for $HT\text{-Na}_3\text{PS}_4$ glass ceramic and oxysulfide glass SEs.

4.5 Chemical Stabilities of Oxysulfide Solid-State Electrolyte against Na Metal

As described above, the chemical and electrochemical stability of SEs against Na metal anode is critically important for developing high-performance SSMBs. We tested the Na|Na₃PS_{4-x}O_x SE interfacial stability by monitoring the EIS change of Na|Na₃PS_{4-x}O_x|Na symmetric cells before and after 5 hours of rest at 60 °C, as shown in Figure 4.9a.

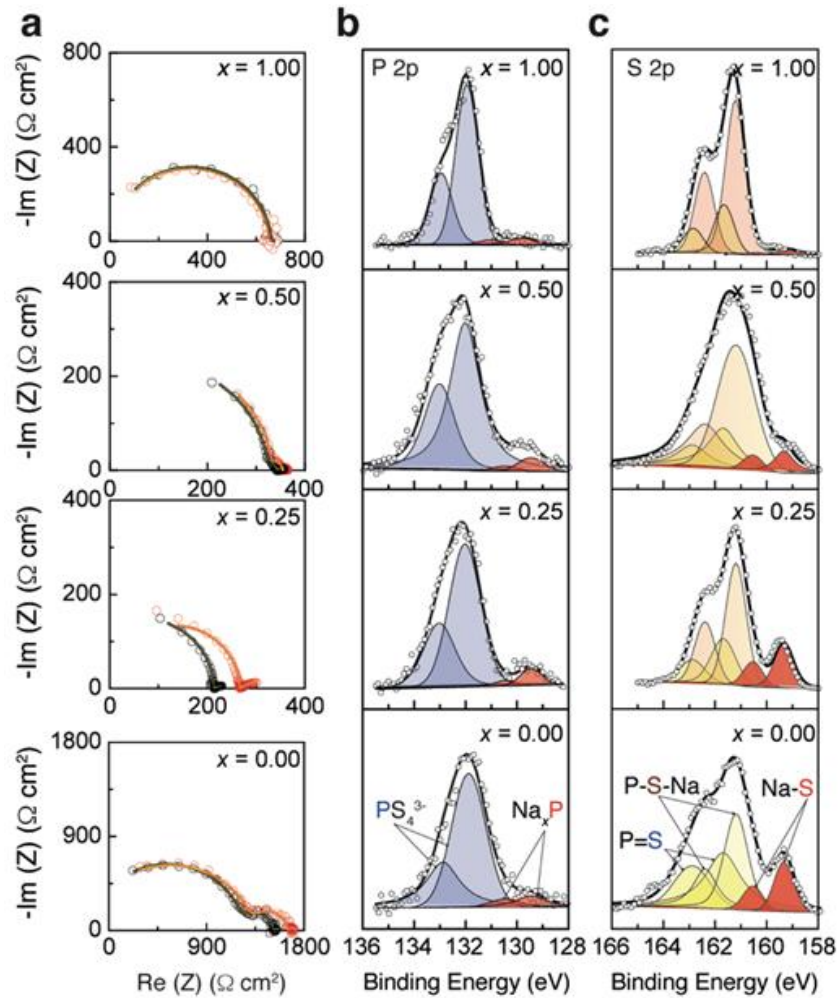
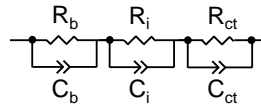


Figure 4.9 (a) Electrochemical impedance spectra (EIS) evolution of freshly made and 5 h-standing Na|SE|Na symmetric cells. (b) P 2p and (c) S 2p XPS spectra of the interfaces between Na and SEs after 5 h of contact.

From the fitting parameters shown in Table 4.1, it can be concluded that the added oxygen has a positive effect on improving the SEs' chemical stability against Na metal as the total areal specific resistance (ASR) change becomes less significant. Further from the fitting parameters shown in Table 4.1, indeed, it is noteworthy that the Na₃PS₃O SE not only presents a negligible change of bulk resistance and charge-transfer resistance, but also shows an indistinguishable interfacial resistance, suggesting not only a chemically stable interface but also a mechanically intimate contact between Na₃PS₃O and Na. In contrast, all the other SEs display an interfacial resistance increasing with time, which is indicative of an unstable Na|SE interface.

Table 4.1 Fitting results of EIS spectra (Figure 4.9a) of Na|Na₃PS_{4-x}O_x (x=0.00, 0.25, 0.50, and 1.00) SEs|Na symmetric cells before and after resting for 5 h



<i>x</i> value	ASR [Ω·cm ²]	<i>R</i> _b [Ω·cm ²]	<i>R</i> _i [Ω·cm ²]	<i>R</i> _{ct} [Ω·cm ²]
0.00 before	1596.7	1240	272	84.7
0.00 after	1753.0	1350	304	99.0
0.25 before	253.1	216	6.0	31.1
0.25 after	341.7	254	16.5	71.2
0.50 before	367.17	334	24.2	8.97
0.50 after	376.7	332	28.3	16.4
1.00 before	664.9	644	-	20.9
1.00 after	662.2	640.8	-	21.4

To identify the interphase composition, Na metal was detached from the symmetric cells and the surface of SEs was probed by the XPS. Compared to the fresh

SEs, the glassy SEs after contacting with Na metal ($x < 1.00$) exhibit a new pair of doublets in both P 2p spectra and S 2p spectra (Figure 4.9b and 4.9c). These new pairs of doublets correspond to the reduced phosphide (Na_xP) and sulfide species (Na_2S),^{122, 147} respectively, which may form a mixed-conducting interface that can cause continuous reduction of the SE. Similar phenomena have been observed in other pure sulfides and selenides, e.g. Na_3PS_4 ,¹⁴⁷ Na_3SbS_4 ^{160, 161} and Na_3PSe_4 ¹²². In contrast, the XPS signals from these reduced species are nearly indiscernible for $\text{Na}_3\text{PS}_3\text{O}$, validating the negligible ASR increase from EIS measurement. We assert that the outstanding chemical stability of $\text{Na}_3\text{PS}_3\text{O}$ in contact with Na metal is contributed by: first, as described above, $\text{Na}_3\text{PS}_3\text{O}$ has a more interconnected and robust glass network than the other SEs due to the existence of more BO units, which have higher electronic binding energy than pure sulfide units; second, the terminal oxygen in $\text{P}-\text{O}^-$ may react with Na metal and form an electronically insulating and stable interphase (Na_xO).^{180, 181}

4.6 Electrochemical Performance of Oxysulfide-Based Symmetrical Cell and Full Cell

Figure 4.10a shows the temperature-dependence of the Na-ion conductivities that were obtained from the Nyquist plots (Figure 4.10b) for the $\text{Na}_3\text{PS}_{4-x}\text{O}_x$, $x = 0.00, 0.25, 0.50, 1.00$, SEs. From Figure 4.10b and 4.10c, it is intriguing that with the initial addition of oxygen, the conductivity of the $\text{Na}_3\text{PS}_{3.75}\text{O}_{0.25}$ SE exhibit a 6-fold increase to $2.7 \times 10^{-4} \text{ S cm}^{-1}$ with an activation energy as low as 41.5 kJ mol^{-1} . This anomalous increase in the ionic conductivity may be associated with two factors: one is an increase of the ‘doorway’ radius as observed in our previously studied $\text{Li}_2\text{GeS}_{2-x}\text{O}_x$ glassy SE,¹⁸² the

other is the existence of highly conductive tetragonal Na_3PS_4 crystalline phase (Figure 4.3a). However, further additions of oxygen monotonically decrease the SEs' conductivities, which may be attributed to the more compact glass network that reduces the free volume available for Na-ion transport.

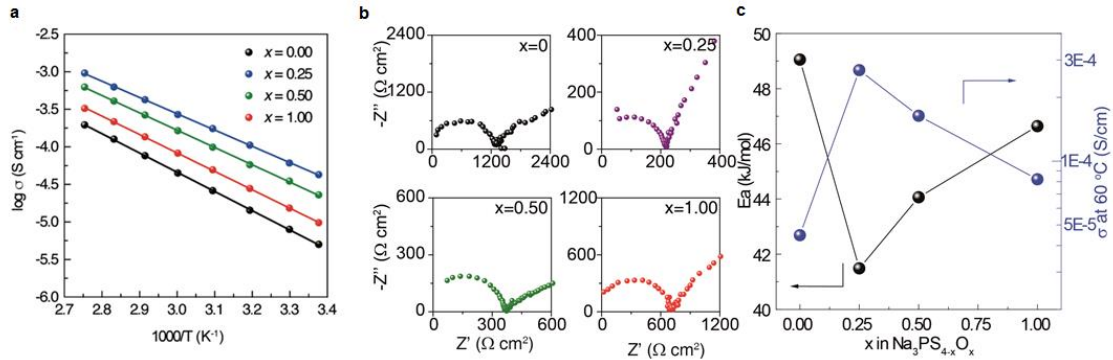


Figure 4.10 (a) Temperature dependence of the Na-ion conductivities of SEs. (b) Nyquist plot of oxysulfide SEs. (c) Activation energies and conductivities versus oxygen contents.

By taking full advantage of the high chemical stability of $\text{Na}_3\text{PS}_3\text{O}$ and the high Na-ion conductivity of $\text{Na}_3\text{PS}_{3.75}\text{O}_{0.25}$, a tri-layer architecture for the glassy electrolyte separator was specially designed (inset of Figure 4.11). Further from the SEM image, both layers exhibit intimate interface contact. Cyclic voltammetry was used on an asymmetric cell Na|tri-layer SE|SS, where SS is stainless steel, to examine the Na metal plating/stripping capability and the stability of the tri-layer SE against oxidation and reduction. As shown in Figure 4.11, a pair of well-defined Na oxidation and reduction peaks is observed at ~ 0 V versus Na^+/Na and there are no remarkable oxidation currents up to 3 V. These results indicate the applicability of the tri-layer SE in SSMBs and in particular, the applicability of operating in a Na-S battery.

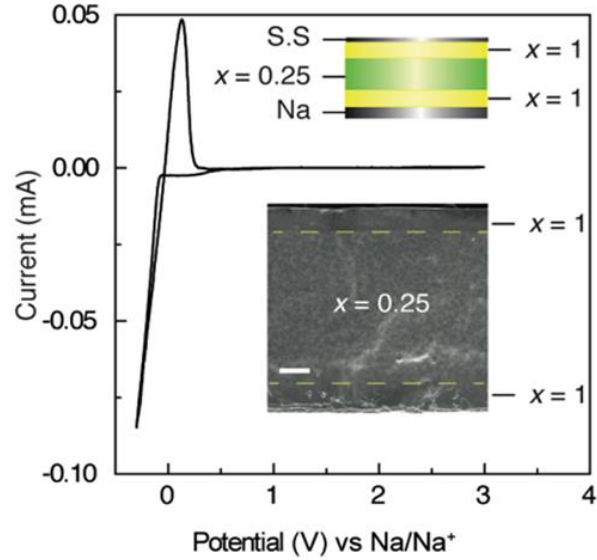


Figure 4.11 Cyclic voltammetry curve of tri-layer electrolyte in Na|SE|Stainless Steel asymmetric cell. Insets show the schematic of the cell set-up and SEM image of the tri-layer electrolyte. Scale bar is 100 μm .

Before fabricating a full cell, the cyclability of the tri-layer SE was studied in a symmetric Na|trilayer-SE|Na cell using step-current and constant-current tests, as shown in Figure 4c,d, respectively. From the Figure 4.12, the critical current density (CCD) that reflects the capability of the SE in resisting metallic dendrite was found to be 2.3 mA cm^{-2} , which is unexpectedly comparable to the state-of-the-art CCD results based on oxide-based SEs, see Table 4.2. The remarkably high CCD value of the oxysulfide glassy SEs is attributed to the homogeneous and nearly flawless microstructure. These observations agree well with recently proposed Griffith's failure mechanism⁶⁰ of SEs towards a metal anode.

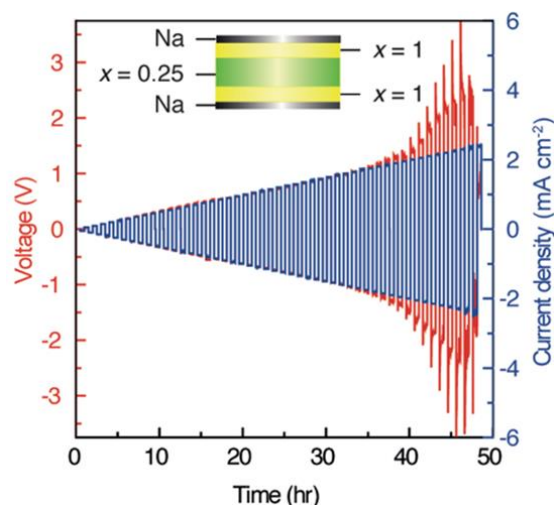


Figure 4.12 Critical current density test of $\text{Na}_3\text{PS}_3\text{O}|\text{Na}_3\text{PS}_{3.75}\text{O}_{0.25}|\text{Na}_3\text{PS}_3\text{O}$ tri-layer SE working in $\text{Na}|\text{SE}|\text{Na}$ symmetric cells at $60\text{ }^\circ\text{C}$, step size of the current density increase is 0.05 mA cm^{-2} and plating/stripping time is 0.5 h.

Table 4.2 Comparison of reported critical current densities (CCD) of SEs with that of $\text{Na}_3\text{PS}_3\text{O}$ SE developed our work

Electrolyte	Electrolyte status	Test temperature [$^\circ\text{C}$]	Critical current density [mA cm^{-2}]	Ref.
$\text{Li}_7\text{La}_3\text{Zr}_2\text{O}_{12}:\text{Ta}$	Ceramic	50	0.8	183
$\text{Li}_7\text{La}_3\text{Zr}_2\text{O}_{12}:\text{Al}$	Ceramic	RT	0.134	184
$\text{Li}_7\text{La}_3\text{Zr}_2\text{O}_{12}:\text{Al}$	Ceramic	RT	0.3	39
$75\text{Li}_2\text{S}-25\text{P}_2\text{S}_5$	Glass	RT	0.5	185
$75\text{Li}_2\text{S}-25\text{P}_2\text{S}_5$	Glass	RT	1.0	185
$75\text{Li}_2\text{S}-25\text{P}_2\text{S}_5$	Glass-ceramic	RT	0.1	185
$70(75\text{Li}_2\text{S}-25\text{P}_2\text{S}_5)-30\text{LiI}$	Glass	RT	1.0	186
$70(75\text{Li}_2\text{S}-25\text{P}_2\text{S}_5)-30\text{LiI}$	Glass	60	2.16	186
$\text{Na}_3\text{PS}_3\text{O}$	Glass	60	2.3	This work

In the constant-current mode, Figure 4.13a,b show that symmetric cells with the

same tri-layer SE can stably cycle for several hundred hours without short-circuiting at current densities of 0.2 mA cm^{-2} and 0.5 mA cm^{-2} , respectively. Furthermore, different from the pure sulfide-based SEs (Figure 4.6), the voltage profiles of the oxysulfide-based SE (inserts of Figure 4.13a,b) are flat with negligible polarization increase at each cycle, indicating the fast and stable Na plating/stripping processes at the Na|Na₃PS₃O interface. It is clear that the oxysulfide-based SE developed in this work significantly extends the cycle life and current density for SEs in symmetric cells, setting new standards in SSMBs.

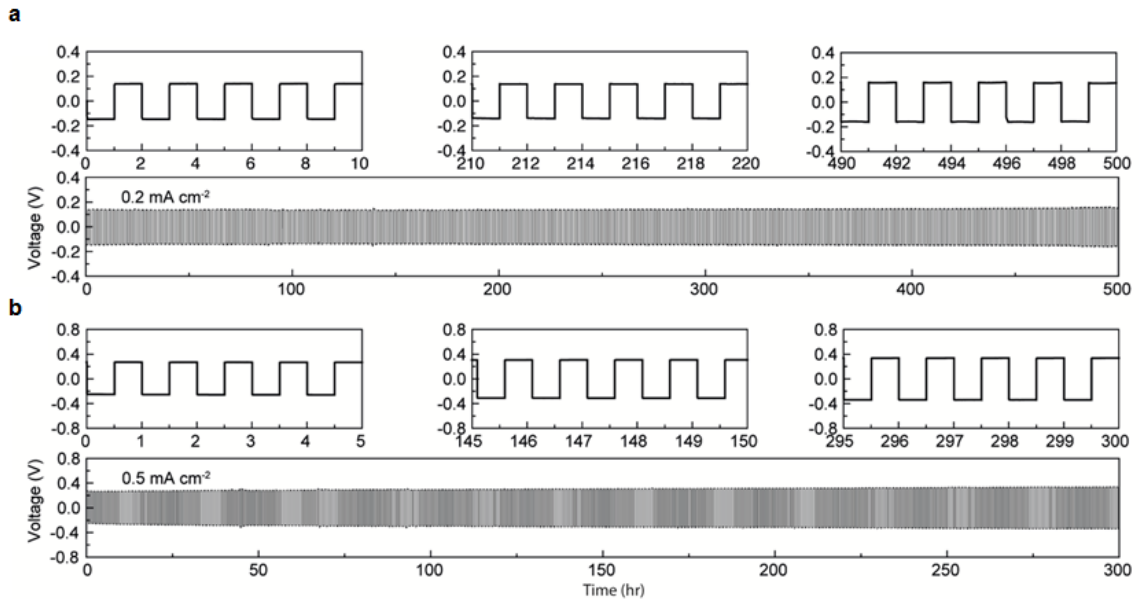


Figure 4.13 Galvanostatic cycling of Na|Na₃PS₃O|Na₃PS_{3.75}O_{0.25}|Na₃PS₃O|Na symmetric cells at 60 °C under current densities of (a) 0.2 mA cm^{-2} and (b) 0.5 mA cm^{-2} , respectively.

The excellent Na|Na₃PS₃O interfacial stability enables the fabrication of SSMBs, of which the one of the most promising is the low-temperature Na-S battery with very low cost and high specific energy. On the basis of the above study that demonstrated the stability of tri-layer SEs, a Na-S battery with the architecture of S–

$\text{Na}_3\text{PS}_{3.75}\text{O}_{0.25}|\text{Na}_3\text{PS}_{3.75}\text{O}_{0.25}|\text{Na}_3\text{PS}_3\text{O}|\text{Na}$ was designed and tested at a low temperature of 60 °C. Figure 4.14a shows that the cell can deliver a high initial discharge capacity of 1280 mAh g⁻¹, which is 76% of the theoretical capacity of sulfur (Na→Na₂S: 1675 mAh g⁻¹) and especially much higher than that, 558 mAh g⁻¹, of the conventional high-temperature Na-S battery.¹⁵⁴ The 1st cycle coulombic efficiency is 92%, indicating that the polysulfide shuttling phenomenon commonly found in a liquid electrolyte cell is inexistent in the current system. After 40 cycles, the battery delivers a capacity of ~1000 mAh g⁻¹ with capacity retention of >80%, see Figure 4.14b. These values are significantly better than those of the reported Na-S batteries using oxide or polymer SEs as shown in Table 4.3. The average discharging potential is 1.42 V, which is higher than those of other pure sulfide-based SE-based Na-S batteries that use a NaSn alloy as the anode (Table 4.3). Therefore, the oxysulfide-based Na metal-sulfur battery system described here is able to provide the highest specific energy density, 1819 Wh kg⁻¹, among all currently reported Na-S battery systems. Further, the cell presents good rate capability of 908 and 574 mAh g⁻¹ at high current densities of 0.20 and 0.35 mA cm⁻², respectively, and stable cycling up to 150 cycles (Figure 4.14c). The significantly improved performance of our Na-S battery is attributed to the excellent stability of Na₃PS₃O towards Na anode, which enables Na to stably plate/strip at high rates, as well as the superior formability of Na₃PS_{3.75}O_{0.25}, which ensures the consistently good contact with sulfur during cycling.

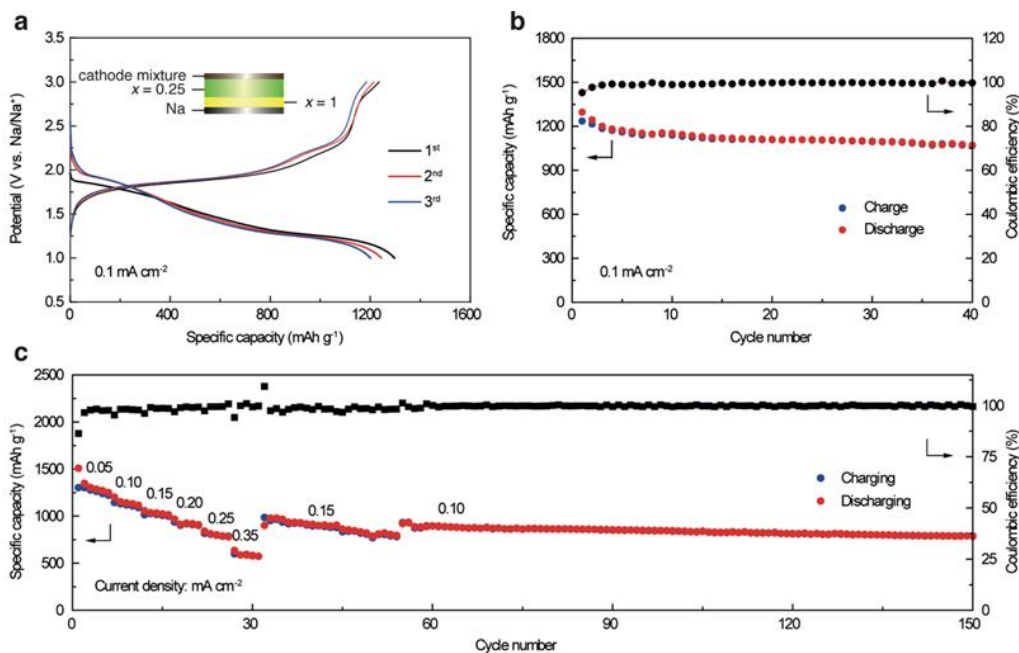


Figure 4.14 Na-S full cell performances at 60 °C. (a) Charge/discharge voltage profiles. (b) Capacity and coulombic efficiency vs. cycle number. (c) Rate capability and cycling stability under different current densities.

Table 4.3 Comparison of reported Na-S batteries using SEs with our work

Electrolyte separator	Discharge voltage [V]	1 st cycle capacity [mAh g ⁻¹]	Specific energy [Wh kg ⁻¹]	Cycles	Ref.
Na _{3.1} Zr _{1.95} Mg _{0.05} Si ₂ P O ₁₂	1.75	527	922	10	187
Poly (ethylene oxide) (PEO)	1.75	505	884	10	188
β"-Al ₂ O ₃	1.73	836	1446	100	189
Na ₃ PS ₄	1.10	1522	1674	2	190
Na ₃ PS ₄	1.30	1112	1446	25	191
Na ₃ PS ₄	1.25	1050	1312	50	152
Na ₃ PS ₄	1.25	>800	~1000	50	192
Na₃PS_{3.75}O_{0.25}/Na₃P S₃O	1.42	1281	1819	150	Our work

4.7 Conclusions

A new class of oxysulfide glass SEs with combined advantages of sulfide-based SEs and oxide-based SEs was successfully synthesized and systematically investigated in both symmetric and full cell configurations. Compared with pure sulfide-based SEs, the oxygen was introduced into the PS_4 structure units, leading to the formation of more oxide and oxysulfide units with BO characteristics. As a result, these oxysulfide-based SEs exhibit dramatically improved formability and are capable of forming homogenous and near flawless glass pellet with significantly higher mechanical strength via facile cold-pressing. Furthermore, the oxysulfide units with stronger P–O bond dramatically improve the chemical stability of the SEs towards Na metal. A near flawless tri-layer composite SE with $\text{Na}_3\text{PS}_3\text{O}|\text{Na}_3\text{PS}_{3.75}\text{O}_{0.25}|\text{Na}_3\text{PS}_3\text{O}$ can not only demonstrate a record-high CCD of up to 2.3 mA cm^{-2} and a long-cycle-life Na metal symmetric cell up to 500 h under 0.2 mA cm^{-2} , but also enables a Na metal-sulfur cell to deliver the highest energy density among all known solid-state Na-S systems to date. These new oxysulfide-based SEs and the tri-layer SEs may provide a very promising avenue of research towards the development of high energy, safe, low-cost, and long-cycle-life SSMBs in general and new solid-state Na-S batteries for energy storage devices.

Chapter 5 A High-Energy Quinone-Based Solid-State

Sodium Battery Using Oxide Electrolyte

5.1 Introduction

The sulfide-based solid electrolytes,^{119, 193} for example, the Na₃PS₄ and Na₃SbS₄, which are usually anodically and cathodically unstable, are prone to form resistive interfacial layers when high-voltage cathodes or Na metal anode are applied.^{122, 127, 147, 162} We recently demonstrated that adopting a tailored organic cathode Na₄C₆O₆ with redox potential fully lying within the stability window of Na₃PS₄ (1.5–2.7 V vs. Na⁺/Na) or incorporating a polymer electrolyte that is stable with Na metal in between Na and Na₃SbS₄ are effective to address the interfacial challenges of Na₃PS₄ and Na₃SbS₄, respectively.^{100, 161} In contrast, oxide-based solid electrolytes, *e.g.* Na beta-alumina solid electrolyte (BASE), are electrochemically stable in the window of 0–3.5 V vs. Na⁺/Na,^{154, 194} which enables more favorable cathode-electrolyte and Na anode-electrolyte interfaces. However, the rigid surface of BASE poses a challenge in forming intimate contact with cathode materials and sodium metal,¹⁹⁵⁻¹⁹⁷ resulting in large interfacial resistance and poor cycle life. Therefore, interface engineering of electrode-electrolyte contact is critical for developing high-performance oxide-based all-solid-state sodium metal batteries (ASSMBs).

In this work, we present a first proof-of-concept demonstration of an oxide-based ASSMB with a sodium metal anode and an organic quinone cathode, pyrene-4,5,9,10-tetraone (PTO), by simultaneously engineering the Na anode-BASE interface with a Sn nanofilm and the cathode interparticle and cathode-BASE contact with a mechanically

compliant ionically conductive poly(ethylene oxide) (PEO) auxiliary agent. The Sn-modified BASE shows the best cycling stability towards Na metal and the PEO-ameliorated PTO presents the highest energy density at the active-material level achieved thus far among reported ASSMBs (Table 5.1). This study reveals a universal strategy to reduce interfacial barriers in solid-state batteries.

Table 5.1 Cell performance of reported all-solid-state sodium metal batteries.

Solid-state Electrolyte	Anode interfacial layer	Cathode	Cathode interfacial layer	Specific energy (Wh kg⁻¹)	Ref.
Na ₃ Zr ₂ Si ₂ PO ₁₂	CPMEA	NaTi ₂ (PO ₄) ₃	CPMEA	214	195
Na ₂ (B ₁₂ H ₁₂) _{0.5} (B ₁₀ H ₁₀) _{0.5}	-	NaCrO ₂	-	287	198
Na _{3.3} Zr _{1.7} La _{0.3} Si ₂ P _{O₁₂}	-	Na ₃ V ₂ (PO ₄) ₃	-	360	196
Na _{2.9375} PS _{3.9375} Cl _{0.0625}	-	TiS ₂	-	371	160
Na ₃ Zr ₂ Si ₂ PO ₁₂	-	Na ₂ MnFe(CN) ₆	PEO	432	180
PEO	-	NaCu _{1/9} Ni _{2/9} Fe _{1/3} Mn _{1/3} O ₂	-	408	199
Na _{3.1} Zr _{1.95} Mg _{0.05} Si ₂ PO ₁₂	-	Sulfur	PEO	724	187
Na ₃ PS ₄	-	FeS ₂	-	830	200
BASE	Sn	PTO	PEO	891	This work

5.2 Experimental Procedures

5.2.1 Synthesis of Oxide-Based Solid-State Electrolyte

Dense pellets of BASE containing 9.0 wt% Na₂O and 0.72 wt% Li₂O were prepared by the solid-state sintering method following our previous work.¹⁵⁴ Typically, we prepared two precursors zeta-lithium aluminate (Li₂O-5Al₂O₃) and zeta-sodium aluminate (Na₂O-5Al₂O₃) by calcinating Li₂CO₃:Al₂O₃ (molar ratio 1:5) and

$\text{Na}_2\text{CO}_3:\text{Al}_2\text{O}_3$ (molar ratio 1:5) at 1250 °C for 2 h. Then the precursors were mixed at molar ratio of 1:5.5 (zeta-lithium aluminate: zeta-sodium aluminate) by ball-milling, spray-granulated, pressed into pellets at 200 MPa, and finally sintered at 1560 °C for 10 min and annealed at 1460 °C for 2 h to obtain dense BASE pellets in a muffle furnace (MTI Corp., KSL-1700X-S-UL). The heating ramp rate is 20 °C min⁻¹. To compensate the lithium and sodium loss of the BASE pellet during annealing, the green BASE pellets was covered with mother powders with the same composition. The as-sintered pellets were carefully polished with 1200-grit sand paper and ethanol in air. After polishing, the pellets were ultrasonicated in ethanol and then vacuum-dried at 60 °C. Then the pellets were quickly transferred to an argon-filled glove box for further study. The density of the BASE pellet is 3.2 g cm⁻³ and dimension is 12 mm in diameter and 1 mm in thickness.

5.2.2 Interfacial Modification Methods

At the anode-electrolyte interface, we deposited a 20-nm-thick Sn layer inside a thermal evaporator equipped with a thickness monitor (Inficon SQC-310) at a deposition rate of 1 Å/s. The thickness of Sn layer was confirmed by a Dektak XT profilometer. The molten Na metal at 150 °C can diffuse into the Sn layer to form NaSn alloy and wets the electrolyte surface, decreasing the contact angle between Na metal and electrolyte. At the cathode-electrolyte interface, we added 20 wt.% PEO- NaClO_4 which serve as a mechanically compliant and ionically conductive agent inside the composite cathode to improve the contact.

5.2.3 Material Characterizations

X-ray diffraction (XRD) patterns of BASE pellets were collected using a Rigaku MiniFlex 600 with Cu $K\alpha$ radiation ($\lambda = 1.5418$ Å). Surface and cross-sectional

morphology of the BASE electrolyte with and without Sn coating were characterized using a Gemini LEO field emission scanning electron microscope (SEM). The chemical elements of the interface between Na and BASE was identified using energy dispersive X-ray (EDX) spectroscopy.

5.2.4 Fabrication of Symmetric Cells and Full Cells

For symmetric cells, two Na metal foils (~300 μm each) were attached to both sides of Sn-coated BASE or bare BASE pellets, kept at 150 $^{\circ}\text{C}$ for 30 minutes to ensure better contact, and then fabricated in the pressured die cells at an initial pressure of 40 psi.

The organic cathode active material PTO was synthesized following the literature. The PTO-based composite cathode was prepared as follows. Briefly, 6 mg PTO, 4 mg Super P carbon, and 2 mg polyvinylidene fluoride (PVDF) powders were ground in an agate mortar. Then, 8 mg PEO- NaClO_4 (PEO Mw: 100,000; EO:Na molar ratio: 10:1) dissolved in anhydrous acetonitrile (10 wt.%) was added into the mixture, resulting in a homogenous cathode slurry. The slurry was then coated onto the uncoated side of the BASE and dried in a vacuum oven at 70 $^{\circ}\text{C}$ for 10 h until the acetonitrile was fully dried. The composite cathode has a mass ratio of PTO:PEO- NaClO_4 :C:PVDF of 3:4:2:1 with active material mass loading of $\sim 1.2 \text{ mg cm}^{-2}$. A stainless-steel foil was used as a current collector; the device area was 1.3 cm^2 . The other side of the BASE was coated with 20 nm-thick Sn, and a 300 μm -thick Na foil was used as the anode. Solid-state full cells were also fabricated in the pressured die cells with initial pressure of 40 psi.

5.2.5 Electrochemical Measurement

The ionic conductivity of the BASE pellet electrolyte and PEO electrolyte was

measured in Au/BASE or PEO/Au blocking cells, where Au was sputtered through a Sputter Coater 108auto (Cressington Scientific Instruments). Electrochemical impedance spectra were collected with AC amplitude of 5 mV and a frequency range of 1 MHz~0.1 Hz on an electrochemical workstation (VMP3, Bio-Logic Co.). Galvanostatic tests were performed at current densities ranging from 0.1C to 0.5C (1C = 409 mA g⁻¹). Solid-state cells were measured at 60 °C while liquid cells were tested at room temperature.

5.3 Interfacial Engineering with Auxiliary Wetting Agents

BASE has excellent structural, electrical, and mechanical properties and are widely used in commercial high-temperature Na-S batteries.¹⁵⁴ In this work, BASE was selected to pair with a high capacity PTO cathode. Figure 5.1a shows the Arrhenius curve of BASE's ionic conductivities. The characteristic layered structure (rhombohedral; *R3m*) of BASE is confirmed by X-ray diffraction (XRD) analysis (Figure 5.1b), BASE exhibits a low activation energy of 0.3 eV and a high Na-ion conductivity of 1.1 mS cm⁻¹ at 60 °C, superior to most of the reported Na-ion SEs.¹¹⁹ Moreover, BASE forms a highly dense layer with relative density over 98% (inset of Figure 5.1a), revealing its ability to potentially suppress dendritic Na growth.¹⁰⁶

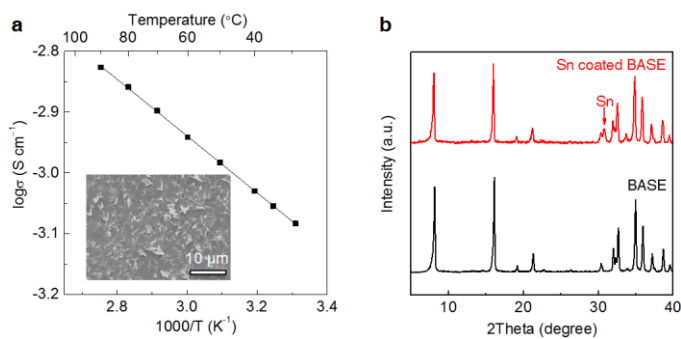


Figure 5.1 (a) Arrhenius plot of ionic conductivity of BASE. Inset: cross-sectional scanning electron microscopy (SEM) image of a BASE pellet. (b) X-ray diffraction patterns of the BASE with and without Sn coating.

However, one of the key challenges hindering the application of BASE in all-solid-state-batteries is its poor wettability with metal anode (Figure 5.2a). This challenge has been observed for other oxide-based SEs, such as $\text{Li}_7\text{La}_3\text{Zr}_2\text{O}_{12}$ (LLZO) and NASICONs¹⁹⁵.

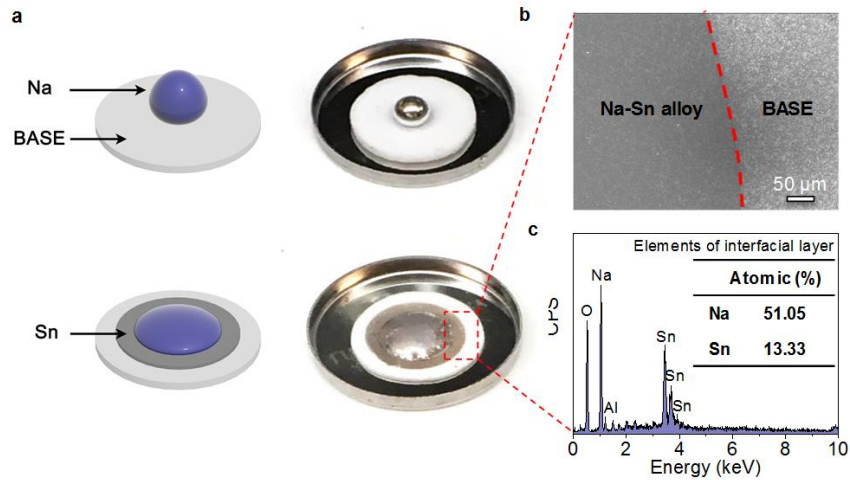


Figure 5.2 (a) Different wetting behaviors of molten Na on bare and Sn-coated BASE. (b) Magnified SEM image of coated vs. uncoated portion of BASE. (c) Energy dispersive spectroscopy (EDS) shows the formation of NaSn alloy.

In a recent study, Hu et al. demonstrated that an interlayer could greatly improve the wettability of lithium metal on garnet-type oxide-based SEs by forming alloys at the interface.²⁰¹ To overcome the interfacial barrier between Na and BASE, we deposited a 20-nm-thick Sn layer via thermal evaporation on the surface of BASE (Figure 5.3). The diffraction peak of Sn thin layer is shown in Figure 5.1b. The Sn layer reduced the surface roughness and lowered the surface tension of Na (Figure 5.2b), thus allowing the molten Na to better wet and simultaneously alloy with Na to form a $\text{Na}_{15}\text{Sn}_4$ interlayer as confirmed by the energy dispersive (EDS) spectrum (Figure 5.2c) and XRD patterns. Note the process of forming Na-Sn alloy is kept at 150 °C for 30 minutes. The $\text{Na}_{15}\text{Sn}_4$ interlayer improves the wettability of Na metal on the BASE by forming ‘sodiophobic’ to

‘sodiophilic’ contact (Figure 5.2a) and specifically provides the necessary ionic/electronic conduction for Na plating/stripping.

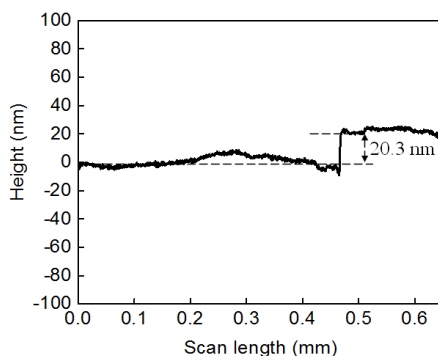


Figure 5.3 Profilometer measurement of a Sn layer.

Another interfacial barrier for ASSMBs arises from the cathode-electrolyte interface,^{32, 202} where rigid solid-solid contact forms between the quinone composite cathode and oxide SE, resulting in poor interfacial ionic transport. The high hardness and sintering temperature of BASE restrict the conventional approaches (*e.g.* co-pressing and co-sintering,¹³¹) of achieving intimate contact because the sublimation temperature of PTO is around 300 °C. Alternatively, polymer electrolytes can serve as a mechanically compliant ionically conductive auxiliary agent to improve cathode-electrolyte contact. A PTO-PEO composite cathode was prepared in a full cell with a Na metal anode (Figure 5.4a). Incorporation PEO into the cathode simultaneously increases the interfacial contact between cathode and BASE as well as contact inside the cathode. As shown in the cross-sectional SEM in Figure 5.4b, there is no discernable gap between the composite cathode and BASE layer. Furthermore, Figure 5.4c shows uniform distribution and intimate contact among the cathode components, highlighting the interpenetrating ionic and electronic pathways that favor the full utilization of PTO. For comparison, when PEO is absent in the cathode composite, unfavorable cathode-BASE and inter-particle contact

are observed (Figure 5.5).

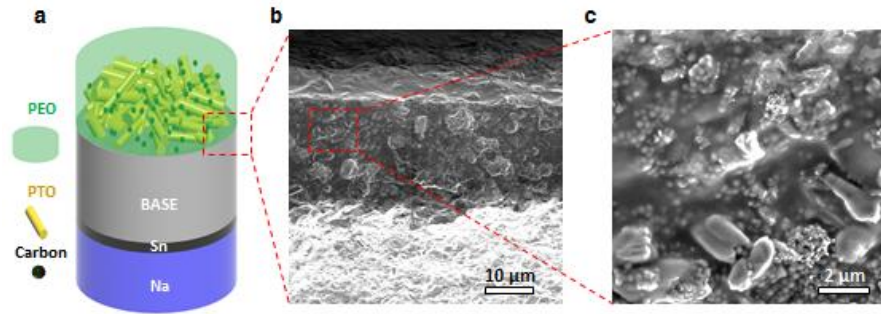


Figure 5.4 (a) Schematic of Na/Sn/BASE/PTO-PEO structure. (b–c) SEM images highlight the intimate contact between the cathode composite and BASE.

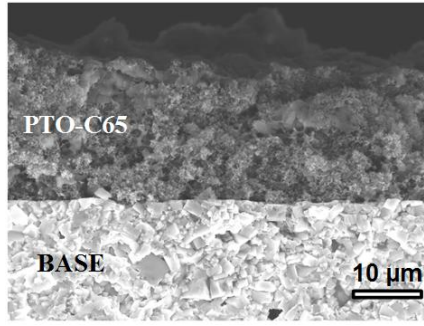


Figure 5.5 A cross-sectional SEM image highlights the non-ideal mechanical contact between PTO-C65 cathode and BASE electrolyte.

5.4 Improved Electrochemical Performance

Compatibility of BASE with Na metal anode was examined in symmetric Na-Na cells. The cells with bare BASE exhibited fluctuating voltage profiles and quickly short-circuited as shown in Figure 5.6a, which is attributed to the poor contact and non-uniform plating-stripping. In comparison, the Na/Sn/BASE/Sn/Na cell presents a much more stable electrochemical Na plating-stripping voltage profile with much smaller hysteresis due to the significant decreased areal specific resistance (ASR) from the EIS spectra (Figure 5.6a and 5.6b). The total ASR of the Na/Sn/BASE/Sn/Na symmetric cell is only $54 \Omega \cdot \text{cm}^2$. This value is two orders of magnitude lower than that of the Na/BASE/Na cell

($3359 \Omega \cdot \text{cm}^2$) (Figure 5.6a), and is superior compared to previous reports of symmetric cells. The EIS spectra were further interpreted by fitting Nyquist plots according to the equivalent circuit shown in the inset of Figure 5.6b with the fitting parameters in Table 5.2. The characteristic frequencies of different electrochemical processes are employed to identify the electrolyte bulk resistance (R_b), interfacial resistance (R_i), and charge-transfer resistance (R_{ct}) from the total ASR of the spectra.¹⁵⁸ The incorporation of an ultrathin Sn interlayer at the Na/BASE interface dramatically lowers the R_i and R_{ct} to $9.6 \Omega \cdot \text{cm}^2$ and $26.7 \Omega \cdot \text{cm}^2$, respectively, indicating the interface modification approach presented here is comparable to those shown for interface-engineered garnet-type SEs.¹⁵⁶

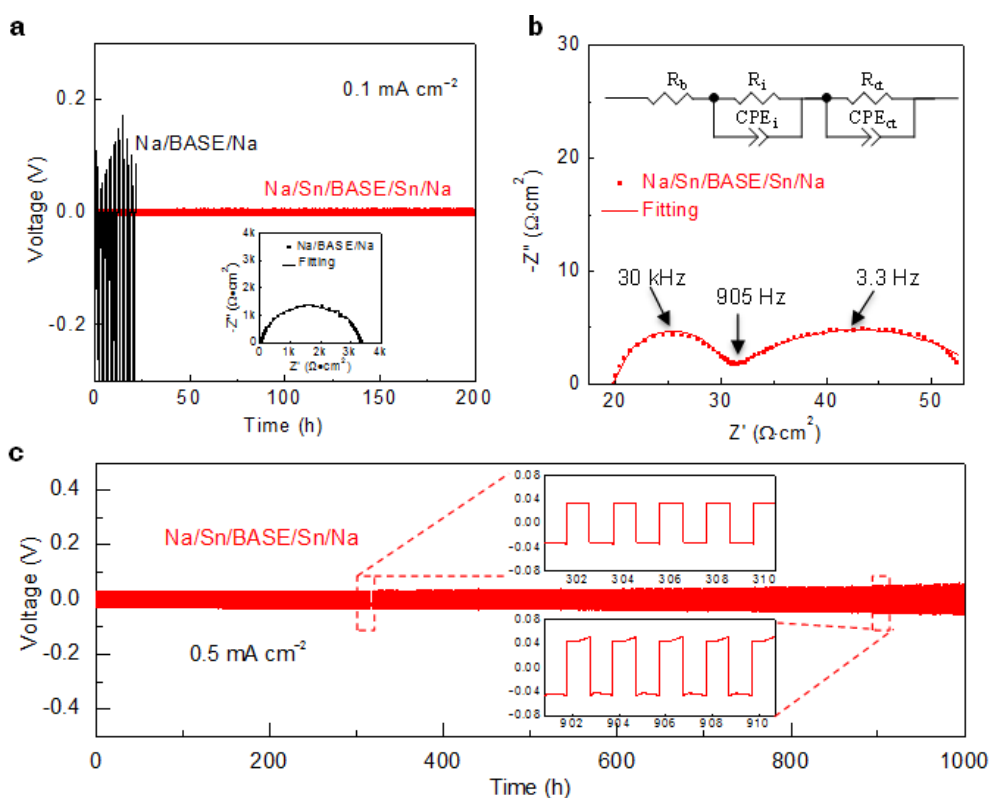


Figure 5.6 (a) Voltage profiles of the Na/BASE/Na cell. Inset: EIS spectrum. (b) EIS spectrum of the Na/Sn/BASE/Sn/Na cell. (c) Voltage profiles of the Na/Sn/BASE/Sn/Na cell.

Figure 5.6c shows the cycling stability of a symmetric cell at a higher current

density of 0.5 mA cm^{-2} . The cell exhibited an initial overpotential of a mere 30 mV with no obvious increase in polarization after 1000 h. To the best of our knowledge, this is the first report of Na/SEs/Na symmetric cells that can stably cycle at a high current density of 0.5 mA cm^{-2} and maintain a long cycle life of 1000 h. Such an outstanding stability of Na plating-stripping behavior of the Sn-modified BASE demonstrates the advantages of surface coating in improving the interfacial contact between Na metal anode and oxide SEs.

Table 5.2 EIS spectra fitting of the symmetric cells shown in the inset of Figure 5.6a and Figure 5.6b. R_b , R_i , and R_{ct} represent the resistance of the BASE bulk, the resistance of the interphase, and the charge transfer resistance.

Symmetric Na cells	$R_b (\Omega \cdot \text{cm}^2)$	$R_i (\Omega \cdot \text{cm}^2)$	$R_{ct} (\Omega \cdot \text{cm}^2)$
Na/BASE/Na	40.6	3255	86.5
Na/Sn/BASE/Sn/Na	20.1	9.6	26.7

For the PTO-PEO composite cathode, Table 5.3 shows 50-fold increase in interfacial resistance (R_i) from $220 \Omega \cdot \text{cm}^2$ to $10,800 \Omega \cdot \text{cm}^2$ when PEO is absent. These results illustrate the important function of PEO in overcoming the challenges of cathode-electrolyte interface in a functioning ASSMB.

Table 5.3 Fitting results for the EIS spectra shown in Figure 5.7a. In the equivalent circuit, W_s represents the Warburg diffusion resistance. R_b , R_i , R_{ct} , refer to the same definitions as above.

Full cells	$R_b (\Omega \cdot \text{cm}^2)$	$R_i (\Omega \cdot \text{cm}^2)$	$R_{ct} (\Omega \cdot \text{cm}^2)$	$W_s (\Omega \cdot \text{cm}^2)$
Na/Sn/BASE/PTO	37.1	10,800	1430	5,030
Na/Sn/BASE/PTO-PEO	16.8	220	456	1,010

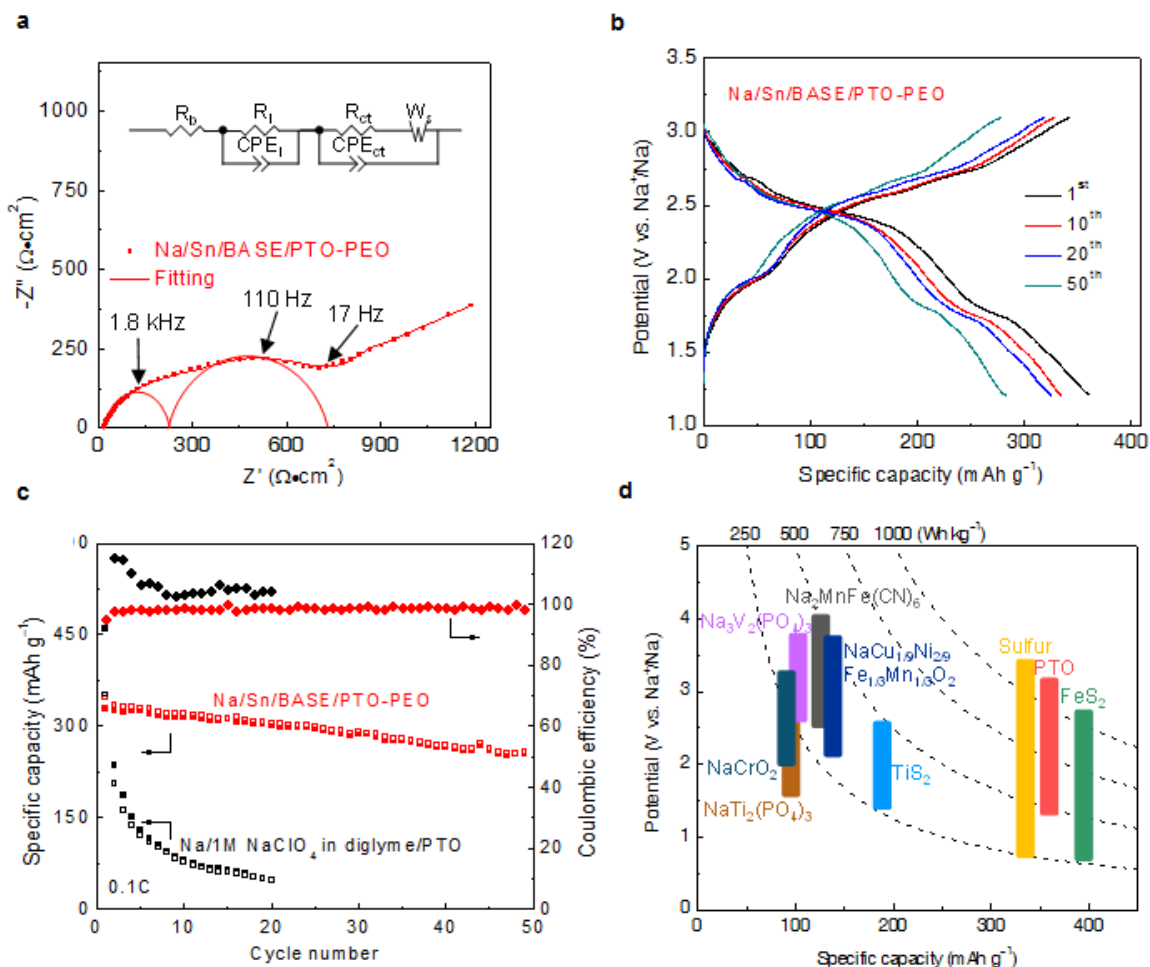


Figure 5.7 (a) EIS spectrum and corresponding equivalent circuit. (b) Voltage profiles at 0.1C for 50 cycles. (c) Cycling stability and coulombic efficiency vs. cycle number. (d) A comprehensive comparison with all reported ASSMBs.

PTO can deliver a high initial discharge specific capacity of 362 mAh g^{-1} and a coulombic efficiency of 95% in Figure 5.7b. A stable cycling with 80% capacity retention over 50 cycles and a high coulombic efficiency of $\sim 100\%$ are demonstrated in Figure 5.7c, in sharp contrast to the performance when liquid electrolyte is used. The presented ASSMB successfully addresses the dissolution and shuttling issues. The finely tailored cathode and anode interfaces, with low interfacial resistance summarized in Table 5.2 and 5.3, enable excellent rate capability (Figure 5.8).

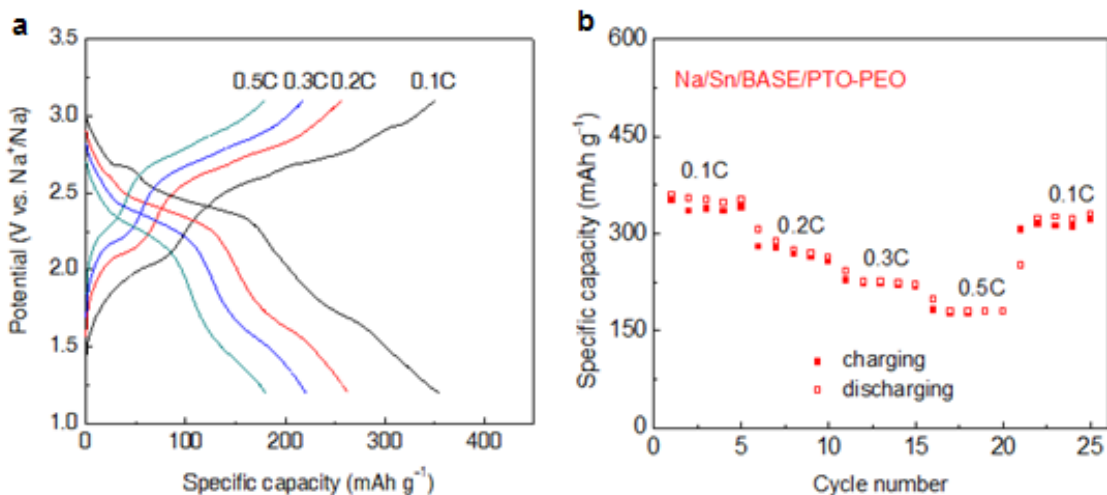


Figure 5.8 Electrochemical performance of an all-solid-state cell (Na/Sn/BASE/PTO-PEO) using PEO as a cathode side interlayer measured at 60 °C. (a) Galvanostatic voltage profiles and (b) cycling at different C rates.

At 0.5C, PTO can offer a discharge capacity of 180 mAh g⁻¹, corresponding to a power density of 220 W kg⁻¹. Furthermore, the cell exhibits initial energy density of ~900 Wh kg⁻¹ calculated based on the cathode specific capacity of 362 mAh g⁻¹ (only the mass of active material is considered) and the average voltage of 2.46 V vs Na/Na⁺, the highest among all the reported ASSMBs using intercalation-type cathodes.

5.5 Conclusions

In summary, the dissolution and shuttling issues of high-capacity organic quinone-based electrodes are addressed in this work by designing an all-solid-state battery. The Na metal/BASE interface and the PTO cathode/BASE interface were effectively ameliorated by introducing an ultrathin Sn metal interlayer and a mechanically compliant ionically conductive polymer auxiliary agent, respectively. Due to the formation of Na₁₅Sn₄ alloy at the interface after Sn coating, the wettability of Na metal on BASE was obviously transformed from sodiophobic to sodiophilic, and the cycling stability of the

corresponding Na symmetric cell was remarkably enhanced. In addition, PEO in the cathode composite facilitates both intimate inter-particle and inter-layer contact. Our approach has led to an organic ASSMB with a remarkably high energy density of 900 Wh kg⁻¹. We believe that the proof-of-concept demonstration and interfacial engineering approaches presented here can be extended to other SEs and organic cathodes to promote the exciting development of ASSMBs.

Chapter 6 Methods and Tools used in Solid-state Battery

Research

6.1 Solid-State Electrolyte Synthesis

Solid-state electrolytes (SEs) are the most critical component for the development of solid-state batteries. Therefore, synthesis of high-quality SEs is one of the most important skills for solid-state batteries researchers. The detailed illustration of synthesis procedures for oxide-based SEs can be found in this review paper.²⁰³ Briefly, precursors are mixed in stoichiometry ratio and pressed into pellets and finally sintered with high temperatures. It is noteworthy that the lithium or sodium loss becomes very prominent at such high sintering temperatures. To compensate the lithium or sodium loss of the oxide-based SEs, the green SE pellets are typically covered with mother powders with the same composition. Sulfide-based SEs are more deformable and therefore more readily synthesized compared to oxide-based SEs. Mechanochemical-synthesis and solution-synthesis are two main approaches for sulfide-base SEs synthesis and routines will be described in 6.1.1 and 6.1.2.

6.1.1 Mechanochemical-Synthesis Method

Mechanochemical-synthesis via high-energy ball milling is the most popular way for synthesizing sulfide-based SEs. For example, in the $75\text{Li}_2\text{S}-25\text{P}_2\text{S}_5$ binary system of glassy Li-ion conductor, the glass modifier Li_2S and glass former P_2S_5 were added into the stainless-steel milling jar with the stoichiometry ratio. For a standard 250 mL milling jar, two grams of precursor powders with milling balls ($2 \times \Phi 15\text{mm}$ and $20 \times \Phi 10\text{mm}$) were tightly sealed in the milling jar and ball milled with the desired speed and time.

Five-hundred rpm at 20 hours was the common recipe for yielding 75Li₂S-25P₂S₅ glassy electrolyte. During the tedious milling process, precursor powders are easily agglomerating and coated on the surface of the milling jar and balls, leading to an insufficient mixing and deviation of the stoichiometric compositions. To solve this problem, an initial low energy milling process with slow 300 rpm and 1 hour was applied to achieve a sufficient mixing degree before the mechanochemical reaction. The high-energy ball milling process in general yields glassy sulfide-based electrolytes which are amorphous with a relatively ionic conductivity of 10⁻⁵ ~ 10⁻⁴ S/cm.²⁰⁴ The post annealing treatment at or above the crystallization temperature of the as-synthesized SEs can enhance the conductivity to 10⁻⁴ ~ 10⁻² S/cm by introducing the crystalline phases into the amorphous structure and these types of SEs are usually called glass-ceramic sulfide-based SEs (50-95 vol% crystalline) or ceramic (100 vol% crystalline) sulfide-based SEs.²⁰⁵ To determine the annealing temperature, the differential scanning calorimetry (DSC) measurement is usually conducted as shown in Figure 6.1.

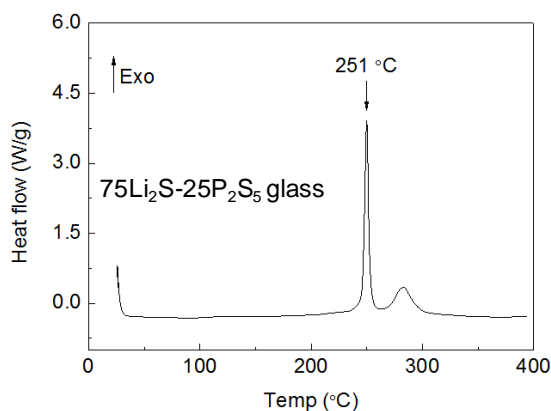


Figure 6.1 DSC measurement of the as-synthesized 75Li₂S-25P₂S₅ glassy electrolyte.

An obvious crystallization peak at 251°C provides the guidance for the annealing temperature. A 2-hour vacuum annealing with 260°C temperature can form glass-ceramic

Li₃PS₄ SE. To have a uniform heating process, the as-synthesized glassy SE powder should be pressed into pellets before the annealing process.

6.1.2 Solution-Synthesis Method

Recently, many studies have reported the synthesis of sulfide-based SEs via solution chemistry using liquid solvents as the mediums. It has several advantages such as: scalability, low cost, and homogeneity.²⁰⁶ The pioneering work is from Liu et al.⁸⁰, who developed a wet-chemical method for synthesizing ceramic β -Li₃PS₄. This electrolyte was prepared with precursors of Li₂S and P₂S₅ in tetrahydrofuran (THF). The removal of THF from the Li₃PS₄·3THF complex leads to the glassy Li₃PS₄, the subsequent heat treatment at 140°C converts the amorphous phase to a crystalline phase. In addition to THF, various solvents have been applied to successfully synthesize electrolytes such as acetonitrile (ACN),^{7, 207-209} 1,2-dimethoxyethane (DME),^{210, 211} and ethyl propionate (EP).²¹² In addition to the advantages mentioned above, the particle size from solution-synthesized SEs is usually smaller and more uniform than that from the traditional ball milling process, which will be discussed in 6.2.1.

6.2 Characterization of Solid Electrolytes

The as-synthesized SEs are not ready for battery fabrication until all important properties have been properly characterized and meet requirements or reported values. Four critical property characterization methods including particle size, crystalline structure, ionic conductivity, and electrochemical stability window will be discussed in the following sections.

6.2.1 Particle Size

The particle size can be characterized by SEM. Due to the moisture sensitivity of

the sulfide-based SEs, these samples need to be sealed in an Argon-filled jar or transfer box and quickly transferred to the SEM chamber to minimize the exposure to the air. The smaller particle size is normally desirable and beneficial for improving the contact area with active material and carbon to achieve a higher material utilization. However, due to the possibility of electrolyte decomposition, a larger contact area may also lead to an expectedly more severe electrolyte decomposition. Therefore, the size control can be extremely crucial but most likely overlooked for battery fabrication. Figure 6.2 shows the particle size from three synthesise methods.

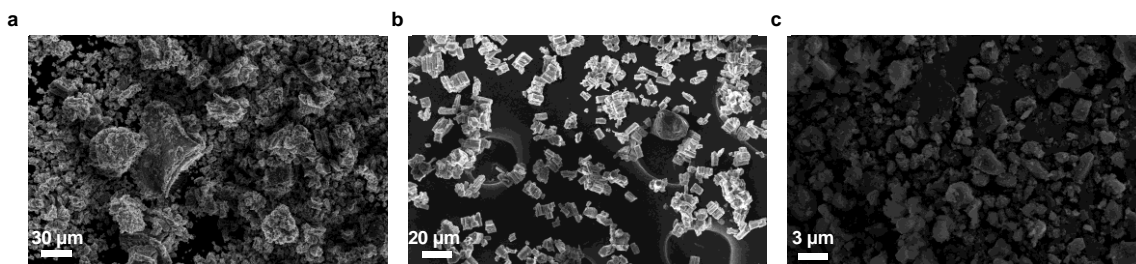


Figure 6.2 SEM images of glass ceramic Li_3PS_4 electrolyte synthesized by (a) high energy ball milling. (b) solution synthesized with THF. (c) high energy + low energy ball milling followed by sifting.

It is obvious that the solution synthesized Li_3PS_4 (Figure 6.2b) is more advantageous than the traditional ball milling method (Figure 6.1a) as the particle size is much smaller and more uniformly distributed. Further low-energy ball milling in an agate jar with ~ 40 agate milling balls (500 rpm, 4 hours) and sifting can downsize the particle to $\sim 1 \mu\text{m}$ (Figure 6.3c). Therefore, low-energy ball milling and sifting should be considered as a routine for synthesizing SEs to maximize the contact area with other components in the composite cathode.

6.2.2 Crystalline Structure

Crystalline structure can be examined by XRD. The purpose is to compare the

peaks to the reported ones and identify the purity of the as-synthesized SEs. The sample preparation is the tricky part for the XRD measurement. The SE powders are covered by Kapton tape with small background peaks to prevent the exposure to the air. The peaks must be scrutinized with the reference or PDF card before using for battery fabrication. Figure 6.3 shows a comparison of XRD patterns between the reported Li_3PS_4 (Figure 6.3a)²¹³ and the home-made Li_3PS_4 (Figure 6.3b). The as-synthesized glassy $75\text{Li}_2\text{S}-25\text{P}_2\text{S}_5$ SE shows no crystalline peaks, indicating it has an amorphous structure. After heat-treatment, glass ceramic Li_3PS_4 shows its characteristic peaks and our home-made Li_3PS_4 exhibits the same peak position and relative peak intensities compared to the reported one.

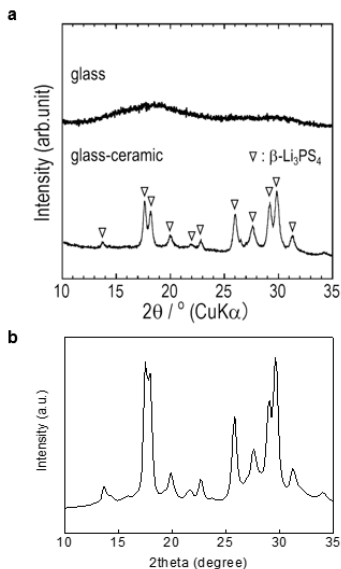


Figure 6.3 The XRD patterns of the reported glassy $75\text{Li}_2\text{S}-25\text{P}_2\text{S}_5$, glass ceramic Li_3PS_4 (Figure 6.3a), and our home-made glass ceramic Li_3PS_4 (Figure 6.3b). Figure 6.3a is reprinted with permission from Ref. 213. © 2017 Springer Nature.

6.2.3 Ionic Conductivity

High ionic conductivity is the prerequisite for qualified SEs to provide fast ionic transportation. To measure the time-dependent ionic conductivity, electrolyte (~150 mg)

powder is first pressed into a dense pellet with 5 metric tons (375 MPa) for 5 min. The copper nano-powder (30 mg) is sequentially dispersed on each side and co-pressed with 3 metric tons (225 MPa) for 5 min to improve the contact between the electrolyte and the current collector. An AC perturbation of ~ 7 mV is applied to the system to excite the internal dynamic feedback at different frequency range. The measurement starts from a high frequency 1 MHz to a low frequency 0.1 Hz and the representative Nyquist plot is shown in Figure 6.4a. The bulk resistance (R_b) and grain boundary resistance (R_{gb}) will show at high frequency range, and ionic conductivity can be calculated from the total resistance (R) with the given thickness (L) and area of the electrolyte (A) as shown in Equation 6-1:

$$\sigma = \frac{L}{A \times R} \quad (6 - 1)$$

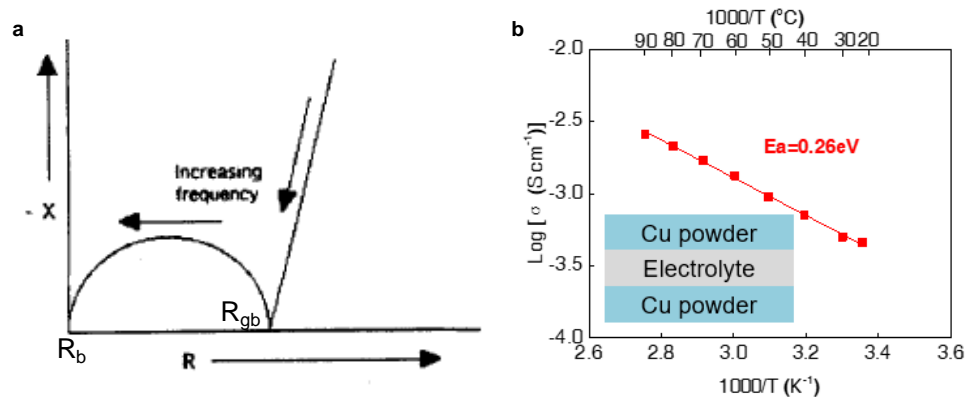


Figure 6.4 (a) The representative EIS spectra of solid electrolyte for ionic conductivity measurement. (b) The temperature-dependent ionic conductivity of Li_3PS_4 . Inset is the cell architecture for ionic conductivity measurement

As the electrodes on both sides are copper, which are electronic conductors, a significant diffusion resistance is observed as a straight line inclined at a certain angle (or so-called tail part) because the ionic diffusion was heavily impeded, indicating the ionic

conductivity is the much more dominant part for the solid electrolyte. On the other hand, if a certain electrolyte has a more dominating electronic conductivity measurement, there will be no tail part in the EIS spectra as the electronic diffusion resistance will be extremely small and the spectra will present like a full semi-circle.

Figure 6.4b shows Arrhenius an plot for Li_3PS_4 electrolyte. The activation energy (E_a) that indicates the barrier for Li-ion migration can be calculated from linear fitting between the $\ln\sigma$ versus $1/T$. Then, the slope will be $-E_a/R$, where R is the a constant equal to $8.314 \text{ J/mol}\cdot\text{K}$.

6.2.4 Electrochemical Stability Window

The electrochemical stability window (ESW) has been considered as the most critical value for the new developed SEs as it determines the interfacial compatibilities between electrode and electrolyte. Thermodynamically ESW can be calculated by DFT but kinetically ESW is more accurate and directly related to the interfacial compatibilities. The cell architecture for ESW measurement is shown as Figure 6.5.

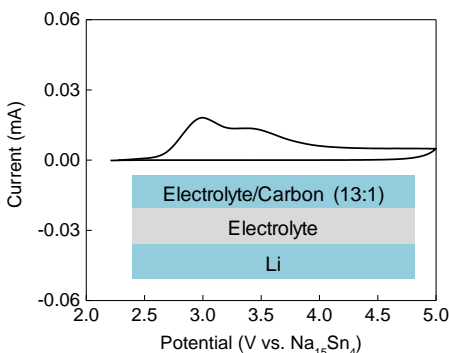


Figure 6.5 Cyclic voltammetry profile and cell architecture for electrochemical stability window measurement.

The electrolyte (~150 mg) powder is first pressed into a pellet with 2 metric tons (150 MPa) for 5 min. The hand grinded composite cathode consisting of electrolyte and

carbon with 13:1 mass ratio will be sequentially dispersed on the top side and co-pressed with 5 metric tons (375 MPa) for 5 min. The introduced carbon aims to improve the contact area and increase the electronic conductivity for the composite cathode, reflecting the accurate ESW. Finally, the Li foil is attached to the bottom side and pressed with a 20 inch-pound torque. The cyclic voltammetry (CV) measurement is conducted with a slow scan rate (0.05 mV/s) and proper scan direction. For example, the upper voltage limit is set to 5 V when examining the anodic stability window as shown in Figure 6.4. The apparent anodic decomposition peak at 2.7 V indicates this electrolyte will be oxidized at 2.7 V.

6.3 Anode Materials Synthesis

Li/Na metal are always the more desirable anode material than the corresponding alloyed anode materials due to their lower potential to the standard hydrogen electrode (SHE). However, not all electrolytes are stable against Li/Na metals. Therefore, it is necessary to synthesis alloyed anode materials to be stable with electrolyte, although it sacrifices the specific energy.

6.3.1 Na-Sn alloy

$\text{Na}_{15}\text{Sn}_4$ alloy is one the most common anode alternative for Na metal.¹⁴⁸ $\text{Na}_{15}\text{Sn}_4$ has a potential of 0.1 V vs. Na^+/Na and can be synthesized via a high-energy ball milling process (500 rpm and 20 hours) with stoichiometry ratio.

6.3.2 Li-In alloy

$\text{Li}_{0.5}\text{In}$ alloy is a widely used anode material to replace Li metal.²¹⁴ It has a potential of 0.6 V vs. Li^+/Li and can be synthesized as follows: Pieces of indium foil (thickness of 0.3 mm, diameter of 9 mm) and lithium foil (thickness of 0.1 mm, diameter

of 8 mm) are pressed under a pressure of 100 MPa.²¹⁵

6.4 Size Reduction for Cathode Active Materials

Similar to the discussion in 6.2.1, the smaller cathode active material particle size will have the larger contact area with electrolyte and carbon, improving the efficiency of the percolation network and material utilization.

6.4.1 Ball-Milling Method

Low-energy ball milling is commonly used to downsize the particle. Instead of using stainless steel milling jar and balls, an agate milling jar and ~40 milling balls will be used for the low-energy ball-milling process. The common recipe will be 500 rpm with 10 hours.

6.4.2 Precipitation Method

The chemical antisolvent precipitation method is another approach to get fine particle. For example, 50 mg as-synthesized PTO active material can be dissolved in 13 mL of tetrahydrofuran (THF, anhydrous, $\geq 99.9\%$, Sigma–Aldrich) and quickly injected into 70 mL of deionized water. After sonication for 10 min, yellow precipitates were collected by centrifuging at 10,000 rpm for 15 min and subsequent vacuum drying overnight. Figure 6.6 summarizes the PTO particle size evolution that is treated by ball-milling and precipitation methods.

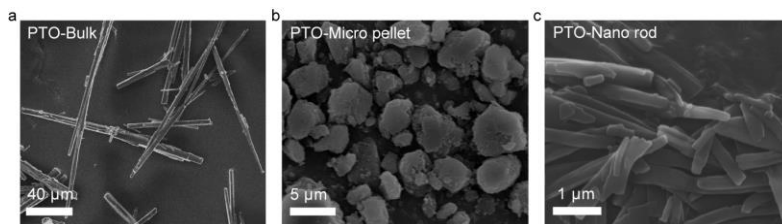


Figure 6.6 (a) As-synthesized PTO. (b) PTO-Micro pellet that treated by low-energy ball milling process. (c) PTO-Nano rod that treated by precipitation method.

6.5 Physicochemical Characterization Methods

The physicochemical properties of electrode and electrolyte materials have recently attracted considerable attention as they are closely related to the performance of solid-state batteries. Therefore, the characterization methods for mechanical properties, percolation network, and chemical compositional information will be detailed in the following sections.

6.5.1 Mechanical Properties Measurement by Indentation

Mechanical properties such as Young's modulus and hardness reflects the deformability for cell fabrication and the capability of achieving intimate contact between electrode and electrolyte materials. The classic Oliver and Pharr indentation method that was developed in 1992 is still in use today.¹⁴⁹ The modulus and hardness were extracted from the load-displacement curves as shown in Figure 6.7.

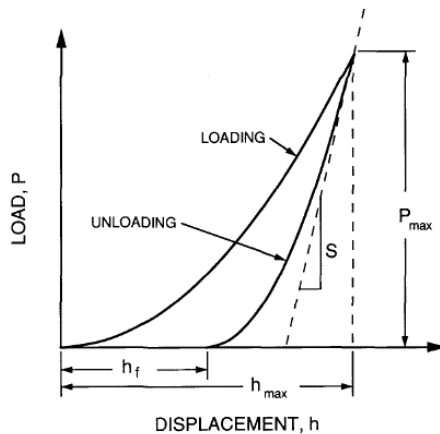


Figure 6.7 The load-displacement curve for an indentation experiment. Reprinted with permission from Ref. 149. © 1992 Materials Research Society.

E and ν are Young's modulus and Poisson's ratio for the sample and E_i and ν_i are the parameters for the indenter in Equation 6-2:

$$\frac{1}{E_r} = \frac{(1 - \nu^2)}{E} + \frac{(1 - \nu_i^2)}{E_i} \quad (6 - 2)$$

the $S = dP / dh$ in Equation 6-3 is the measured stiffness of the upper portion of the unloading data and A is the contact area:

$$S = \frac{dP}{dh} = \frac{2}{\sqrt{\pi}} E_r \sqrt{A}. \quad (6 - 3)$$

Therefore, the Young's modulus can be derived by measuring the unloading stiffness S . The hardness is defined as the maximum applied load P_{\max} divided by the corresponding contact area A as indicated in Equation 6-4:

$$H = \frac{P_{\max}}{A(h_c)}. \quad (6 - 4)$$

In our experiment, indentations under displacement control at a maximum depth of 1000 nm were conducted at 10 different locations using a standard Berkovich tip. The loading, holding, and unloading time is 10 s, 5 s, and 10 s, respectively. The sample powder was pressed with 5 metric tons (375 MPa) for 10 min into a dense pellet for minimizing the microcracks and gaps. The load-displacement curve of the Na_3PS_4 solid-state electrolyte is shown as Figure 6.8.

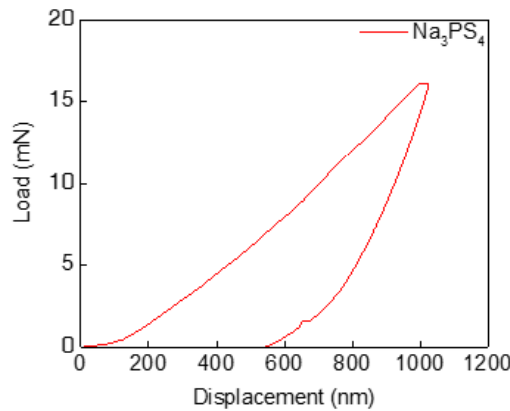


Figure 6.8 Load-displacement response of indentation of Na_3PS_4 .

6.5.2 Morphological Characterization by Focused-Ion-Beam Scanning Electron Microscopy and Three-Dimensional (3D) Reconstruction

A highly percolated ionic/electronic pathway in the composite cathode is required for achieving high-performance solid-state batteries. A quantitative analysis of the composite cathode with the 3D reconstruction technique provides the direct evidence of the microstructure of the composite cathodes. Figure 6.9 shows a flow scheme for a quantitative analysis using the 3D reconstruction technique. A cross-sectional composite cathode consisting of an active material and a solid electrolyte was first polished by focused ion beam in the directional perpendicular to the prepared sample, and the SEM image of the milled surface was taken at an angle of 52° . The region marked with a red dashed rectangle was selected as the area for the following 3D reconstruction (Figure 6.9a). Continuous slicing and imaging were performed 200 times with 50 nm intervals followed by the image alignment (Figure 6.9b). The obtained consecutive images were segmented based on the different gray-scale contrast and stacked to reconstruct a 3D volume microstructure of composite cathode including three components: solid electrolytes, active materials, and pores (Figure 6.9c).

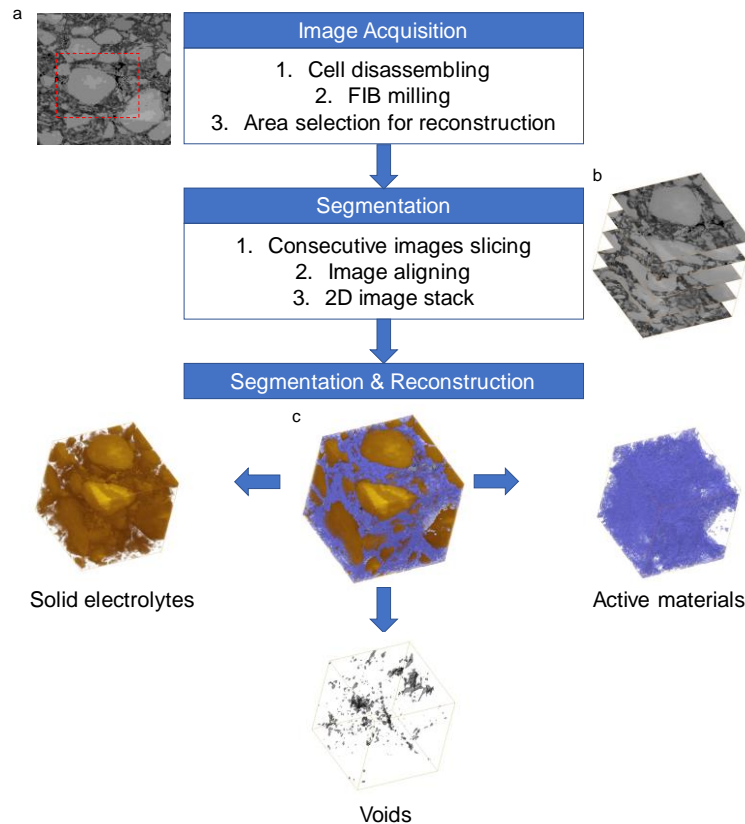


Figure 6.9 (a) Cross-sectional SEM image of the composite cathode. (b) Acquisition and align of consecutive SEM images. (c) 3D reconstruction of the composite cathode

6.5.3 Chemical Compositional Analysis by Time-of-Flight Secondary Ion Mass

Spectrometry (ToF-SIMS)

ToF-SIMS provides detailed elemental and molecular information about surface, thin layers, interfaces, and full 3D analysis of the samples. For ToF-SIMS analysis, a solid sample surface is bombarded with a pulsed primary Bi ion beam as shown in Figure 6.10. Both atomic and molecular ions are emitted from the outermost layers of the surface. These ions are accelerated with negative or positive bias and are collected and analyzed with a time-of-flight detector. A sputtering ion beam (Cs^+ with 1 keV ion energy) was used for depth profiling. To minimize air exposure, all samples were

transferred from an argon-filled vessel to the analysis chamber. In my recent published work,¹⁶² ToF-SIMS was used to analyze the interfacial decomposition products during battery cycling as shown in Figure 3.5f.

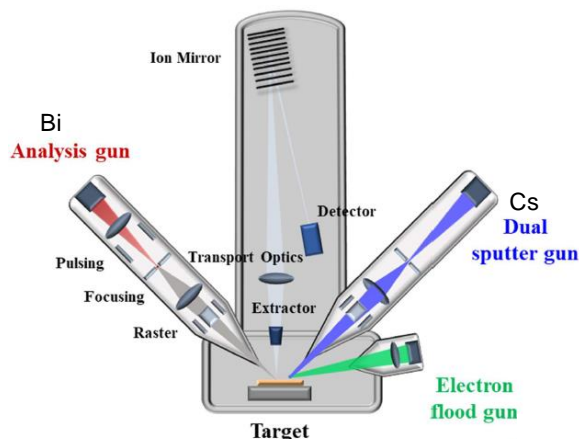


Figure 6.10 The schematic setup of ToF-SIMS.

6.6 Electrochemical Impedance Spectroscopy

Electrochemical impedance spectroscopy (EIS) can determine both the resistive and capacitive properties of materials. It has been widely used for analyzing ionic/electronic properties for electrode and electrolyte materials and interfacial diffusion resistance at the electrode-electrolyte interfaces for solid-state batteries.

6.6.1 Electronic Conductivities Measurement of Solid-State Electrolytes

The ideal solid electrolytes should have a high ionic conductivity but a negligible electronic conductivity. However, a recent study from Wang et al. reported that the high electronic conductivity could be the origin of the lithium dendrite formation.²¹⁶ Therefore, the electronic conductivity measurement is as important as the ionic conductivity measurement. The cell architecture for electronic conductivity measurement

has been shown in the inset of Figure 6.4b and a DC voltage of ~ 0.1 V will be applied at the cell for usually one hour.

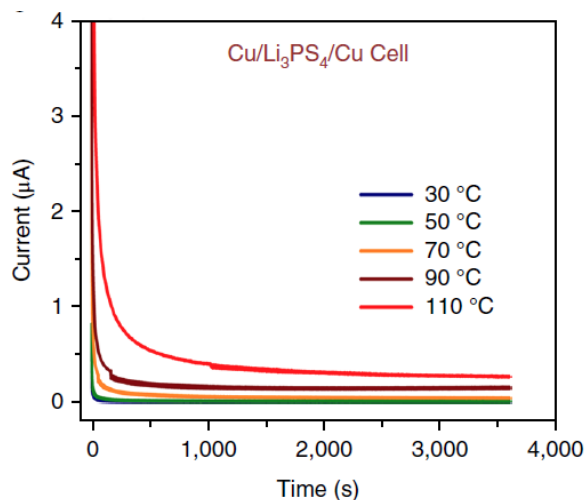


Figure 6.11 The representative current-time curves for electronic conductivity measurement. Reprinted with permission from Ref. 216. © 2019 Springer Nature.

With the ionic blocking electrodes of copper at both sides, the steady current can only be contributed from an electronic current. As shown in Figure 6.11, the electronic conductivity of Li_3PS_4 at room temperature is 2.2×10^{-9} S/cm, which is three magnitude higher than the ideal electronic conductivity of $\sim 10^{-12}$ S/cm for solid electrolyte.

6.6.2 In-Situ EIS Measurement at Various State-of-Charge

In-situ EIS measurement is an informative tool to reveal the interfacial evolution during cell cycling (Figure 3.5a). The experimental details can be found in section 3.2.4. Here, I want to introduce how to extract the Warburg coefficient from the raw EIS spectra. During the discharge process, the EIS measurement was conducted at five different discharge potentials and their corresponding EIS spectra are shown in Figure 6.12a. The Warburg coefficient A_w , which indicating the ionic diffusion resistance at the interface, can be obtained by plotting the real impedance against the reciprocal of the

square root of the frequency. The value of the slope from linear fitting in the low frequency range (1 Hz – 0.1 Hz) is the Warburg coefficient as shown in 6.12c. Figure 6.12b and 6.12d show the EIS spectra and corresponding linear fitting during charge process.

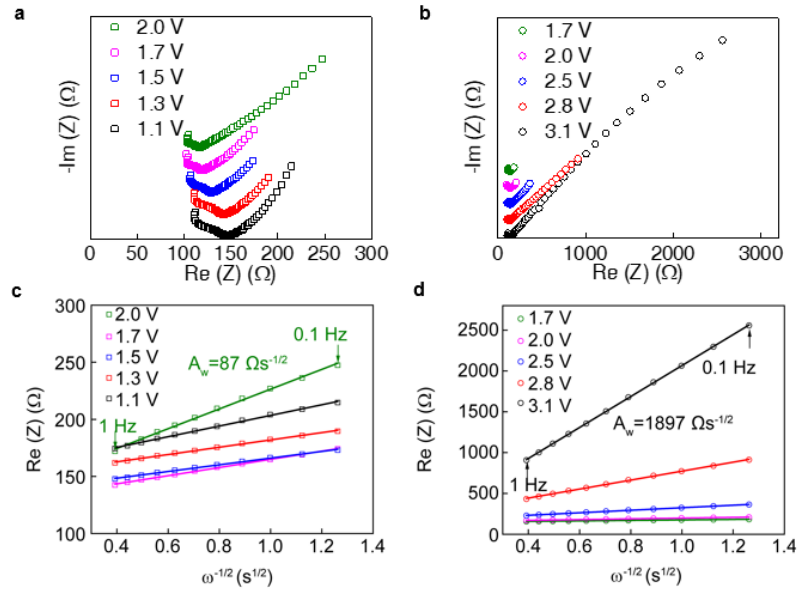


Figure 6.12 EIS spectra during (a) discharge and (b) charge process and their corresponding real part resistance versus minus square root of frequency during (c) discharge and (d) charge process.

6.6.3 Ionic/Electronic Conductivities Measurement of Cathode Active Materials

It is also important to investigate the ionic/electronic conductivities of cathode active materials to design the optimum composition of the composite cathode. For example, LiCoO₂ has decent electronic conductivity of $\sim 10^{-5}$ S/cm. Therefore, the carbon is usually not necessary for the LiCoO₂-contained composite cathode.

For the electronic conductivity measurement for active material, the cell architecture and test method are the same as above-mentioned as shown in Figure 6.13a.

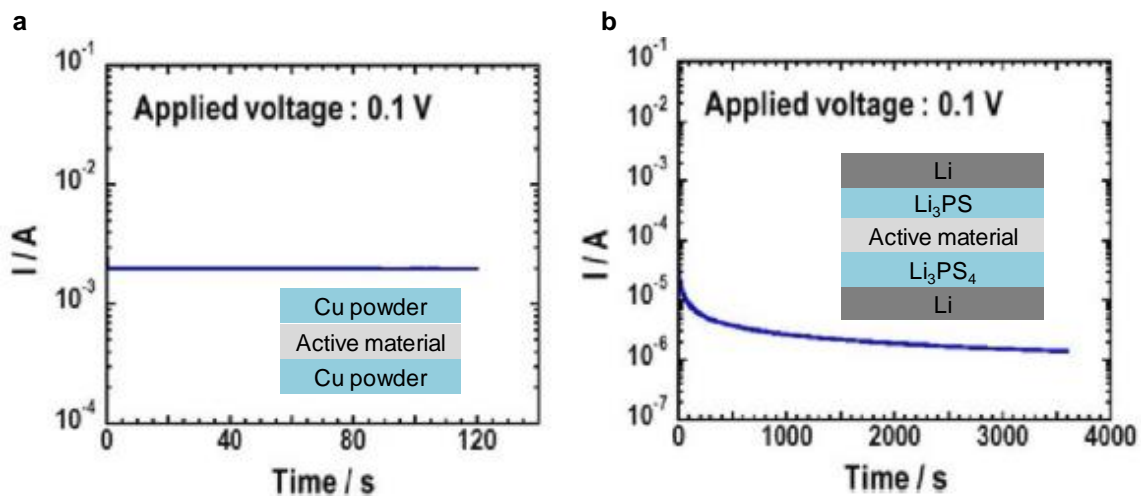


Figure 6.13 DC polarization curves for (a) electronic conductivity measurement and (b) ionic conductivity measurement of active material. Reprinted with permission from Ref. 217. © 2017 Elsevier.

For the ionic conductivity measurement, same DC bias will be applied but the electrodes will be replaced by the electron blocking electrodes, such as solid electrolyte Li_3PS_4 as shown in Figure 6.13b. The Li metal on both sides provide the Li source. Therefore, the steady current after 1 hour can be only contributed from ions transportation.

6.7 Full Cell Fabrication

6.7.1 Dry Mixing of Composite Cathodes for Bulk-Type Cells Fabrication

The electrochemical performance and cell architecture strongly depend on the processing approach of the composite cathode. Two categories of the composite cathodes are fabricated. Traditionally, dry mixing the active material, solid electrolyte, and carbon with a desirable mass ratio in an agate mortar with 10-15 min can form the composite cathode for fabricating solid-state batteries. It is noteworthy that the composite cathode can also be prepared by ball milling or freeze milling with a higher mixing degree.

However, it significantly depends on the compatibility between the active material, electrolyte, and carbon. The ball milling or freeze milling with much higher energy than hand grinding may lead to more severe decomposition. Then, ~150 mg of the solid electrolyte powder is pressed into pellet with 2 metric tons. The as-prepared composite cathode is then distributed uniformly on top of the electrolyte and co-pressed with 5 metric tons to achieve an intimate interlayer and interparticle contact. The anode materials such Li/Na metal will finally be attached to the bottom of the electrolyte and then pressed with 20 inch-pound torque and sealed with vacuum grease to prevent the air exposure. This type of solid-state battery is called bulk-type solid-state battery, which used a compressed powder pellet with the thickness of several hundred micrometers as a solid electrolyte separator.

6.7.2 Wet Mixing of Composite Cathodes for Sheet-Type Cells Fabrication

To increase the cell-level specific energy, the electrolyte thickness must be reduced to bring solid state batteries to reality as discussed in section 2.2.2. For this reason, the sheet-type solid-state batteries were recently attracting more attention by introducing binders into the electrolyte to provide mechanical strength during battery fabrication. Typically, the composite cathode slurry was prepared by wet-mixing the active material, solid electrolyte, carbon, and binder with the desirable mass ratio into solvent that can fully dissolve the selected binder. The solvent here plays a very important role as the electrolyte must not react with the selected solvent and the binder must exhibit a decent solubility into the solvent. The cathode slurry then coated on current collector using the tape-casting technique, followed by vacuum drying to remove the solvent. Similarly, the solid electrolyte slurry that containing solid electrolyte and binder are

dispersed uniformly in the solvent and directly tape-casted on top of the as-prepared cathode layer, followed by the same drying procedure as the composite cathode layer. Finally, the anode foil is attached and co-pressed. This type of solid-state battery is called a sheet-type solid-state battery with less than 100 micrometers thickness electrolyte, significantly reducing the weight of the cell and increasing the cell-level specific energy. The comparison in terms of the fabrication procedures between bulk-type solid-state batteries and sheet-type solid-state batteries is shown as Figure 6.14.

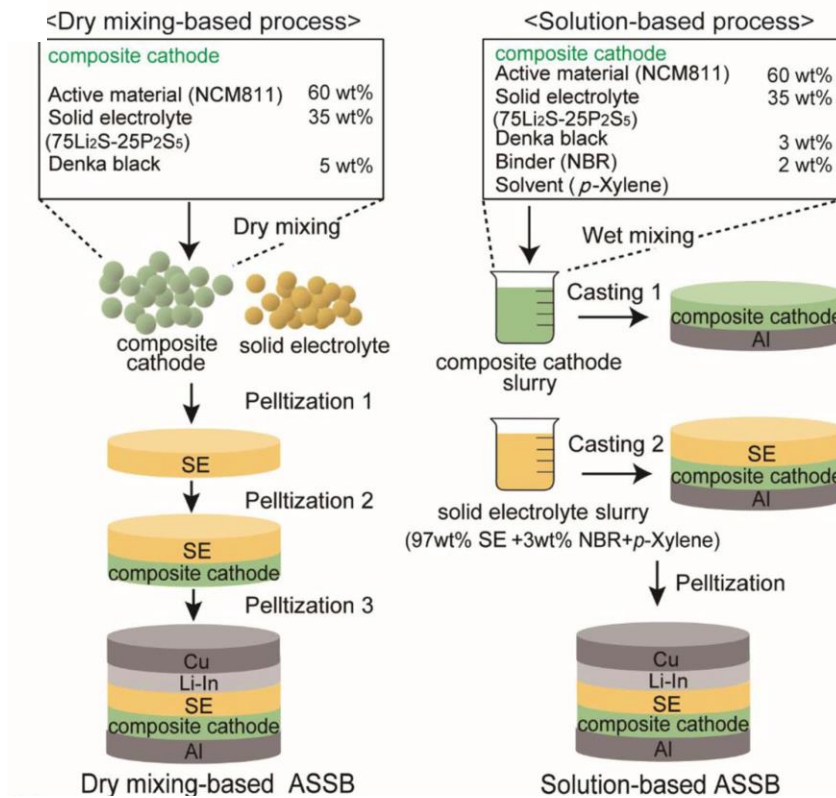


Figure 6.14 The comparison of fabrication procedures of bulk-type and sheet-type solid-state batteries. Reprinted with permission from Ref. 75. © 2017 The Electrochemical Society.

6.8 Symmetrical Cell Fabrication

The purpose of fabricating symmetrical cell is to measure the anode stability at

the anode-electrolyte interface. The solid electrolyte (~ 150 mg) will be first pressed into a dense pellet. If the anode material is Li or Na foil, it can be punched with the area of 1.3 cm² and directly attached to both sides of solid electrolyte pellet and pressed with 10 inch-pound torque. If the anode material is alloy powder, it needs to be distributed on both sides of electrolyte and co-pressed with 5 metric tons and pressed with 20 inch-pound torque for the test.

6.9 Full Cell Testing

For full cells testing, galvanostatic cycling is the typical method. The cycling current can be calculated by multiplying the theoretical capacity of the active material, active material loading in the composite cathode, and cycling C-rate.

6.10 Symmetrical Cell Testing

The anode stripping (negative current) and plating (positive current) process is taking place with designated current density and time. Typically, the test will begin with a relatively small current density of 0.1 mA/cm² and short time of 1 hour (capacity of 0.1 mAh/cm²). If the voltage profile is shown as Figure 4.6, it indicates the anode is not stable against electrolyte as the areal specific resistance (ASR) keeps increasing. ASR (ohm·cm²) can be calculated as voltage (mV) divided by current density (mA/cm²). The trend of ASR is the key to reflect the anode stability. If the ASR maintains constant at low current density and capacity, a higher current density can be applied and intermittently increased until the voltage profile exhibits a characteristic “peaking” shape, indicating a soft short-circuit is occurring. The voltage will gradually be decreasing and eventually becoming very stable with very small ASR, indicating the cell short completely.

Chapter 7 Summary and Outlook

7.1 Summary

This dissertation reports various electrode materials, electrolyte materials, and cell architectures to develop high-energy and long-cycle-life solid-state batteries for application in energy storage. I have demonstrated the effect of interfacial compatibilities between electrode and electrolyte on the battery performance and the approaches to achieve excellent compatibilities by using innovative active materials, electrolyte, and modified cell architecture.

This study starts from the urgent needs of the advanced energy storage system and the advantages of the solid-state batteries over the traditional liquid-based batteries. The motivation and the concept of developing solid-state batteries are discussed in Chapter 1, with a focus on features of solid-state batteries such as high safety, high energy, and unique architecture. Chapter 2 reviews relevant literature based on emerging solid-state electrolytes, architecture design, fabrication approaches, and large-scale fabrication challenges for solid-state batteries. The correlations between these perspectives and battery performance are revealed and the fundamental concept of these factors is deliberated. The main hurdles regarding interfacial incompatibilities of developing high-performance solid-state batteries are illustrated and the corresponding failure results related to interfaces are analyzed.

Chapter 3 begins with a detailed study on taming active material-solid electrolyte interface to achieve high-performance solid-state batteries by using organic cathode material. The quinone-based organic active material pyrene-4,5,9,10-tetraone (PTO) with

a higher theoretical specific capacity and a higher working potential can further improve the specific energy in solid-state batteries. PTO has a moderate redox potential (2.2 V vs. Na⁺/Na) that aligns with the electrochemical stability window of Na₃PS₄, ensuring a reversible electrolyte oxidation with controlled resistivity. Additionally, PTO's mechanical properties are first revealed by nanoindentation technique. The Young's modulus of PTO (4.2 ± 0.2 GPa) is approximately two orders of magnitude lower than that of oxide cathodes (100–200 GPa), which promises effective accommodation of interfacial stress and intimate inter-particle contact upon cycling, contributing to the excellent cycling stability. All above-mentioned advantages of PTO enable the PTO-based solid-state sodium-ion batteries to deliver a specific energy (587 Wh kg⁻¹ at 0.1C), a specific power (335 W kg⁻¹ at 1C), and 89% capacity retention over 500 cycles at 0.3C. This organic compound as cathode material opens a new opportunity to realize a stable electrode-electrolyte interface for enhancing performances of solid-state batteries, and it can be also applied to other all-solid-state energy storage system.

Chapter 4 focuses on developing new oxysulfide electrolyte for improving anode-electrolyte interfacial stability. An oxysulfide Na₃PS₃O glassy solid electrolyte that shows distinctive ability to form a defect-free and robust structure that excludes the possibility of grain-boundary dendrite penetration in oxide-based solid electrolytes, and substantial chemical/electrochemical stability that addresses the challenge of continuous interfacial decomposition in sulfide-based solid electrolytes. Systematic structural characterizations reveals that compared with pure sulfide-based solid electrolytes, the oxygen is introduced into the PS₄ structure units, leading to the formation of more oxide and oxysulfide units with bridging-oxygen characteristics. The unique structure and properties of the new

solid electrolyte enable hitherto the best cycling stability with Na metal over all the other known solid electrolytes. Furthermore, an ambient-temperature Na-S battery with $\text{Na}_3\text{PS}_3\text{O}$ demonstrates the highest yet reported energy density (1819 Wh kg^{-1}) among all the current sodium batteries. This study provides a very promising avenue of research towards the development of high-performance solid-state sodium metal batteries, and to all emerging solid-state batteries in general.

Chapter 5 solves the interfacial stability challenge by replacing sulfide electrolyte with oxide-based electrolyte with the wider electrochemical stability window and develops solutions to address interfacial contact challenges by introducing auxiliary wetting agents at the interlayers. I for the first time demonstrates an all-solid-state cell based on an oxide-based solid electrolyte (beta-alumina solid electrolyte, BASE), which not only enables PTO to deliver the highest energy (ca. 900 Wh kg^{-1} at the material-level) but also offers a sodium metal anode the best cycling stability (1000 h at 0.5 mA cm^{-2}) to date among the reported all-solid-state sodium metal batteries (ASSSBs). This work represents the first use of organic redox materials in oxide-based solid-state sodium batteries. The study establishes effective interfacial modifying strategies for developing high-performance solid-state sodium metal batteries, and to all emerging solid-state batteries in general.

Chapter 6 summarizes all fundamental and advanced methodologies that I used for solid-state batteries research. Numerous characterization techniques such as electrochemical impedance spectroscopy, DC polarization methods, focused-ion-beam scanning electron microscopy (FIB-SEM), nanoindentation, and time-of-flight secondary ion mass spectrometry (ToF-SIMS) are discussed. The fundamental synthesis methods for

electrode and electrolyte, processing procedures for the composite cathodes, and fabrication approaches for solid-state batteries are also introduced.

7.2 Outlook and Future Directions

Even with the promising results for developing solid-state batteries by above-mentioned approaches, realizing high-performance solid-state batteries remains challenging due to the high interfacial impedance. Addressing these issues requires a clear understandings and quantitative analysis of the chemical compositions and microstructure of the composite cathode, which however remain elusive. One of the future directions will be researching, developing, and demonstrating a systematic diagnostic technique combining chemical and structural information interfaces using time-of-flight secondary ion mass spectrometry (ToF-SIMS), focused ion beam scanning electron microscopy (FIB-SEM), 3D volume reconstruction. Successful demonstration of these diagnostic tools will provide us unprecedented details of the interfaces, their influences on battery performances, and possible ways to optimize them.

I have already initiated the morphological characterization by combining FIB milling and 3D reconstruction. As shown in Figure 6.9, the 3D reconstruction clearly shows the percolation network of the composite cathode and provides a clear angle for conducting further analysis such as: volume ratio, connectivity, porosity, and tortuosity, which are the key properties for achieving an effective ionic/electronic conducting network. This quantitative analysis will provide us a guidance for optimizing the processing and fabrication approaches for solid-state batteries with the improved performance. With this technique, we can bridge the knowledge gaps between the mechanical/morphological/compositional and electrochemical performance in the

conventional solid-state battery interface studies, and enables the establishment of a general model for the electro-chemo-mechanical effects on the solid-state batteries.

I have demonstrated the organic cathode material PTO with high specific energy at active material level in the detailed work in Chapter 3 and Chapter 5. To bring these organic cathode-based solid-state batteries close to the practical application, we need to focus on translating the active material-level high specific energy to the cell level in the future. There are two proposed approaches: 1) exploring ways to increase the active material ratio (from the current 20 wt % to 70 wt%) and areal loading (4 mAh/cm^2) in the composite cathode; 2) reducing the thickness of solid electrolytes and developing the fabrication routine for the sheet-type solid-state batteries for achieving this goal. I have two hypothesis towards the current issue of low active material ratio and the relating solutions will also be briefly discussed.

One of the possible reasons for the low active material ratio issue may be due to the insulating properties of most organic cathode materials, which is very similar to the sulfur as a cathode material. Therefore, in both sulfur and organic cathode cases, excessive amount of solid electrolyte ($>50 \text{ wt } \%$) and carbon ($\sim 20 \text{ wt } \%$) are needed to compensate the insulating natures of active materials. In contrast, inorganic cathode materials such as LiCoO_2 and $\text{LiNi}_{0.8}\text{Mn}_{0.1}\text{Co}_{0.1}\text{O}_2$ have decent electronic conductivity of $\sim 10^{-4} \text{ S/cm}$ and ionic conductivity of $\sim 10^{-8} \text{ S/cm}$,²¹⁷ resulting in high active material ratio in the composite. Therefore, organic cathode materials possess good ionic and electronic conduction properties (mixed conductor) should have the potential for increasing the mass ratio and cell-level specific energy.

In addition to the insulating properties of organic electrode materials, the

insufficient percolated network due to the poor solid-solid contact in the composite cathode also limits the mass loading of the organic cathode materials. The solution processed method for fabricating composite cathode can possibly solve this challenge by achieving an intimate solid-solid contact, which can be realized by coating the dissolved solid electrolytes onto active materials,²¹⁸ or directly infiltrating solution processed solid electrolytes into the porous composite cathode.⁵⁰ By doing this, the interfacial contact can be improved by excluding any cracks and pores at the electrode-electrolyte interface, leading to the higher material utilization.

Solid-state batteries have experienced fast growing interest. However, the understanding of interfacial incompatibilities, cell architecture, and performance are still at an early stage. The transition from conventional bulk-type solid-state batteries to sheet-type solid-state batteries is very critical to improve the cell-level energy. Major efforts are required for a objective evaluation of the technological figure of solid-state batteries. I hope this dissertation make a humble but meaningful contribution in the progress for developing high-performance solid-state batteries.

References

1. Karl, T. R.; Trenberth, K. E., "Modern global climate change." *Science* **2003**, *302*, 1719–1723.
2. Tarascon, J. M.; Armand, M., "Issues and challenges facing rechargeable lithium batteries." *Nature* **2001**, *414*, 359.
3. Armand, M.; Tarascon, J. M., "Building better batteries." *Nature* **2008**, *451*, 652.
4. Dunn, B.; Kamath, H.; Tarascon, J.-M., "Electrical energy storage for the grid: a battery of choices." *Science* **2011**, *334*, 928–935.
5. Larcher, D.; Tarascon, J. M., "Towards greener and more sustainable batteries for electrical energy storage." *Nat. Chem.* **2014**, *7*, 19.
6. Kurzweil, P.; Garche, J., Overview of batteries for future automobiles. Garche, J.; Karden, E.; Moseley, P. T.; Rand, D. A. J., Eds. Elsevier: **2017**; pp 27–96.
7. Calpa, M.; Rosero-Navarro, N. C.; Miura, A.; Tadanaga, K., "Preparation of sulfide solid electrolytes in the Li_2S – P_2S_5 system by a liquid phase process." *Inorg Chem Front* **2018**, *5*, 501–508.
8. Li, W.; Yao, H.; Yan, K.; Zheng, G.; Liang, Z.; Chiang, Y.-M.; Cui, Y., "The synergetic effect of lithium polysulfide and lithium nitrate to prevent lithium dendrite growth." *Nat. Commun.* **2015**, *6*, 7436.
9. Janek, J.; Zeier, W. G., "A solid future for battery development." *Nat. Energy* **2016**, *1*, 16141.
10. Yada, C.; Lee, C. E.; Laughman, D.; Hannah, L.; Iba, H.; Hayden, B. E., "A high-throughput approach developing lithium-niobium-tantalum oxides as

- electrolyte/cathode interlayers for high-voltage all-solid-state lithium batteries." *J. Electrochem. Soc.* **2015**, *162*, A722–A726.
11. Mikhaylik, Y. V.; Akridge, J. R., "Polysulfide shuttle study in the Li/S battery system." *J. Electrochem. Soc.* **2004**, *151*, A1969–A1976.
 12. Luntz, A. C.; Voss, J.; Reuter, K., "Interfacial challenges in solid-state Li ion batteries." *J. Phys. Chem. Lett.* **2015**, *6*, 4599–4604.
 13. Kato, Y.; Hori, S.; Saito, T.; Suzuki, K.; Hirayama, M.; Mitsui, A.; Yonemura, M.; Iba, H.; Kanno, R., "High-power all-solid-state batteries using sulfide superionic conductors." *Nat. Energy* **2016**, *1*, 16030.
 14. Kato, Y.; Shiotani, S.; Morita, K.; Suzuki, K.; Hirayama, M.; Kanno, R., "All-solid-state batteries with thick electrode configurations." *J. Phys. Chem. Lett.* **2018**, *9*, 607–613.
 15. Schnell, J.; Günther, T.; Knoche, T.; Vieider, C.; Köhler, L.; Just, A.; Keller, M.; Passerini, S.; Reinhart, G., "All-solid-state lithium-ion and lithium metal batteries – paving the way to large-scale production." *J. Power Sources* **2018**, *382*, 160–175.
 16. Manthiram, A.; Yu, X.; Wang, S., "Lithium battery chemistries enabled by solid-state electrolytes." *Nat. Rev. Mater* **2017**, *2*, 16103.
 17. Reuter, B.; Hardel, K., "Silbersulfidbromid und Silbersulfidjodid." *Angew. Chem.* **1960**, *72*, 138–139.
 18. Chandra, S.; Lal, H. B.; Shahi, K., "An electrochemical cell with solid, superionic Ag_4KI_5 as the electrolyte." *Journal of Physics D: Applied Physics* **1974**, *7*, 194–198.

19. Yung-Fang Yu, Y.; Kummer, J. T., "Ion exchange properties of and rates of ionic diffusion in beta-alumina." *Journal of Inorganic and Nuclear Chemistry* **1967**, *29*, 2453–2475.
20. Oshima, T.; Kajita, M.; Okuno, A., "Development of sodium-sulfur batteries." *International Journal of Applied Ceramic Technology* **2004**, *1*, 269–276.
21. Fenton, D. E.; Parker, J. M.; Wright, P. V., "Complexes of alkali metal ions with poly(ethylene oxide)." *Polymer* **1973**, *14*, 589.
22. Dudney, N. J.; Bates, J. B.; Zuhr, R. A.; Luck, C. F.; Robertson, J. D., "Sputtering of lithium compounds for preparation of electrolyte thin films." *Solid State Ionics* **1992**, *53–56*, 655–661.
23. Adachi, G.-y.; Imanaka, N.; Tamura, S., "Ionic conducting lanthanide oxides." *Chem. Rev.* **2002**, *102*, 2405–2430.
24. Jian, Z.; Hu, Y.-S.; Ji, X.; Chen, W., "NASICON-structured materials for energy storage." *Adv. Mater.* **2017**, *29*, 1601925.
25. Thangadurai, V.; Narayanan, S.; Pinzaru, D., "Garnet-type solid-state fast Li ion conductors for Li batteries: critical review." *Chem. Soc. Rev.* **2014**, *43*, 4714–4727.
26. Lee, H.; Oh, P.; Kim, J.; Cha, H.; Chae, S.; Lee, S.; Cho, J., "Advances and prospects of sulfide all-solid-state lithium batteries via one-to-one comparison with conventional liquid lithium ion batteries." *Adv. Mater.* **2019**, *0*, 1900376.
27. Xia, S.; Wu, X.; Zhang, Z.; Cui, Y.; Liu, W., "Practical challenges and future perspectives of all-solid-state lithium-metal batteries." *Chem* **2019**, *5*, 753–785.
28. Ratner, M. A.; Johansson, P.; Shriver, D. F., "Polymer electrolytes: ionic transport

- mechanisms and relaxation coupling." *MRS Bull.* **2000**, *25*, 31–37.
29. Meyer, W. H., "Polymer electrolytes for lithium-ion batteries." *Adv. Mater.* **1998**, *10*, 439–448.
 30. Zhang, B.; Tan, R.; Yang, L.; Zheng, J.; Zhang, K.; Mo, S.; Lin, Z.; Pan, F., "Mechanisms and properties of ion-transport in inorganic solid electrolytes." *Energy Storage Mater.* **2018**, *10*, 139–159.
 31. He, X.; Zhu, Y.; Mo, Y., "Origin of fast ion diffusion in super-ionic conductors." *Nat. Commun.* **2017**, *8*, 15893.
 32. Lu, Y.; Li, L.; Zhang, Q.; Niu, Z.; Chen, J., "Electrolyte and interface engineering for solid-state sodium batteries." *Joule* **2018**, *2*, 1747–1770.
 33. Zhou, Y. F.; Xie, S.; Ge, X. W.; Chen, C. H.; Amine, K., "Preparation of rechargeable lithium batteries with poly(methyl methacrylate) based gel polymer electrolyte by in situ γ -ray irradiation-induced polymerization." *Journal of Applied Electrochemistry* **2004**, *34*, 1119–1125.
 34. Appetecchi, G. B.; Croce, F.; Persi, L.; Ronci, F.; Scrosati, B., "Transport and interfacial properties of composite polymer electrolytes." *Electrochim. Acta* **2000**, *45*, 1481–1490.
 35. Zhang, H.; Li, C.; Piszcz, M.; Coya, E.; Rojo, T.; Rodriguez-Martinez, L. M.; Armand, M.; Zhou, Z., "Single lithium-ion conducting solid polymer electrolytes: advances and perspectives." *Chem. Soc. Rev.* **2017**, *46*, 797–815.
 36. Thangadurai, V.; Kaack, H.; Weppner, W. J. F., "Novel Fast Lithium Ion Conduction in Garnet-Type $\text{Li}_5\text{La}_3\text{M}_2\text{O}_{12}$ ($\text{M} = \text{Nb}, \text{Ta}$)." *J. Am. Ceram. Soc.* **2003**, *86*, 437–440.

37. Murugan, R.; Thangadurai, V.; Weppner, W., "Fast lithium ion conduction in garnet-type $\text{Li}_7\text{La}_3\text{Zr}_2\text{O}_{12}$." *Angew. Chem. Int. Ed.* **2007**, *46*, 7778–7781.
38. Junji, A.; Akira, T.; Kunimitsu, K.; Norihito, K.; Yasushi, I.; Junji, A., "Crystal structure of fast lithium-ion-conducting cubic $\text{Li}_7\text{La}_3\text{Zr}_2\text{O}_{12}$." *Chem. Lett.* **2011**, *40*, 60–62.
39. Sharafi, A.; Kazyak, E.; Davis, A. L.; Yu, S.; Thompson, T.; Siegel, D. J.; Dasgupta, N. P.; Sakamoto, J., "Surface chemistry mechanism of ultra-low interfacial resistance in the solid-state electrolyte $\text{Li}_7\text{La}_3\text{Zr}_2\text{O}_{12}$." *Chem. Mater.* **2017**, *29*, 7961–7968.
40. Inaguma, Y.; Liqun, C.; Itoh, M.; Nakamura, T.; Uchida, T.; Ikuta, H.; Wakihara, M., "High ionic conductivity in lithium lanthanum titanate." *Solid State Communications* **1993**, *86*, 689–693.
41. West, A. R., Crystal chemistry of some tetrahedral oxides. In *Zeitschrift für Kristallographie*, 1975; Vol. 141, p 422.
42. Du, Y. A.; Holzwarth, N. A. W., "Mechanisms of diffusion in crystalline electrolytes from first principles." *Physical Review B* **2007**, *76*, 174302.
43. Goodenough, J. B.; Hong, H. Y. P.; Kafalas, J. A., "Fast Na^+ -ion transport in skeleton structures." *Materials Research Bulletin* **1976**, *11*, 203–220.
44. Abrahams, I.; Hadzifejzovic, E., "Lithium ion conductivity and thermal behaviour of glasses and crystallised glasses in the system $\text{Li}_2\text{O}-\text{Al}_2\text{O}_3-\text{TiO}_2-\text{P}_2\text{O}_5$." *Solid State Ionics* **2000**, *134*, 249–257.
45. Jung, Y. S.; Oh, D. Y.; Nam, Y. J.; Park, K. H., "Issues and challenges for bulk-type all-solid-state rechargeable lithium batteries using sulfide solid electrolytes."

Isr. J. Chem. **2015**, *55*, 472–485.

46. Wenzel, S.; Weber, D. A.; Leichtweiss, T.; Busche, M. R.; Sann, J.; Janek, J., "Interphase formation and degradation of charge transfer kinetics between a lithium metal anode and highly crystalline $\text{Li}_7\text{P}_3\text{S}_{11}$ solid electrolyte." *Solid State Ionics* **2016**, *286*, 24–33.
47. Kamaya, N.; Homma, K.; Yamakawa, Y.; Hirayama, M.; Kanno, R.; Yonemura, M.; Kamiyama, T.; Kato, Y.; Hama, S.; Kawamoto, K.; Mitsui, A., "A lithium superionic conductor." *Nat. Mater.* **2011**, *10*, 682–686.
48. Deiseroth, H.-J.; Kong, S.-T.; Eckert, H.; Vannahme, J.; Reiner, C.; Zaiß, T.; Schlosser, M., " $\text{Li}_6\text{PS}_5\text{X}$: a class of crystalline li-rich solids with an unusually high Li^+ mobility." *Angew. Chem. Int. Ed.* **2008**, *47*, 755–758.
49. Kraft, M. A.; Culver, S. P.; Calderon, M.; Böcher, F.; Krauskopf, T.; Senyshyn, A.; Dietrich, C.; Zevalkink, A.; Janek, J.; Zeier, W. G., "Influence of lattice polarizability on the ionic conductivity in the lithium superionic argyrodites $\text{Li}_6\text{PS}_5\text{X}$ ($\text{X} = \text{Cl}, \text{Br}, \text{I}$)." *J. Am. Chem. Soc.* **2017**, *139*, 10909–10918.
50. Kim, D. H.; Oh, D. Y.; Park, K. H.; Choi, Y. E.; Nam, Y. J.; Lee, H. A.; Lee, S.-M.; Jung, Y. S., "Infiltration of solution-processable solid electrolytes into conventional li-ion-battery electrodes for all-solid-state li-ion batteries." *Nano Lett* **2017**, *17*, 3013–3020.
51. Hayashi, A.; Noi, K.; Sakuda, A.; Tatsumisago, M., "Superionic glass-ceramic electrolytes for room-temperature rechargeable sodium batteries." *Nat. Commun.* **2012**, *3*, 856.
52. Knoche, T.; Zinth, V.; Schulz, M.; Schnell, J.; Gilles, R.; Reinhart, G., "In situ

- visualization of the electrolyte solvent filling process by neutron radiography." *J. Power Sources* **2016**, *331*, 267–276.
53. Han, F.; Yue, J.; Chen, C.; Zhao, N.; Fan, X.; Ma, Z.; Gao, T.; Wang, F.; Guo, X.; Wang, C., "Interphase engineering enabled all-ceramic lithium battery." *Joule* **2018**, *2*, 497–508.
54. Zhang, W.; Leichtweiß, T.; Culver, S. P.; Koerver, R.; Das, D.; Weber, D. A.; Zeier, W. G.; Janek, J., "The detrimental effects of carbon additives in $\text{Li}_{10}\text{GeP}_2\text{S}_{12}$ -based solid-state batteries." *ACS Appl. Mater. Interfaces* **2017**, *9*, 35888–35896.
55. Monroe, C.; Newman, J., "The impact of elastic deformation on deposition kinetics at lithium/polymer interfaces." *J. Electrochem. Soc.* **2005**, *152*, A396–A404.
56. Neudecker, B. J.; Dudney, N. J.; Bates, J. B., " "Lithium-free" thin-film battery with in situ plated li anode." *J. Electrochem. Soc.* **2000**, *147*, 517–523.
57. Cheng, E. J.; Sharafi, A.; Sakamoto, J., "Intergranular Li metal propagation through polycrystalline $\text{Li}_{6.25}\text{Al}_{0.25}\text{La}_3\text{Zr}_2\text{O}_{12}$ ceramic electrolyte." *Electrochim. Acta* **2017**, *223*, 85–91.
58. Fudong, H.; Jie, Y.; Xiangyang, Z.; Chunsheng, W., "Suppressing Li dendrite formation in $\text{Li}_2\text{S}-\text{P}_2\text{S}_5$ solid electrolyte by li incorporation." *Adv. Energy Mater.* **2018**, 1703644.
59. Ren, Y.; Shen, Y.; Lin, Y.; Nan, C.-W., "Direct observation of lithium dendrites inside garnet-type lithium-ion solid electrolyte." *Electrochem. Commun.* **2015**, *57*, 27–30.

60. Porz, L.; Swamy, T.; Sheldon, B. W.; Rettenwander, D.; Frömling, T.; Thaman, H. L.; Berendts, S.; Uecker, R.; Carter, W. C.; Chiang, Y.-M., "Mechanism of lithium metal penetration through inorganic solid electrolytes." *Adv. Energy Mater.* **2017**, *7*, 1701003.
61. Sakuda, A.; Hayashi, A.; Tatsumisago, M., "Sulfide solid electrolyte with favorable mechanical property for all-solid-state lithium battery." *Sci. Rep.* **2013**, *3*, 2261.
62. Yu, S.; Schmidt, R. D.; Garcia-Mendez, R.; Herbert, E.; Dudney, N. J.; Wolfenstine, J. B.; Sakamoto, J.; Siegel, D. J., "Elastic properties of the solid electrolyte $\text{Li}_7\text{La}_3\text{Zr}_2\text{O}_{12}$ (LLZO)." *Chem. Mater.* **2016**, *28*, 197–206.
63. Wu, B.; Wang, S.; Evans IV, W. J.; Deng, D. Z.; Yang, J.; Xiao, J., "Interfacial behaviours between lithium ion conductors and electrode materials in various battery systems." *J. Mater. Chem. A* **2016**, *4*, 15266–15280.
64. McCloskey, B. D., "Attainable gravimetric and volumetric energy density of Li–S and Li ion battery cells with solid separator-protected Li metal anodes." *J. Phys. Chem. Lett.* **2015**, *6*, 4581–4588.
65. Kim, S.; Hirayama, M.; Taminato, S.; Kanno, R., "Epitaxial growth and lithium ion conductivity of lithium-oxide garnet for an all solid-state battery electrolyte." *Dalton Trans.* **2013**, *42*, 13112–13117.
66. Chen, R.-J.; Huang, M.; Huang, W.-Z.; Shen, Y.; Lin, Y.-H.; Nan, C.-W., "Sol-gel derived Li-La-Zr-O thin films as solid electrolytes for lithium-ion batteries." *J. Mater. Chem. A* **2014**, *2*, 13277–13282.
67. Ahn, C.-W.; Choi, J.-J.; Ryu, J.; Hahn, B.-D.; Kim, J.-W.; Yoon, W.-H.; Choi, J.-

- H.; Park, D.-S., "Microstructure and Ionic Conductivity in $\text{Li}_7\text{La}_3\text{Zr}_2\text{O}_{12}$ Film Prepared by Aerosol Deposition Method." *J. Electrochem. Soc.* **2015**, *162*, A60–A63.
68. Lobe, S.; Dellen, C.; Finsterbusch, M.; Gehrke, H. G.; Sebold, D.; Tsai, C. L.; Uhlenbruck, S.; Guillon, O., "Radio frequency magnetron sputtering of $\text{Li}_7\text{La}_3\text{Zr}_2\text{O}_{12}$ thin films for solid-state batteries." *J. Power Sources* **2016**, *307*, 684–689.
69. Kazyak, E.; Chen, K.-H.; Wood, K. N.; Davis, A. L.; Thompson, T.; Bielinski, A. R.; Sanchez, A. J.; Wang, X.; Wang, C.; Sakamoto, J.; Dasgupta, N. P., "Atomic layer deposition of the solid electrolyte garnet $\text{Li}_7\text{La}_3\text{Zr}_2\text{O}_{12}$." *Chem. Mater.* **2017**, *29*, 3785–3792.
70. Yi, E.; Wang, W.; Kieffer, J.; Laine, R. M., "Flame made nanoparticles permit processing of dense, flexible, Li^+ conducting ceramic electrolyte thin films of cubic- $\text{Li}_7\text{La}_3\text{Zr}_2\text{O}_{12}$ (c-LLZO)." *J. Mater. Chem. A* **2016**, *4*, 12947–12954.
71. Inada, T.; Kobayashi, T.; Sonoyama, N.; Yamada, A.; Kondo, S.; Nagao, M.; Kanno, R., "All solid-state sheet battery using lithium inorganic solid electrolyte, thio-LISICON." *J. Power Sources* **2009**, *194*, 1085–1088.
72. Nam, Y. J.; Cho, S.-J.; Oh, D. Y.; Lim, J.-M.; Kim, S. Y.; Song, J. H.; Lee, Y.-G.; Lee, S.-Y.; Jung, Y. S., "Bendable and thin sulfide solid electrolyte film: a new electrolyte opportunity for free-standing and stackable high-energy all-solid-state lithium-ion batteries." *Nano Lett* **2015**, *15*, 3317–3323.
73. Sakuda, A.; Kuratani, K.; Yamamoto, M.; Takahashi, M.; Takeuchi, T.; Kobayashi, H., "All-solid-state battery electrode sheets prepared by a slurry

- coating process." *J. Electrochem. Soc.* **2017**, *164*, A2474–A2478.
74. Yamamoto, M.; Terauchi, Y.; Sakuda, A.; Takahashi, M., "Binder-free sheet-type all-solid-state batteries with enhanced rate capabilities and high energy densities." *Sci. Rep.* **2018**, *8*, 1212.
75. Lee, K.; Kim, S.; Park, J.; Park, S. H.; Coskun, A.; Jung, D. S.; Cho, W.; Choi, J. W., "Selection of binder and solvent for solution-processed all-solid-state battery." *J. Electrochem. Soc.* **2017**, *164*, A2075–A2081.
76. Wang, B.; Liu, J.; Norouzi Banis, M.; Sun, Q.; Zhao, Y.; Li, R.; Sham, T.-K.; Sun, X., "Atomic layer deposited lithium silicates as solid-state electrolytes for all-solid-state batteries." *ACS Appl. Mater. Interfaces* **2017**, *9*, 31786–31793.
77. Nagao, M.; Hayashi, A.; Tatsumisago, M., "Sulfur–carbon composite electrode for all-solid-state Li/S battery with Li₂S–P₂S₅ solid electrolyte." *Electrochim. Acta* **2011**, *56*, 6055–6059.
78. Nagao, M.; Hayashi, A.; Tatsumisago, M., "High-capacity Li₂S-nanocarbon composite electrode for all-solid-state rechargeable lithium batteries." *J. Mater. Chem.* **2012**, *22*, 10015–10020.
79. Choi, H. U.; Jin, J. S.; Park, J.-Y.; Lim, H.-T., "Performance improvement of all-solid-state Li-S batteries with optimizing morphology and structure of sulfur composite electrode." *J. Alloys Compd.* **2017**, *723*, 787–794.
80. Liu, Z.; Fu, W.; Payzant, E. A.; Yu, X.; Wu, Z.; Dudney, N. J.; Kiggans, J.; Hong, K.; Rondinone, A. J.; Liang, C., "Anomalous high ionic conductivity of nanoporous β -Li₃PS₄." *J. Am. Chem. Soc.* **2013**, *135*, 975–978.
81. Lin, Z.; Liu, Z.; Dudney, N. J.; Liang, C., "Lithium superionic sulfide cathode for

- all-solid lithium–sulfur batteries." *ACS Nano* **2013**, *7*, 2829–2833.
82. Teragawa, S.; Aso, K.; Tadanaga, K.; Hayashi, A.; Tatsumisago, M., "Liquid-phase synthesis of a Li_3PS_4 solid electrolyte using N-methylformamide for all-solid-state lithium batteries." *J. Mater. Chem. A* **2014**, *2*, 5095–5099.
83. Eun, C. Y.; Ho, P. K.; Hyeon, K. D.; Yang, O. D.; Ram, K. H.; Young - Gi, L.; Seok, J. Y., "Coatable Li_4SnS_4 solid electrolytes prepared from aqueous solutions for all–solid–state lithium–ion batteries." *ChemSusChem* **2017**, *10*, 2605–2611.
84. Han, F.; Yue, J.; Fan, X.; Gao, T.; Luo, C.; Ma, Z.; Suo, L.; Wang, C., "High-performance all-solid-state lithium–sulfur battery enabled by a mixed-conductive Li_2S Nanocomposite." *Nano Lett* **2016**, *16*, 4521–4527.
85. Huo, H.; Zhao, N.; Sun, J.; Du, F.; Li, Y.; Guo, X., "Composite electrolytes of polyethylene oxides/garnets interfacially wetted by ionic liquid for room-temperature solid-state lithium battery." *J. Power Sources* **2017**, *372*, 1–7.
86. Ohta, S.; Seki, J.; Yagi, Y.; Kihira, Y.; Tani, T.; Asaoka, T., "Co-sinterable lithium garnet-type oxide electrolyte with cathode for all-solid-state lithium ion battery." *J. Power Sources* **2014**, *265*, 40–44.
87. Park, K.; Yu, B.-C.; Jung, J.-W.; Li, Y.; Zhou, W.; Gao, H.; Son, S.; Goodenough, J. B., "Electrochemical nature of the cathode interface for a solid-state lithium-ion battery: interface between LiCoO_2 and Garnet- $\text{Li}_7\text{La}_3\text{Zr}_2\text{O}_{12}$." *Chem. Mater.* **2016**, *28*, 8051–8059.
88. Abelmaula, A.; Renaud, B.; Gaëlle, D.; Vincent, S.; Laurence, T.; Mathieu, M.; Patrick, R.; Jean - Marie, T.; Virginie, V.; Mickaël, D., "A new approach to develop safe all–inorganic monolithic Li–ion batteries." *Adv. Energy Mater.* **2011**,

1, 179–183.

89. Kato, T.; Hamanaka, T.; Yamamoto, K.; Hirayama, T.; Sagane, F.; Motoyama, M.; Iriyama, Y., "In-situ $\text{Li}_7\text{La}_3\text{Zr}_2\text{O}_{12}/\text{LiCoO}_2$ interface modification for advanced all-solid-state battery." *J. Power Sources* **2014**, *260*, 292–298.
90. Zhou, W.; Wang, S.; Li, Y.; Xin, S.; Manthiram, A.; Goodenough, J. B., "Plating a dendrite-free lithium anode with a polymer/ceramic/polymer sandwich electrolyte." *J. Am. Chem. Soc.* **2016**, *138*, 9385–9388.
91. Fu, K.; Gong, Y.; Hitz, G. T.; McOwen, D. W.; Li, Y.; Xu, S.; Wen, Y.; Zhang, L.; Wang, C.; Pastel, G.; Dai, J.; Liu, B.; Xie, H.; Yao, Y.; Wachsman, E. D.; Hu, L., "Three-dimensional bilayer garnet solid electrolyte based high energy density lithium metal-sulfur batteries." *Energy Environ. Sci.* **2017**, *10*, 1568–1575.
92. Ren, Y.; Liu, T.; Shen, Y.; Lin, Y.; Nan, C.-W., "Garnet-type oxide electrolyte with novel porous-dense bilayer configuration for rechargeable all-solid-state lithium batteries." *Ionics* **2017**, *23*, 2521–2527.
93. Jan, v. d. B.; Semih, A.; M., R. J. L., "Interface-engineered all-solid-state Li-ion batteries based on garnet-type fast Li^+ conductors." *Adv. Energy Mater.* **2016**, *6*, 1600736.
94. Gong, Y.; Fu, K.; Xu, S.; Dai, J.; Hamann, T. R.; Zhang, L.; Hitz, G. T.; Fu, Z.; Ma, Z.; McOwen, D. W.; Han, X.; Hu, L.; Wachsman, E. D., "Lithium-ion conductive ceramic textile: A new architecture for flexible solid-state lithium metal batteries." *MaterToday* **2018**, DOI: 10.1016/j.mattod.2018.01.001.
95. Han, X.; Gong, Y.; Fu, K.; He, X.; Hitz, G. T.; Dai, J.; Pearse, A.; Liu, B.; Wang, H.; Rubloff, G.; Mo, Y.; Thangadurai, V.; Wachsman, E. D.; Hu, L., "Negating

- interfacial impedance in garnet-based solid-state Li metal batteries." *Nat. Mater.* **2016**, *16*, 572–579.
96. Yang, C.; Zhang, L.; Liu, B.; Xu, S.; Hamann, T.; McOwen, D.; Dai, J.; Luo, W.; Gong, Y.; Wachsman, E. D.; Hu, L., "Continuous plating/stripping behavior of solid-state lithium metal anode in a 3D ion-conductive framework." *Proc. Natl. Acad. Sci. U.S.A* **2018**, DOI: 10.1073/pnas.1719758115.
97. Ong, S. P.; Mo, Y.; Richards, W. D.; Miara, L.; Lee, H. S.; Ceder, G., "Phase stability, electrochemical stability and ionic conductivity of the $\text{Li}_{10\pm 1}\text{MP}_2\text{X}_{12}$ (M = Ge, Si, Sn, Al or P, and X = O, S or Se) family of superionic conductors." *Energy Environ. Sci.* **2013**, *6*, 148–156.
98. Olivetti, E. A.; Ceder, G.; Gaustad, G. G.; Fu, X., "Lithium-ion battery supply chain considerations: analysis of potential bottlenecks in critical metals." *Joule* **2017**, *1*, 229–243.
99. Liang, Y.; Jing, Y.; Gheytani, S.; Lee, K.-Y.; Liu, P.; Facchetti, A.; Yao, Y., "Universal quinone electrodes for long cycle life aqueous rechargeable batteries." *Nat. Mater.* **2017**, *16*, 841–848.
100. Chi, X.; Liang, Y.; Hao, F.; Zhang, Y.; Whiteley, J.; Dong, H.; Hu, P.; Lee, S.; Yao, Y., "Tailored organic electrode material compatible with sulfide electrolyte for stable all - solid - state sodium batteries." *Angew. Chem. Int. Ed.* **2018**, *57*, 2630–2634.
101. Bucci, G.; Swamy, T.; Chiang, Y.-M.; Carter, W. C., "Modeling of internal mechanical failure of all-solid-state batteries during electrochemical cycling, and implications for battery design." *J. Mater. Chem. A* **2017**, *5*, 19422–19430.

102. Chen, R.-J.; Zhang, Y.-B.; Liu, T.; Xu, B.-Q.; Lin, Y.-H.; Nan, C.-W.; Shen, Y., "Addressing the interface issues in all-solid-state bulk-type lithium ion battery via an all-composite approach." *ACS Appl. Mater. Interfaces* **2017**, *9*, 9654–9661.
103. Wang, Y.; Lai, W., "Phase transition in lithium garnet oxide ionic conductors $\text{Li}_7\text{La}_3\text{Zr}_2\text{O}_{12}$: The role of Ta substitution and $\text{H}_2\text{O}/\text{CO}_2$ exposure." *J. Power Sources* **2015**, *275*, 612–620.
104. Cheng, L.; Crumlin, E. J.; Chen, W.; Qiao, R.; Hou, H.; Franz Lux, S.; Zorba, V.; Russo, R.; Kostecki, R.; Liu, Z.; Persson, K.; Yang, W.; Cabana, J.; Richardson, T.; Chen, G.; Doeff, M., "The origin of high electrolyte-electrode interfacial resistances in lithium cells containing garnet type solid electrolytes." *Phys. Chem. Chem. Phys.* **2014**, *16*, 18294–18300.
105. Li, Y.; Chen, X.; Dolocan, A.; Cui, Z.; Xin, S.; Xue, L.; Xu, H.; Park, K.; Goodenough, J. B., "Garnet electrolyte with an ultralow interfacial resistance for Li-metal batteries." *J. Am. Chem. Soc.* **2018**, *140*, 6448–6455.
106. Kerman, K.; Luntz, A.; Viswanathan, V.; Chiang, Y.-M.; Chen, Z., "Review—practical challenges hindering the development of solid state Li ion batteries." *J. Electrochem. Soc.* **2017**, *164*, A1731–A1744.
107. Li, Y.; Wang, Z.; Li, C.; Cao, Y.; Guo, X., "Densification and ionic-conduction improvement of lithium garnet solid electrolytes by flowing oxygen sintering." *J. Power Sources* **2014**, *248*, 642–646.
108. Ito, S.; Fujiki, S.; Yamada, T.; Aihara, Y.; Park, Y.; Kim, T. Y.; Baek, S.-W.; Lee, J.-M.; Doo, S.; Machida, N., "A rocking chair type all-solid-state lithium ion battery adopting $\text{Li}_2\text{O}-\text{ZrO}_2$ coated $\text{LiNi}_{0.8}\text{Co}_{0.15}\text{Al}_{0.05}\text{O}_2$ and a sulfide based

- electrolyte." *J. Power Sources* **2014**, *248*, 943–950.
109. Inada, T.; Takada, K.; Kajiyama, A.; Sasaki, H.; Kondo, S.; Watanabe, M.; Murayama, M.; Kanno, R., "Silicone as a binder in composite electrolytes." *J. Power Sources* **2003**, *119–121*, 948–950.
110. Jiang, C.; Li, H.; Wang, C., "Recent progress in solid-state electrolytes for alkaline ion batteries." *Science Bulletin* **2017**, *62*, 1473–1490.
111. Pervez, S. A.; Cambaz, M. A.; Thangadurai, V.; Fichtner, M., "Interface in solid-state lithium battery: challenges, progress, and outlook." *ACS Appl. Mater. Interfaces* **2019**.
112. Han, F.; Zhu, Y.; He, X.; Mo, Y.; Wang, C., "Electrochemical stability of $\text{Li}_{10}\text{GeP}_2\text{S}_{12}$ and $\text{Li}_7\text{La}_3\text{Zr}_2\text{O}_{12}$ solid electrolytes." *Adv. Energy Mater.* **2016**, *6*, 1501590.
113. Sakuda, A.; Hayashi, A.; Tatsumisago, M., "Interfacial observation between LiCoO_2 electrode and $\text{Li}_2\text{S-P}_2\text{S}_5$ solid electrolytes of all-solid-state lithium secondary batteries using transmission electron microscopy." *Chem. Mater.* **2010**, *22*, 949–956.
114. Zhu, Y.; He, X.; Mo, Y., "Origin of outstanding stability in the lithium solid electrolyte materials: insights from thermodynamic analyses based on first-principles calculations." *ACS Appl. Mater. Interfaces* **2015**, *7*, 23685–23693.
115. Kim, K. H.; Iriyama, Y.; Yamamoto, K.; Kumazaki, S.; Asaka, T.; Tanabe, K.; Fisher, C. A. J.; Hirayama, T.; Murugan, R.; Ogumi, Z., "Characterization of the interface between LiCoO_2 and $\text{Li}_7\text{La}_3\text{Zr}_2\text{O}_{12}$ in an all-solid-state rechargeable lithium battery." *J. Power Sources* **2011**, *196*, 764–767.

116. Culver, S. P.; Koerver, R.; Krauskopf, T.; Zeier, W. G., "Designing ionic conductors: the interplay between structural phenomena and interfaces in thiophosphate-based solid-state batteries." *Chem. Mater.* **2018**, *30*, 4179–4192.
117. Xu, R.; Sun, H.; de Vasconcelos, L. S.; Zhao, K., "Mechanical and structural degradation of $\text{LiNi}_x\text{Mn}_y\text{Co}_z\text{O}_2$ cathode in Li-ion batteries: An Experimental Study." *J. Electrochem. Soc.* **2017**, *164*, A3333–A3341.
118. Zhao, C.; Liu, L.; Qi, X.; Lu, Y.; Wu, F.; Zhao, J.; Yu, Y.; Hu, Y. S.; Chen, L., "Solid–state sodium batteries." *Adv. Energy Mater.* **2018**, *8*, 1703012.
119. Kim, J.-J.; Yoon, K.; Park, I.; Kang, K., "Progress in the development of sodium-ion solid electrolytes." *Small Methods* **2017**, *1*, 1700219.
120. Duchardt, M.; Ruschewitz, U.; Adams, S.; Dehnen, S.; Roling, B., "Vacancy–controlled Na^+ superion conduction in $\text{Na}_{11}\text{Sn}_2\text{PS}_{12}$." *Angew. Chem. Int. Ed.* **2018**, *57*, 1351–1355.
121. Nose, M.; Kato, A.; Sakuda, A.; Hayashi, A.; Tatsumisago, M., "Evaluation of mechanical properties of $\text{Na}_2\text{S–P}_2\text{S}_5$ sulfide glass electrolytes." *J. Mater. Chem. A* **2015**, *3*, 22061–22065.
122. Tian, Y.; Shi, T.; Richards, W. D.; Li, J.; Kim, J. C.; Bo, S.-H.; Ceder, G., "Compatibility issues between electrodes and electrolytes in solid-state batteries." *Energy Environ. Sci.* **2017**, *10*, 1150–1166.
123. Kim, S. W.; Seo, D. H.; Ma, X.; Ceder, G.; Kang, K., "Electrode materials for rechargeable sodium–ion batteries: potential alternatives to current lithium–ion batteries." *Adv. Energy Mater.* **2012**, *2*, 710–721.
124. Pan, H.; Hu, Y.-S.; Chen, L., "Room-temperature stationary sodium-ion batteries

- for large-scale electric energy storage." *Energy Environ. Sci.* **2013**, *6*, 2338–2360.
125. Banerjee, A.; Park, K. H.; Heo, J. W.; Nam, Y. J.; Moon, C. K.; Oh, S. M.; Hong, S.-T.; Jung, Y. S., "Na₃SbS₄: A solution processable sodium superionic conductor for all-solid-state sodium-ion batteries." *Angew. Chem.* **2016**, *128*, 9786–9790.
126. Hayashi, A.; Noi, K.; Tanibata, N.; Nagao, M.; Tatsumisago, M., "High sodium ion conductivity of glass–ceramic electrolytes with cubic Na₃PS₄." *J. Power Sources* **2014**, *258*, 420–423.
127. Tang, H.; Deng, Z.; Lin, Z.; Wang, Z.; Chu, I.-H.; Chen, C.; Zhu, Z.; Zheng, C.; Ong, S. P., "Probing solid–solid interfacial reactions in all-solid-state sodium-ion batteries with first-principles calculations." *Chem. Mater.* **2018**, *30*, 163–173.
128. Ohta, N.; Takada, K.; Sakaguchi, I.; Zhang, L.; Ma, R.; Fukuda, K.; Osada, M.; Sasaki, T., "LiNbO₃-coated LiCoO₂ as cathode material for all solid-state lithium secondary batteries." *Electrochem. Commun.* **2007**, *9*, 1486–1490.
129. Koerver, R.; Aygün, I.; Leichtweiß, T.; Dietrich, C.; Zhang, W.; Binder, J. O.; Hartmann, P.; Zeier, W. G.; Janek, J., "Capacity fade in solid-state batteries: interphase formation and chemomechanical processes in nickel-rich layered oxide cathodes and lithium thiophosphate solid electrolytes." *Chem. Mater.* **2017**, *29*, 5574–5582.
130. Koerver, R.; Zhang, W.; de Biasi, L.; Schweidler, S.; Kondrakov, A. O.; Kolling, S.; Brezesinski, T.; Hartmann, P.; Zeier, W. G.; Janek, J., "Chemo-mechanical expansion of lithium electrode materials—on the route to mechanically optimized all-solid-state batteries." *Energy Environ. Sci.* **2018**, *11*, 2142–2158.
131. Hao, F.; Han, F.; Liang, Y.; Wang, C.; Yao, Y., "Architectural design and

- fabrication approaches for solid-state batteries." *MRS Bull.* **2018**, *43*, 775–781.
132. Zhao, Q.; Lu, Y.; Chen, J., "Advanced organic electrode materials for rechargeable sodium-ion batteries." *Adv. Energy Mater.* **2017**, *7*, 1601792.
133. Jing, Y.; Liang, Y.; Gheyhani, S.; Yao, Y., "Cross-conjugated oligomeric quinones for high performance organic batteries." *Nano Energy* **2017**, *37*, 46–52.
134. Liang, Y.; Yao, Y., "Positioning organic electrode materials in the battery landscape." *Joule* **2018**, *2*, 1690–1706.
135. Nokami, T.; Matsuo, T.; Inatomi, Y.; Hojo, N.; Tsukagoshi, T.; Yoshizawa, H.; Shimizu, A.; Kuramoto, H.; Komae, K.; Tsuyama, H.; Yoshida, J.-i., "Polymer-bound pyrene-4,5,9,10-tetraone for fast-charge and -discharge lithium-ion batteries with high capacity." *J. Am. Chem. Soc.* **2012**, *134*, 19694–19700.
136. Liang, Y.; Zhang, P.; Chen, J., "Function-oriented design of conjugated carbonyl compound electrodes for high energy lithium batteries." *Chem. Sci.* **2013**, *4*, 1330–1337.
137. McGrogan, F. P.; Swamy, T.; Bishop, S. R.; Eggleton, E.; Porz, L.; Chen, X.; Chiang, Y.-M.; Van Vliet, K. J., "Compliant yet brittle mechanical behavior of $\text{Li}_2\text{S}-\text{P}_2\text{S}_5$ lithium-ion-conducting solid electrolyte." *Adv. Energy Mater.* **2017**, *7*, 1602011.
138. Chu, I.-H.; Kompella, C. S.; Nguyen, H.; Zhu, Z.; Hy, S.; Deng, Z.; Meng, Y. S.; Ong, S. P., "Room-temperature all-solid-state rechargeable sodium-ion batteries with a Cl-doped Na_3PS_4 superionic conductor." *Sci. Rep.* **2016**, *6*, 33733.
139. Yu, Z.; Shang, S.-L.; Seo, J.-H.; Wang, D.; Luo, X.; Huang, Q.; Chen, S.; Lu, J.; Li, X.; Liu, Z.-K.; Wang, D., "Exceptionally high ionic conductivity in

- Na₃P_{0.62}As_{0.38}S₄ with improved moisture stability for solid-state sodium-ion batteries." *Adv. Mater.* **2017**, *29*, 1605561-n/a.
140. Heo, J. W.; Banerjee, A.; Park, K. H.; Jung, Y. S.; Hong, S.-T., "New Na-ion solid electrolytes Na_{4-x}Sn_{1-x}Sb_xS₄ (0.02 ≤ x ≤ 0.33) for all-solid-state Na-ion batteries." *Adv. Energy Mater.* **2018**, *8*, 1702716.
141. Moon, C. K.; Lee, H.-J.; Park, K. H.; Kwak, H.; Heo, J. W.; Choi, K.; Yang, H.; Kim, M.-S.; Hong, S.-T.; Lee, J. H.; Jung, Y. S., "Vacancy-driven Na⁺ superionic conduction in new Ca-doped Na₃PS₄ for all-solid-state Na-ion batteries." *ACS Energy Lett.* **2018**, *3*, 2504–2512.
142. Li, Y.; Deng, Z.; Peng, J.; Chen, E.; Yu, Y.; Li, X.; Luo, J.; Huang, Y.; Zhu, J.; Fang, C.; Li, Q.; Han, J.; Huang, Y., "A P2-type layered superionic conductor Ga-doped Na₂Zn₂TeO₆ for all-solid-state sodium-ion batteries." *Chem. Eur. J* **2018**, *24*, 1057–1061.
143. Zhang, Z.; Zhang, Q.; Shi, J.; Chu, Y. S.; Yu, X.; Xu, K.; Ge, M.; Yan, H.; Li, W.; Gu, L.; Hu, Y. S.; Li, H.; Yang, X. Q.; Chen, L.; Huang, X., "A self-forming composite electrolyte for solid-state sodium battery with ultralong cycle life." *Adv. Energy Mater.* **2017**, *7*, 1601196.
144. Kim, J.-K.; Lim, Y. J.; Kim, H.; Cho, G.-B.; Kim, Y., "A hybrid solid electrolyte for flexible solid-state sodium batteries." *Energy Environ. Sci.* **2015**, *8*, 3589–3596.
145. Rao, R. P.; Chen, H.; Wong, L. L.; Adams, S., "Na_{3+x}M_xP_{1-x}S₄ (M = Ge⁴⁺, Ti⁴⁺, Sn⁴⁺) enables high rate all-solid-state Na-ion batteries Na_{2+2δ}Fe_{2-δ}(SO₄)₃|Na_{3+x}M_xP_{1-x}S₄|Na₂Ti₃O₇." *J. Mater. Chem. A* **2017**, *5*, 3377–

3388.

146. Duchene, L.; Kuhnel, R. S.; Stilp, E.; Cuervo Reyes, E.; Remhof, A.; Hagemann, H.; Battaglia, C., "A stable 3 V all-solid-state sodium-ion battery based on a closo-borate electrolyte." *Energy Environ. Sci.* **2017**, *10*, 2609–2615.
147. Wenzel, S.; Leichtweiss, T.; Weber, D. A.; Sann, J.; Zeier, W. G.; Janek, J., "Interfacial reactivity benchmarking of the sodium ion conductors Na₃PS₄ and sodium β-Alumina for protected sodium metal anodes and sodium all-solid-state batteries." *ACS Appl. Mater. Interfaces* **2016**, *8*, 28216–28224.
148. Chevrier, V. L.; Ceder, G., "Challenges for Na-ion negative electrodes." *J. Electrochem. Soc.* **2011**, *158*, A1011–A1014.
149. Oliver, W. C.; Pharr, G. M., "An improved technique for determining hardness and elastic modulus using load and displacement sensing indentation experiments." *J. Mater. Res.* **1992**, *7*, 1564–1583.
150. Koerver, R.; Walther, F.; Aygun, I.; Sann, J.; Dietrich, C.; Zeier, W. G.; Janek, J., "Redox-active cathode interphases in solid-state batteries." *J. Mater. Chem. A* **2017**, *5*, 22750–22760.
151. Wang, Y.; Ding, Y.; Pan, L.; Shi, Y.; Yue, Z.; Shi, Y.; Yu, G., "Understanding the size-dependent sodium storage properties of Na₂C₆O₆-based organic electrodes for sodium-ion batteries." *nano lett.* **2016**, *16*, 3329–3334.
152. Yue, J.; Han, F.; Fan, X.; Zhu, X.; Ma, Z.; Yang, J.; Wang, C., "High-performance all-inorganic solid-state sodium–sulfur battery." *ACS Nano* **2017**, *11*, 4885–4891.
153. Zhao, C.; Liu, L.; Qi, X.; Lu, Y.; Wu, F.; Zhao, J.; Yu, Y.; Hu, Y.-S.; Chen, L., "Solid-state sodium batteries." *Adv. Energy Mater.* **2018**, *8*, 1703012.

154. Wen, Z.; Hu, Y.; Wu, X.; Han, J.; Gu, Z., "Main challenges for high performance nas battery: materials and interfaces." *Adv. Funct. Mater.* **2013**, *23*, 1005–1018.
155. Wang, Y. X.; Zhang, B.; Lai, W.; Xu, Y.; Chou, S. L.; Liu, H. K.; Dou, S. X., "Room–temperature sodium–sulfur batteries: a comprehensive review on research progress and cell chemistry." *Adv. Energy Mater.* **2017**, *7*, 1602829.
156. Wang, C.; Xie, H.; Zhang, L.; Gong, Y.; Pastel, G.; Dai, J.; Liu, B.; Wachsman, E. D.; Hu, L., "Universal soldering of lithium and sodium alloys on various substrates for batteries." *Adv. Energy Mater.* **2018**, *8*, 1701963.
157. Zhou, W.; Gao, H.; Goodenough, J. B., "Low-cost hollow mesoporous polymer spheres and all-solid-state lithium, sodium batteries." *Adv. Energy Mater.* **2016**, *6*, 1501802.
158. Wang, S.; Xu, H.; Li, W.; Dolocan, A.; Manthiram, A., "Interfacial chemistry in solid-state batteries: formation of interphase and its consequences." *J. Am. Chem. Soc.* **2018**, *140*, 250–257.
159. Wang, H.; Chen, Y.; Hood, Z. D.; Sahu, G.; Pandian, A. S.; Keum, J. K.; An, K.; Liang, C., "An air-stable Na₃SbS₄ superionic conductor prepared by a rapid and economic synthetic procedure." *Angew. Chem. Int. Ed.* **2016**, *55*, 8551–8555.
160. Wu, E. A.; Kompella, C. S.; Zhu, Z.; Lee, J. Z.; Lee, S. C.; Chu, I.-H.; Nguyen, H.; Ong, S. P.; Banerjee, A.; Meng, Y. S., "New insights into the interphase between the na metal anode and sulfide solid-state electrolytes: a joint experimental and computational study." *ACS Appl. Mater. Interfaces* **2018**, *10*, 10076–10086.
161. Hu, P.; Zhang, Y.; Chi, X.; Kumar Rao, K.; Hao, F.; Dong, H.; Guo, F.; Ren, Y.;

- Grabow, L. C.; Yao, Y., "Stabilizing the interface between sodium metal anode and sulfide-based solid-state electrolyte with an electron-blocking interlayer." *ACS Appl. Mater. Interfaces* **2019**, *11*, 9672–9678.
162. Hao, F.; Chi, X.; Liang, Y.; Zhang, Y.; Xu, R.; Guo, H.; Terlier, T.; Dong, H.; Zhao, K.; Lou, J.; Yao, Y., "Taming active material-solid electrolyte interfaces with organic cathode for all-solid-state batteries." *Joule* **2019**, *3*, 1349–1359.
163. Berbano, S. S.; Seo, I.; Bischoff, C. M.; Schuller, K. E.; Martin, S. W., "Formation and structure of Na₂S+P₂S₅ amorphous materials prepared by melt-quenching and mechanical milling." *J. Non-Cryst. Solids* **2012**, *358*, 93–98.
164. Nose, M.; Kato, A.; Sakuda, A.; Hayashi, A.; Tatsumisago, M., "Evaluation of mechanical properties of Na₂S-P₂S₅ sulfide glass electrolytes." *J. Mater. Chem. A* **2015**, *3*, 22061–22065.
165. Martin, S. W., Glass and Glass-Ceramic Sulfide and Oxy-Sulfide Solid Electrolytes. WORLD SCIENTIFIC: **2015**; Vol. 6, pp 433–501.
166. Kmiec, S.; Joyce, A.; Martin, S. W., "Glass formation and structural analysis of Na₄P₂S_{7-x}O_x, 0 ≤ x ≤ 7 sodium oxy-thiophosphate glasses." *J. Non-Cryst. Solids* **2018**, *498*, 177–189.
167. Hayashi, A.; Noi, K.; Sakuda, A.; Tatsumisago, M., "Superionic glass-ceramic electrolytes for room-temperature rechargeable sodium batteries." *Nat. Commun.* **2012**, *3*, 856.
168. Bischoff, C.; Schuller, K.; Haynes, M.; Martin, S. W., "Structural investigations of yNa₂S+(1-y)PS_{5/2} glasses using Raman and infrared spectroscopies." *J. Non-Cryst. Solids* **2012**, *358*, 3216–3222.

169. Eckert, J.; Schultz, L.; Hellstern, E.; Urban, K., "Glass-forming range in mechanically alloyed Ni-Zr and the influence of the milling intensity." *J. Appl. Phys.* **1988**, *64*, 3224–3228.
170. Tsukasaki, H.; Mori, S.; Morimoto, H.; Hayashi, A.; Tatsumisago, M., "Direct observation of a non-crystalline state of Li₂S–P₂S₅ solid electrolytes." *Sci. Rep.* **2017**, *7*, 4142.
171. Bischoff, C.; Schuller, K.; Dunlap, N.; Martin, S. W., "IR, Raman, and NMR studies of the short-range structures of 0.5Na₂S + 0.5[xGeS₂ + (1-x)PS_{5/2}] mixed glass-former glasses." *J. Phys. Chem. B.* **2014**, *118*, 1943–1953.
172. Hirai, K.; Tatsumisago, M.; Takahashi, M.; Minami, T., "²⁹Si and ³¹P MAS-NMR spectra of Li₂S-SiS₂-Li₃PO₄ rapidly quenched glasses." *J. Am. Ceram. Soc.* **1996**, *79*, 349–352.
173. Minami, K.; Mizuno, F.; Hayashi, A.; Tatsumisago, M., "Structure and properties of the 70Li₂S·(30-x)P₂S₅·xP₂O₅ oxysulfide glasses and glass-ceramics." *J. Non-Cryst. Solids* **2008**, *354*, 370–373.
174. Tan, G.; Wu, F.; Li, L.; Liu, Y.; Chen, R., "Magnetron sputtering preparation of nitrogen-incorporated lithium-aluminum-titanium phosphate based thin film electrolytes for all-solid-state lithium ion batteries." *J. Phys. Chem. C.* **2012**, *116*, 3817–3826.
175. Jha, P. K.; Pandey, O. P.; Singh, K., "FTIR spectral analysis and mechanical properties of sodium phosphate glass-ceramics." *J. Mol. Struct.* **2015**, *1083*, 278–285.
176. Hayashi, A.; Tatsumisago, M.; Minami, T.; Miura, Y., "Structural investigation of

- 95(0.6Li₂S_{0.4}SiS₂)₅Li₄SiO₄ oxysulfide glass by using x-ray photoelectron spectroscopy." *J. Am. Ceram. Soc.* **1998**, *81*, 1305–1309.
177. Nesbitt, H. W.; Bancroft, G. M.; Henderson, G. S.; Ho, R.; Dalby, K. N.; Huang, Y.; Yan, Z., "Bridging, non-bridging and free (O²⁻) oxygen in Na₂O-SiO₂ glasses: an x-ray photoelectron spectroscopic (XPS) and nuclear magnetic resonance (NMR) study." *J. Non-Cryst. Solids* **2011**, *357*, 170–180.
178. Kim, Y.; Saienga, J.; Martin, S. W., "Glass formation in and structural investigation of Li₂S+GeS₂+GeO₂ composition using Raman and IR spectroscopy." *J. Non-Cryst. Solids* **2005**, *351*, 3716–3724.
179. Kato, A.; Yamamoto, M.; Sakuda, A.; Hayashi, A.; Tatsumisago, M., "Mechanical properties of Li₂S–P₂S₅ glasses with lithium halides and application in all-solid-state batteries." *ACS Appl. Energy Mater.* **2018**, *1*, 1002–1007.
180. Gao, H.; Xin, S.; Xue, L.; Goodenough, J. B., "Stabilizing a high-energy-density rechargeable sodium battery with a solid electrolyte." *Chem* **2018**, *4*, 833–844.
181. Seh, Z. W.; Sun, J.; Sun, Y.; Cui, Y., "A highly reversible room-temperature sodium metal anode." *ACS Cent. Sci.* **2015**, *1*, 449–455.
182. Kim, Y.; Saienga, J.; Martin, S. W., "Anomalous ionic conductivity increase in Li₂S + GeS₂ + GeO₂ glasses." *J. Phys. Chem. B* **2006**, *110*, 16318–16325.
183. Tsai, C.-L.; Roddatis, V.; Chandran, C. V.; Ma, Q.; Uhlenbruck, S.; Bram, M.; Heitjans, P.; Guillon, O., "Li₇La₃Zr₂O₁₂ interface modification for Li dendrite prevention." *ACS Appl. Mater. Interfaces* **2016**, *8*, 10617–10626.
184. Cheng, L.; Chen, W.; Kunz, M.; Persson, K.; Tamura, N.; Chen, G.; Doeff, M., "Effect of surface microstructure on electrochemical performance of garnet solid

- electrolytes." *ACS Appl. Mater. Interfaces* **2015**, *7*, 2073–2081.
185. Garcia-Mendez, R.; Mizuno, F.; Zhang, R.; Arthur, T. S.; Sakamoto, J., "Effect of processing conditions of 75Li₂S-25P₂S₅ Solid electrolyte on its dc electrochemical behavior." *Electrochim. Acta* **2017**, *237*, 144–151.
186. Han, F.; Yue, J.; Zhu, X.; Wang, C., "Suppressing li dendrite formation in Li₂S-P₂S₅ solid electrolyte by Li incorporation." *Adv. Energy Mater.* **2018**, *8*, 1703644.
187. Song, S.; Duong, H. M.; Korsunsky, A. M.; Hu, N.; Lu, L., "A Na⁺ superionic conductor for room-temperature sodium batteries." *Sci. Rep.* **2016**, *6*, 32330.
188. Park, C.-W.; Ryu, H.-S.; Kim, K.-W.; Ahn, J.-H.; Lee, J.-Y.; Ahn, H.-J., "Discharge properties of all-solid sodium–sulfur battery using poly (ethylene oxide) electrolyte." *J. Power Sources* **2007**, *165*, 450–454.
189. Kim, I.; Park, J.-Y.; Kim, C. H.; Park, J.-W.; Ahn, J.-P.; Ahn, J.-H.; Kim, K.-W.; Ahn, H.-J., "A room temperature Na/S battery using a β " alumina solid electrolyte separator, tetraethylene glycol dimethyl ether electrolyte, and a S/C composite cathode." *J. Power Sources* **2016**, *301*, 332–337.
190. Nagata, H.; Chikusa, Y., "An all-solid-state sodium–sulfur battery operating at room temperature using a high-sulfur-content positive composite electrode." *Chem. Lett.* **2014**, *43*, 1333–1334.
191. Tanibata, N.; Deguchi, M.; Hayashi, A.; Tatsumisago, M., "All-solid-state Na/S batteries with a Na₃PS₄ electrolyte operating at room temperature." *Chem. Mater.* **2017**, *29*, 5232–5238.
192. Fan, X.; Yue, J.; Han, F.; Chen, J.; Deng, T.; Zhou, X.; Hou, S.; Wang, C., "High-performance all-solid-state Na–S battery enabled by casting–annealing

- technology." *ACS Nano* **2018**, *12*, 3360–3368.
193. Hayashi, A.; Sakuda, A.; Tatsumisago, M., "Development of sulfide solid electrolytes and interface formation processes for bulk-type all-solid-state Li and Na batteries." *Frontiers Energy Res.* **2016**, *4*.
194. Lu, X.; Xia, G.; Lemmon, J. P.; Yang, Z., "Advanced materials for sodium-beta alumina batteries: Status, challenges and perspectives." *J. Power Sources* **2010**, *195*, 2431–2442.
195. Zhou, W.; Li, Y.; Xin, S.; Goodenough, J. B., "Rechargeable sodium all-solid-state battery." *ACS Central Science* **2017**, *3*, 52–57.
196. Zhang, Z.; Zhang, Q.; Shi, J.; Chu, Y. S.; Yu, X.; Xu, K.; Ge, M.; Yan, H.; Li, W.; Gu, L.; Hu, Y.-S.; Li, H.; Yang, X.-Q.; Chen, L.; Huang, X., "A self-forming composite electrolyte for solid-state sodium battery with ultralong cycle life." *Adv. Energy Mater.* **2017**, *7*, 1601196.
197. Wang, L.-P.; Zhang, X.-D.; Wang, T.-S.; Yin, Y.-X.; Shi, J.-L.; Wang, C.-R.; Guo, Y.-G., "Ameliorating the interfacial problems of cathode and solid-state electrolytes by interface modification of functional polymers." *Adv. Energy Mater.* **2018**, *8*, 1801528.
198. Duchêne, L.; Kühnel, R. S.; Stilp, E.; Cuervo Reyes, E.; Remhof, A.; Hagemann, H.; Battaglia, C., "A stable 3 V all-solid-state sodium–ion battery based on a closo-borate electrolyte." *Energy Environ. Sci.* **2017**, *10*, 2609–2615.
199. Ma, Q.; Liu, J.; Qi, X.; Rong, X.; Shao, Y.; Feng, W.; Nie, J.; Hu, Y.-S.; Li, H.; Huang, X.; Chen, L.; Zhou, Z., "A new Na[(FSO₂)(n-C₄F₉SO₂)N]-based polymer electrolyte for solid-state sodium batteries." *J. Mater. Chem. A* **2017**, *5*, 7738–

7743.

200. Wan, H.; Mwizerwa, J. P.; Qi, X.; Xu, X.; Li, H.; Zhang, Q.; Cai, L.; Hu, Y.-S.; Yao, X., "Nanoscaled Na₃PS₄ solid electrolyte for all-solid-state FeS₂/Na batteries with ultrahigh initial coulombic efficiency of 95% and excellent cyclic performances." *ACS Appl. Mater. Interfaces* **2018**, *10*, 12300–12304.
201. Dai, J.; Yang, C.; Wang, C.; Pastel, G.; Hu, L., "Interface engineering for garnet-based solid-state lithium-metal batteries: materials, structures, and characterization." *Adv. Mater.* **2018**, *30*, 1802068.
202. Xin, S.; You, Y.; Wang, S.; Gao, H.-C.; Yin, Y.-X.; Guo, Y.-G., "Solid-state lithium metal batteries promoted by nanotechnology: progress and prospects." *ACS Energy Lett.* **2017**, *2*, 1385–1394.
203. Ren, Y.; Chen, K.; Chen, R.; Liu, T.; Zhang, Y.; Nan, C.-W., "Oxide electrolytes for lithium batteries." *J. Am. Ceram. Soc.* **2015**, *98*, 3603–3623.
204. Chen, S.; Xie, D.; Liu, G.; Mwizerwa, J. P.; Zhang, Q.; Zhao, Y.; Xu, X.; Yao, X., "Sulfide solid electrolytes for all-solid-state lithium batteries: Structure, conductivity, stability and application." *Energy Storage Mater.* **2018**, *14*, 58–74.
205. Dudney, N. J. W., William C; Nanda, Jagjit;, Handbook of solid state batteries.
206. Miura, A.; Rosero-Navarro, N. C.; Sakuda, A.; Tadanaga, K.; Phuc, N. H. H.; Matsuda, A.; Machida, N.; Hayashi, A.; Tatsumisago, M., "Liquid-phase syntheses of sulfide electrolytes for all-solid-state lithium battery." *Nat. Rev. Chem.* **2019**, *3*, 189–198.
207. Calpa, M.; Rosero-Navarro, N. C.; Miura, A.; Tadanaga, K., "Instantaneous preparation of high lithium-ion conducting sulfide solid electrolyte Li₇P₃S₁₁ by a

- liquid phase process." *RSC Adv.* **2017**, *7*, 46499–46504.
208. Xu, R. C.; Xia, X. H.; Yao, Z. J.; Wang, X. L.; Gu, C. D.; Tu, J. P., "Preparation of $\text{Li}_7\text{P}_3\text{S}_{11}$ glass-ceramic electrolyte by dissolution-evaporation method for all-solid-state lithium ion batteries." *Electrochim. Acta* **2016**, *219*, 235–240.
209. Yao, X.; Liu, D.; Wang, C.; Long, P.; Peng, G.; Hu, Y.-S.; Li, H.; Chen, L.; Xu, X., "High-energy all-solid-state lithium batteries with ultralong cycle life." *Nano Lett* **2016**, *16*, 7148–7154.
210. Ito, S.; Nakakita, M.; Aihara, Y.; Uehara, T.; Machida, N., "A synthesis of crystalline $\text{Li}_7\text{P}_3\text{S}_{11}$ solid electrolyte from 1,2-dimethoxyethane solvent." *J. Power Sources* **2014**, *271*, 342–345.
211. Sedlmaier, S. J.; Indris, S.; Dietrich, C.; Yavuz, M.; Dräger, C.; von Seggern, F.; Sommer, H.; Janek, J., " $\text{Li}_4\text{PS}_4\text{I}$: a Li^+ superionic conductor synthesized by a solvent-based soft chemistry approach." *Chem. Mater.* **2017**, *29*, 1830–1835.
212. Phuc, N. H. H.; Yamamoto, T.; Muto, H.; Matsuda, A., "Fast synthesis of Li_2S – P_2S_5 – LiI solid electrolyte precursors." *Inorg Chem Front* **2017**, *4*, 1660–1664.
213. Tsukasaki, H.; Mori, S.; Morimoto, H.; Hayashi, A.; Tatsumisago, M., "Direct observation of a non-crystalline state of Li_2S – P_2S_5 solid electrolytes." *Sci. Rep.* **2017**, *7*, 4142.
214. Yersak, T. A.; Shin, J.; Wang, Z.; Estrada, D.; Whiteley, J.; Lee, S.-H.; Sailor, M. J.; Meng, Y. S., "Preparation of mesoporous $\text{Si}@\text{PAN}$ electrodes for Li-ion batteries via the in-situ polymerization of PAN." *ECS Electrochem. Lett.* **2015**, *4*, A33–A36.
215. Sakuda, A.; Takeuchi, T.; Okamura, K.; Kobayashi, H.; Sakaebe, H.; Tatsumi, K.;

- Ogumi, Z., "Rock-salt-type lithium metal sulphides as novel positive-electrode materials." *Sci. Rep.* **2014**, *4*, 4883–4883.
216. Han, F.; Westover, A. S.; Yue, J.; Fan, X.; Wang, F.; Chi, M.; Leonard, D. N.; Dudney, N. J.; Wang, H.; Wang, C., "High electronic conductivity as the origin of lithium dendrite formation within solid electrolytes." *Nat. Energy* **2019**, *4*, 187–196.
217. Nagao, K.; Hayashi, A.; Deguchi, M.; Tsukasaki, H.; Mori, S.; Tatsumisago, M., "Amorphous $\text{LiCoO}_2\text{Li}_2\text{SO}_4$ active materials: Potential positive electrodes for bulk-type all-oxide solid-state lithium batteries with high energy density." *J. Power Sources* **2017**, *348*, 1–8.
218. Oh, D. Y.; Nam, Y. J.; Park, K. H.; Jung, S. H.; Kim, K. T.; Ha, A. R.; Jung, Y. S., "Slurry-fabricable Li^+ -conductive polymeric binders for practical all-solid-state lithium-ion batteries enabled by solvate ionic liquids." *Adv. Energy Mater.* **2019**, *9*, 1802927.